EXPERIMENTAL STUDY OF DROPLET IMPINGEMENT USING PHOTO-ACTIVATED NANO-COATINGS AND TEMPERATURE NANO-SENSORS INTEGRATED WITH HIGH-SPEED VISUALIZATION

A Thesis

by

SCOTT WILLIAM HANSEN

Submitted to the Office of Graduate Studies of
Texas A&M University
in partial fulfillment of the requirements for the degree of

MASTER OF SCIENCE

May 2012

Major Subject: Mechanical Engineering

Experimental Study of Droplet Impingement Using Photo-Activated Nano-Coatings and Temperature Nano-Sensors Integrated with High-Speed Visualization

EXPERIMENTAL STUDY OF DROPLET IMPINGEMENT USING PHOTO-ACTIVATED NANO-COATINGS AND TEMPERATURE NANO-SENSORS INTEGRATED WITH HIGH-SPEED VISUALIZATION

A Thesis

by

SCOTT WILLIAM HANSEN

Submitted to the Office of Graduate Studies of
Texas A&M University
in partial fulfillment of the requirements for the degree of

MASTER OF SCIENCE

Approved by:

Chair of Committee,	Debjyoti Banerjee
Committee Members,	Andrew Duggleby
	Robert Handler
	Helen Reed
	Chad Hunter
Head of Department,	Jerry Caton

May 2012

Major Subject: Mechanical Engineering

ABSTRACT

Experimental Study of Droplet Impingement Using Photo-Activated Nano-Coatings and Temperature Nano-Sensors Integrated with High Speed Visualization.

(May 2012)

Scott William Hansen, B.A., The University of South Dakota

Chair of Advisory Committee: Dr. Debjyoti Banerjee

In this study nano-scale transport mechanisms are explored during liquid-vapor phase change phenomena. Surface temperature transients during droplet impingement cooling of a heated surface with a photo-activated nanocoating was measured using temperature nano-sensors integrated with a high speed digital data acquisition system and was synchronized with high speed digital image acquisition system. Control experiments were performed by repeating the experiments without the nanocoating. Photo-activation was achieved at different exposure levels by using an ultra-violet (UV) light source. Photo-activation caused a reduction in the contact angle by up to 20° for a wafer surface with the nanocoatings (compared to that of an unexposed and uncoated wafer surface).

Using microfabrication techniques (a combination of Physical Vapor Deposition/ "PVD" and "lift-off" process) a 2×3 array (300 μm pitch) of novel temperature nano-sensors called "Thin Film Thermocouples" (TFT) were designed and micro-fabricated on a silicon wafer. The wafer was subsequently sputter coated with an insulation layer (SiO_2, 100 nm thick) followed by deposition of the photo-activated nanocoating layer (TiO_2, 150 nm thick).

After achieving steady state conditions, a single droplet of water was dispensed onto the heated surface, centered on the TFT array. The temperature transients recorded by the TFT array were used to estimate the spatial and temporal distribution of heat flux values (both local and global values) during evaporation and boiling of the individual droplets. High speed image acquisition (up to 1000 fps) was performed and synchronized with the high speed data acquisition system (~100 Hz). The transient profiles for temperature and heat flux along with the synchronized images of the droplet were combined into a single video file. These video images enabled the identification of several regimes of phase-change heat transfer during the droplet evaporation process.

Significant improvement in heat flux (for both local and global average) values were observed for the nanocoatings, which were weakly affected by the UV illumination. This shows that the effect of enhanced surface roughness (nucleation site density enhancement) dominated over the effects associated with reduction in contact angle (higher bubble departure diameter and lower departure frequency). Large temporal variations (~10^2 °C/s) and spatial variations (~10^4 °C/m) in surface temperature (and therefore heat flux values at the surface) were observed to exist. These fluctuations in surface temperature were found to occur at time scales less than ~10 ms and length scales of ~300 μm.

To God's Grace, Calvin's Five Points, and Double Imputation

ACKNOWLEDGEMENTS

It is a pleasure to thank the many people who made this thesis possible. It is difficult to overstate my gratitude to my advisor and committee chair, Dr. Banerjee for his guidance and support throughout the course of this research. His enthusiasm, efforts to explain things clearly and simply and ideas made this research an enjoyable experience. I would also like to thank the members of my committee, Dr. Hunter, Dr. Duggleby, Dr. Handler, Dr. Reed, and Dr. Pate. Thank you for your time, input, feedback, and support.

Many thanks are also in order for numerous people at the Air Force Research Lab (AFRL) at Wright Patterson Air Force Base and the University of Dayton Research Institute (UDRI) including Chad Hunter, Steve Patton, Mike Check, Nick Glavin, Ashley White, and David Turner, all of whom answered numerous questions, facilitated my time at AFRL, provided great company, good ideas, and made my time at AFRL very enjoyable. Special thanks are in order to Shawn Putnam for assisting with many aspects of the experimental set-up at AFRL from running the experiments to data acquisition and analysis.

I am also indebted to many student colleagues for providing a great environment to lean and grow. I am especially grateful to the former and currently members of the Multi-Phase Flow and Heat Transfer Lab including Dr. Jeon, Dr. Shin, Dr. Kang, Dr. Joe, Mr. Yu, Mr. Yang, and Nick Niedbalski as well as staff members at the Material and Characterization Facility. Thank you for all your help with FFT's, photolithography, mask aligning, physical vapor deposition, uncertainty analysis, and answering all types of

various questions I had while working in the lab. Work at Texas A&M University with you has been very enjoyable and a great learning experience and one I am very thankful for.

I would also like to thank the congregants of South Dayton Presbyterian Church in Dayton, Ohio for community, encouragement, and fellowship while living in Dayton. Specifically, I would like to thank Mark Carey for organizing living arrangements with many different families throughout the summer and I would like to acknowledge and thank those families - Mark, Sarah, Paul, and Elizabeth Carey; Dot and Dave Weldon; and Jay, Pam, Paul, and Lindsey Strickler. The time living with these families was a blessing I value very deeply.

I'd also to thank many friends at Texas A&M University, mostly whom I've gotten to know through Reformed University Fellowship and many friends whom I've gotten to know through the Johnson Space Center Co-op program. Thank you to all for reminding me, through many different ways and at many different times, that "of the making of many books there is no end, and much study is a weariness of the flesh" (Ecc. 12:12), but also encouraging me to defer immediate gratification at other times. I am grateful for everyone's support and encouragement. Also, a particular thanks to my good friend Rubik Sheth, who provided the initial impetus for me to undertake engineering in the first place.

Lastly, and most importantly, I wish to thank my parents, John and Kay Hansen and brother, Dave, and sister, Kim. Thanks for encouraging me to pursue engineering and supporting me in countless ways throughout my life, especially during my time at Texas A&M University.

NOMENCLATURE

Greek Symbols

α	Thermal diffusivity [m^2/s]
β	Thermal expansion coefficient [1/K]
μ	Dynamic viscosity [Ns/m^2]
v	Kinematic viscosity [m^2/s]
ρ	Density [kg/m^3]
σ	Surface tension [N/m]
τ	Thermocouple temperature uncertainty
w	Uncertainty value

Roman Symbols

Bo	Bond number
C_p	Specific heat [W/(m^2 K)]
D	Droplet diameter [m]
g	Gravity [m/s^2]
h	Heat transfer coefficient [W/(m^2 K)]
h_{fg}	Latent heat of vaporization [W/m^2]
J	Jakob number
k	Thermal conductivity [W/mK]
L_c	Characteristic Length

Nu	Nusselt number
r	Radius [m]
Ra	Rayleigh number
R_c	Thermal contact resistance
Re	Reynolds number
t	Time, seconds
$T_{initial}$	Average initial TFT temperature before droplet impingement
$T(x, t)$	TFT temperature at any point in time
T_∞	Room Temperature
We	Weber number

Subscripts

2-phase	Two Phase
nc	Natural Convection
tft(t)	Temperature of TFT at time t

TABLE OF CONTENTS

Page

Page

CHAPTER

LIST OF FIGURES

FIGURE Page

FIGURE Page

FIGURE Page

LIST OF TABLES

TABLE Page

TABLE Page

CHAPTER I

INTRODUCTION AND LITERATURE REVIEW

Increasing levels of sophistication and complexities in contemporary and upcoming technologies have led to development of enhanced cooling technologies. The next generations of cooling technologies need to be refined to provide more effective means of heat dissipation and thermal management, often at lower temperature differentials (i.e., requiring lower thermal resistances). An example of more sophisticated design involves the increased miniaturization of devices and systems that have led to smaller form factors (less surface area available for heat dissipation) along with higher levels of heat dissipation.

For example, contemporary microchip designs utilize semiconductor devices (diodes and transistors) with design rules of ~30 nm that run at clock speeds exceeding ~5 GHz. Due to increasing clock speed (higher operating frequency) and the number density of devices (higher electrical impedance), higher levels of heat generated by these devices must be dissipated effectively and efficiently [1]. Better thermal management platforms are needed to maintain stability of the operating temperature and prevent, or minimize, the debilitating effects of "hot spots" (local temperature transients) during peak operating periods. These thermal loads are estimated to reach $10^2 \sim 10^3$ W/cm^2 [2]. Even higher continuous heat rejection rates on the order of 10^4 W/cm^2 have been reported within fusion reactors [3].

This thesis follows the style of *AIAA Journal of Thermophysics and Heat Transfer*.

Phase change phenomena such as boiling and evaporation during spray cooling are considered to be an attractive option for combating these high heating loads. Spray cooling has been explored for high heat flux applications such as fire suppression systems and directed energy weapons or "DEW" [3, 4, 5]. During spray cooling, droplets impact a hot surface. By effectively controlling the hydrodynamics of the sprays, even at relatively low flow rates, uniform and high heat fluxes can be achieved [1, 3, 6]. Spray cooling enables higher heat fluxes to be achieved over a larger surface area and can also enable the enhancement of critical heat flux (CHF). Additionally, by utilizing lower flow rates, consumption of coolant is reduced (i.e. higher heat flux per unit mass is achieved), thus reducing costs. Many studies have been conducted regarding spray cooling, maximizing heat flux, and extending the CHF to higher operating temperatures. In this chapter literature review of droplet cooling studies is performed to identify the deficiencies of the current approaches in order to formulate the objectives and scope of this study.

Review of Droplet Cooling

Numerous theoretical and experimental studies have been conducted for droplet cooling. Perhaps the earliest was in 1756 when Liedenfrost discovered the effect bearing his name. In subsequent studies four main heat transfer regimes for droplet cooling (and also for pool boiling) have been identified, which includes: 1) natural convection heat transfer, 2) nucleate boiling, 3) transition boiling, and 4) film boiling. During natural convection, surface fluid motion is mostly governed by free convection currents within the fluid. As the heater surface temperature is increased above the saturation temperature of

the fluid, bubble formation occurs (also called the onset of nucleate boiling). In this regime, isolated bubbles form and a majority of the heat transfer is by transient conduction from the heated surface to the liquid droplet as well as by fluid momentum and energy convection that occurs within the liquid droplet as well as at the surface of the droplet. As temperature increases, more nucleation sites are activated and bubbles begin to form at an increased rate. This could also cause coalescence of adjacent bubbles leading to the formation of larger bubbles which depart from the boiling surface at a faster rate. This regime is called fully developed nucleate boiling. This occurs due to the non-linear coupled interactions of the hydrodynamic and thermal transport processes such as buoyancy force, fluid inertia, and surface tension. This regime continues as the heater surface temperature is increased until the critical heat flux (CHF) condition is reached. At CHF, the limit for the maximum rate of vapor removal is reached. Any incremental increase in surface temperature beyond the CHF condition causes higher vapor generation rate (than can be removed by buoyancy forces) which leads to lateral coalescence of bubbles for a large number of bubbles. This leads to the formation of a stable film of vapor that separates the liquid phase from the heater surface. As the heater temperature is increased the vapor blanket forms an insulating film (the heat flux through the vapor layer is much smaller compared to the heat flux to the liquid phase that is contacting the heater surface at a location away from the continuous vapor film) causing a progressive degradation in the local heat flux values as the film becomes more stable and/or increases in size (i.e., the region of the heater surface covered by the vapor film is extended). This leads to a negative feedback system where increasing the temperature leads to progressive

degradation in the heat flux values. The degradation in heat flux is observed for both the local transient values as well as the global values (i.e., the combined time averaged and spatially averaged values). This is termed transition boiling. Incremental increase in temperature or heat flux causes the transition boiling regime to culminate in a stable film boiling, where the whole heater surface is covered in a stable film of vapor that blankets the heater surface and prevents or minimizes heat transfer by liquid-solid contact. At this point the liquid is separated from the heater surface by a vapor blanket (stable film of vapor) and is marked by a decrease in heat flux. With additional increments in temperature, heat flux increases due to enhanced radiation through the vapor film from the heater to the liquid. Figure 1.1 schematically demonstrates the variation of boiling heat flux as a function of heater temperature (or wall superheat). In this figure, wall superheat, or ΔT_{sat}, is defined as the difference between wall temperature (temperature of the heated surface) and the saturation temperature of the liquid (100°C for water at 1 atmosphere).

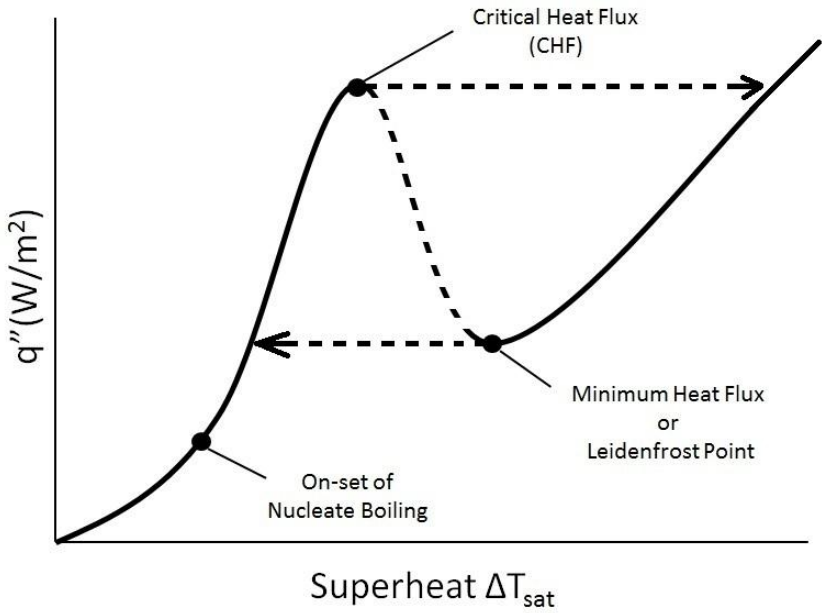

Fig. 1.1 Typical boiling curve

In addition to the boiling curve, Bernardin et. al. described the heat transfer regimes when a small, hot, solid object is suddenly submerged into a bath of liquid [7]. As the hot object is submerged into the liquid, it immediately enters the film boiling regime until it is cooled and the minimum heat flux condition is reached (Leidenfrost point). Collapse of film boiling (leading to transition boiling regime), is usually associated with a sudden drop in temperature. Transition boiling regime is maintained until a minima in the slope of temperature profile occurs, which Bernardin et al. identified as the critical heat flux (CHF) condition. CHF leads to nucleate boiling until the temperature of the solid is below saturation temperature where single phase cooling natural convection occurs [7]. The cooling process described above is shown schematically in Figure 1.2 where time is plotted as a function of wall superheat. Wall superheat is again defined as the temperature difference between wall temperature and the saturation temperature of the liquid.

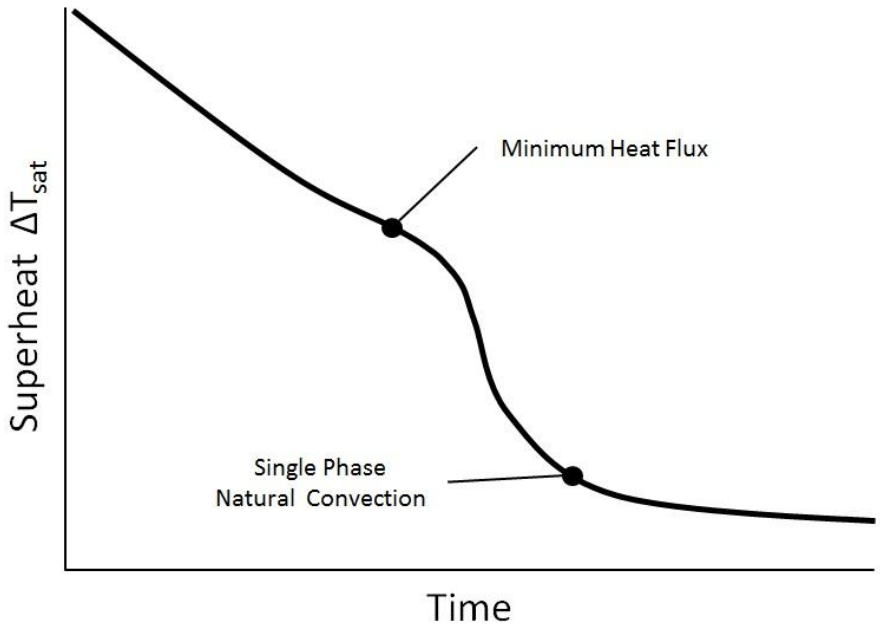

Fig. 1.2 Cooling curve for a hot object submerged in a liquid

In the 1900's, specifically the 50's-60's, a heavy research emphasis was placed on boiling phenomena and applications in nuclear energy generation and nuclear thermal-hydraulics. A significant research focus involved the study of individual and multi-droplet spray cooling systems. Parametric studies were performed by varying surface temperature (wall superheat), working fluids (materials properties), impact velocity of impinging droplets, contact angle, and droplet impingement surface morphologies (coatings). The parametric studies were performed to enumerate the contributions to the total heat flux from the individual parameters. Other parameters such as pressure, subcooling, effects of dissolved gasses, forced convection, gravity, geometry, and surface orientation have also been explored.

The focus of this study is restricted to parametric variation of three primary parameters that are expected to dominate the heat transfer from an impinging droplet. These parameters are impact velocity, surface roughness, and contact angle. The effects of these parameters are described next. Parameters such as pressure, dissolved gasses, gravity, and surface orientation have been neglected as they are assumed to remain constant or have a negligible impact upon heat flux in the experimental set-ups used.

Effect of Impact Velocity

A variety of droplet impingement studies have been reported over the last century. The impact velocity, indicated by the non-dimensional Weber Number, has been regarded to exert a strong influence on the spreading characteristics of the liquid and the transient heat transfer associated with an impinging droplet [3]. Weber number is defined as

$$\mathrm{We} = \frac{\rho \mathrm{V}^2 \mathrm{D}}{\sigma} \tag{1}$$

where ρ is the density of the liquid droplet prior to impingement, V is the impact velocity, D is the initial diameter, and σ is the surface tension of the liquid. Impact velocity influences phase-change heat transfer from a droplet primarily due to two factors, causing progressively smaller resistance values for heat and mass transfer. First, as droplets impact at higher velocities, the droplets spread into thinner and thinner films, leading to higher temperature gradients. The increased force of impact increases the surface area exposed to the heated surface. Second, after an accelerated droplet is suddenly stopped by a surface, a large stagnation pressure is generated in a droplet and the physical properties of the liquid are also altered [8].

McFinnis and Holman noted that the heat transfer from each liquid droplet is proportional to the impact velocity until a critical velocity is reached. After this point the heat transfer rate decreases with increased velocity [3]. In 1970, Pedersen showed that a dominant variable affecting heat transfer is impact velocity [9]. Additionally, droplet impact behavior studies have shown that for Weber numbers greater than eighty, droplets spread out radially into a flat disk and the perimeter of the disks break into smaller droplets [10, 11]. At Weber numbers less than thirty no droplet disintegration occurs, but rather the droplet initially spreads out and then shrinks. At intermediate Weber numbers, the droplet was reported to spread out initially and then shrink, leading to splitting of the droplet into a large and a small droplet [10, 11].

New models and correlations have been developed taking into account the effects of impact velocity. Healy et. al. developed a critical heat flux correlation for droplet impact cooling at lower Weber numbers ranging from 55 to 109 [12]. While Sawyer et. al. developed a similar model for Weber numbers ranging from 207 to 866 [13]. These models have helped in emphasizing the significant effects of the impact velocity of liquid droplets on phase-change heat transfer.

Effect of Surface Roughness

Several experiments have also been conducted to explore droplet evaporation and boiling for different surface conditions. From their boiling experiments for methanol droplets on a hot porous surface, Avedisian and Koplik observed that the heat flux and temperature (wall superheat) increases at the Liedenfrost Point (LFP) with increase in

porosity [14]. Engel found that higher surface roughness promotes droplet break-up [15]. Ganic and Rohsenow found that liquid-solid contact increases with increased surface roughness and led to increased film boiling heat transfer [16]. Interestingly, Bernardin et. al. conducted experiments for three different surface finish conditions and observed that the critical heat flux (CHF) was fairly independent of surface roughness; while in contrast, the LFP was particularly sensitive to surface finish [17, 18]. Changing the surface roughness can lead to enhanced bubble nucleation density (number of departing bubbles per unit area) as well as enhanced bubble departure frequency caused by lateral bubble merger due to a greater number of nucleating and growing bubbles in close proximity, which, in turn, can enhance boiling heat flux. Changing the surface roughness can also significantly alter the contact angle for the liquid droplets on the surface, which can also affect the transport mechanisms (e.g., bubble departure diameter and departure frequency). Effects of changing contact angle are discussed in the next section.

Effect of Contact Angle

Surface coating of TiO_2 can confer unique strategies for modifying transport processes during phase-change heat transfer for impinging droplets. TiO_2 is naturally a hydrophilic surface and when exposed to UV light, the contact angle changes to a very low angle (zero in some cases) within a short period of time (within two hours of prolonged exposure) [19]. TiO_2 coatings can therefore be explored to increase heat transfer to an impinging droplet, since as the contact angle is decreased, the liquid layer becomes thinner. Thus, causing the surface area of the droplet in contact with the heater surface and

to the ambient to increase [4]. This has been explored in both boiling and evaporation studies. Takata et. al. observed that by coating a surface with TiO_2 and exposing to UV light the contact angle is reduced from 97° (unexposed) to ~8° (exposed), resulting in the CHF to be enhanced by a factor of 1.5 ~ 2.2 compared to that of non-coated surfaces [20]. Based on the results from the evaporation experiments, Takata also noted that the Leidenfrost point increases and evaporation time (for individual droplets) decreases with a decrease in contact angle. In similar experiments, Chandra et. al. added surfactant to water to decrease the contact angle [4]. The results from the droplet cooling experiments indicated that decreasing the initial contact angle from 90° to 20° reduced the droplet evaporation time by approximately 50% and increased CHF by 30%. In an additional experiment the authors reported that "a TiO_2 coated specimen was cooled more rapidly than non-coated specimen because the film boiling regime breaks down at higher temperatures" [21]. Another experiment studying the effect of contact angle, metal-coated nanofiber mats were created by electro-spinning a metal (silver or copper) and polymer solution at room temperature onto a copper substrate. This created a structured surface which resulted in a decrease in contact angle and increase in contact area by 25%. Additionally, these nano-coatings showed an increased heat flux by ~13-40%, depending on the type of metal used [22].

Theoretical and Numerical Models

Droplet impingement heat transfer is a complicated problem due to the large number of parameters that affect the phase-change phenomena. To reduce the complexity for analyzing the transport phenomena associated with this topic, researchers have approached the problem using several methods. Several researchers have focused on studying single droplets by analyzing the droplet either as a cylindrical disk on a heated surface (such as the analytical approach used by Bonacia [23] and Grissom [24]), or as a spherical segment (such as the analytical approach used by Sadhal and Plesset [25], and Yang [26]). In addition to these analytical approaches, analytical models for heat transfer based on the "semi-infinite body assumption" have also been used in some studies. This analytical approach was utilized by Sadhal and Plesset [25] and Tio and Sadhal [27]. The treatment of the semi-infinite solid model is further discussed in the Chapter III.

The Volume of Fluid (VOF) method was developed by Hirt and Nichols [28] and Nichols [29] for simulating multi-phase flows and heat transfer. In this method the interface between two phases (e.g., droplet) is tracked by using a VOF function. The value of the VOF function depends on the percentage of a computational cell occupied by the liquid phase. Pasandideh et. al. used a modified version of the VOF method to model tin droplet deformation, solidification, and heat transfer [30]. Nikolopoulos et. al. used this method to predict the height of the vapor blanket between a hot surface and an impinging droplet for temperatures above the Leidenfrost point [10].

An alternate numerical approach is provided by the Level Set Method. Although related to the VOF method, the Level Set method, developed by Sussman [31, 32], uses a

"continuous distance function to indicate the distance from point in space to the free surface" as opposed to 1 and 0, as the VOF method uses.

Review of Transient Temperature Measurements

One popular method of measuring transient temperature is through the use of Thermochromic Liquid Crystals (TLC's). Sodtke et. al. and Stasiek have used these in droplet cooling and surface temperature measurements [33, 34]. As TLC's are heated or cooled, the color of light reflected by the TLC is altered. By imagining these TLC with an IR camera and using a calibrated plate, one can determine the actual surface temperature of a water droplet impinging upon a hot surface. Additionally, TLC's have a high response time of about 10 ms [34]. However, they are limited by the imaging capabilities of the camera which increases both response time and uncertainty.

In more recent years, Thin-Film Thermocouples (TFT's) have been developed and used for measurement of surface temperature transients in boiling. Typically, microfabrication techniques are used to obtain thermocouple junctions which are ~200-400 nm thick. The microfabrication techniques involve metal deposition and patterning using photolithography and Physical Vapor Deposition (PVD) followed by the "lift-off" process. TFT's have been developed by Sunder and Banerjee and several other researchers for use in a variety of applications [35-50] Using TFT's confer several advantages in studying micro/nano-scale transport phenomena during phase change including their small size (minimal invasion of the phase-change phenomena due to act of measurement), fast response time (due to low thermal inertia) and for their flexibility in incorporation in high

spatial density architectures. Additionally, traditional wire-bead thermocouples can interfere with the phase change processes (e.g., boiling, condensation, and evaporation) by providing artificial nucleation sites which can affect the local and global values of heat flux during the phase change processes while also providing unreliable transient responses, and cannot be used to monitor coupled hydrodynamic-thermal structures (such as cold spots) that occur on small scales [35]. TFT's, because of their extremely thin structure, are minimally intrusive and therefore are not expected to significantly perturb the hydrodynamic and thermal transport processes during measurement of the transient surface temperature. Hence TFT can be used to measure surface temperature fluctuations in response to parametric variation of experimental parameters (such as nanocoatings, surface roughness, and contact angle).

TFT dimensions are limited to thicknesses above 100 nm, since a thermocouple junction below this size limit starts behaving as a resistor due to phonon-electron and phonon-phonon interference limits. Jeon [35] obviated this limitation by successfully fabricating Diode Temperature Sensors (DTS) array with the sensor dimensions being below 100nm in thickness. DTS platforms also provide the added benefits in terms of reduced cost of packaging since N wire leads can be used to address [N×(N-1)] sensors. This can enable sensor arrays to be fabricated with much higher speeds (~ 1 ns response time) and much higher spatial density (~ 100 nm pitch). In contrast, TFT are limited to a response time of ~ 10 ns and spatial density of ~ 500 nm pitch. Jeon [35] successfully demonstrated the use of DTS array for measuring the surface temperature transients for droplet impingement cooling using alcohol and acetone droplets. For DTS, the potential

drop across a diode (forward or reverse biased, for a specified current) is proportional to the operating temperature of the diode, which follows an exponential relationship. Similarly, for a specified bias voltage, the diode current can be calibrated as a function of temperature. This temperature metrology technique is very promising. However, fabrication is more complicated compared to TFT. Hence, in this study TFT sensor array was used.

Scope of Investigation

This scope of this experimental study was limited to a single droplet impingement heat transfer, since the information gleaned from these experiments provide a more simplified approach for understanding the coupled transport mechanisms involving thermal-hydraulic interactions along with mass transfer. The information obtained from a simplified approach can then be used to obtain more sophisticated models that can be applied for spray cooling as well as droplet cooling. The operating temperature of this experimental study ranged from saturation temperature (100℃) to a wall superheat of 30°C. Transient temperature data was gathered using TFT array at a data acquisition (sampling frequency) of ~100 Hz. The experiments were performed for silicon wafers with nanocoatings of TiO_2. The effect of UV exposure (and contact angle) as well as surface roughness from the nanocoatings was also explored. Control experiments were performed using bare silicon wafers (with varying levels of UV exposure). Additionally, high speed digital data acquisition was used to obtain images of the impinging droplets at 250-1,000 fps (frames per second).

Intellectual Merits and Broader Impacts of This Study

This study impacts the level of understanding, the state of information and knowledge available, and research efforts in thermal-fluid sciences and phase change phenomena (boiling, evaporation) as well as droplet cooling technologies in the following ways:

1. Novel fabrication and packaging techniques were developed for obtaining temperature nano-sensor (TFT) arrays.
2. This study provides a unique metrology technique for measurement of surface temperature transients using a temperature nano-sensor array.
3. These nano-sensors provide very accurate temperature measurements. The temperature metrology techniques developed in this study also provide for temperature measurements with high spatial and temporal resolution with minimal perturbation of the transport mechanisms associated with phase-change phenomena.
4. Integration of nanocoatings with temperature nano-sensors demonstrates a novel approach for phase-change heat transfer measurements.
5. Integrating: (a) the high speed data acquisition system for temperature data (to monitor thermal behavior); with (b) synchronized recording using high speed digital image and video acquisition system for droplet impact (to monitor hydrodynamic behavior) - demonstrates a novel approach for phase-change heat transfer measurements.

6. Parametric control of experimental parameters such as contact angle by using photo-activated surface nanocoatings (with varying levels of UV illumination) is also a novel experimental approach.
7. The transient temperature data was used to explore the role of transient local heat flux values and global average heat flux values (spatial and temporal average values) in droplet cooling. The effect of the experimental parameters on the heat flux values were used to provide additional insights and for identifying the dominant experimental parameters.
8. Videos with synchronized images of the droplet evaporation and boiling regimes along with the transient temperature data from the TFT array and derived values for heat fluxes (local and global) provided unique insights into the physics of the phase-change phenomena.
9. By synchronizing high speed videos with high speed temperature data and compiling data into a single video file for each experiment (each containing temperature, time, droplet and bubble images, and heat flux data) provided a unique and simple way to analyze a large volume of data. This approach is a pioneering technique that can be used in other studies in the literature for enhanced understanding of the spatial and temporal coupling of the thermal and hydrodynamic transport mechanisms.
10. The compiled videos were used to identify the different regimes of boiling and evaporation during droplet impingement as a function of the experimental parameters (surface roughness, contact angle/UV illumination, nanocoatings/bare

surface, impingement velocity and wall superheat). This is unique and to the knowledge of the author such a comprehensive and detailed study is unprecedented in the boiling literature.

Transformative Nature of This Study

This study was restricted to phase change phenomena for droplet cooling. However, the experimental and metrology techniques as well as data analyses performed in this study have wider applications, as enumerated below.

1. Bio-technology, Homeland and Bio-Security: Nanocoatings and nanostructures can be used to enhance the device performance that require thermo-cycling (e.g., for genomic signal amplification and diagnostics using polymerase chain reaction that involves repeated and rapid thermo-cycling).
2. Deep Drilling for Oil and Gas Exploration (>15,000 feet): Cooling of electronics under high temperature and pressure conditions are needed (e.g., DOE DeepTrek program). The nano-sensors developed in this study can be used in such harsh environments.
3. Nanofluids: The experimental results obtained in this study have implications that project beyond the realm of boiling. For example, in earlier experiments performed at AFRL using nanofluids as coolants in a flow loop apparatus, formation of nano-fins (and nano-caotings) due to precipitation of nanoparticles was reported. Colloidal solvents with dispersed nano-particles are known as nanofluids. These nanocoatings enhanced convective heat flux by ~10%. At higher nano-particle

concentrations these precipitates can agglomerate and cause fouling of the heat exchanging surfaces. This can explain the anomalous behavior and contradictory reports for nanofluids experiments, especially for pool boiling experiments. Anomalous enhancements in the conductivity of nanofluids (e.g. measured using hot-wire techniques) can also be affected due to precipitation of nano-particles, thus forming surface nano-fins. Hence in addition to the boiling heat transfer data – the experimental results from this study have fundamental applications which can aid and complement the interpretation of results from other studies in the thermal-fluids literature on nano-scale transport phenomena.

4. Energy Efficiency/ Sustainability: The results from this study can enable the development of more efficient heat exchangers and thermal management platforms, which are useful for energy efficient buildings and HVAC, solar thermal, geo-thermal and nuclear power plants. In previous studied sponsored by the DOE Solar Energy Technology Program (SETP) phase change phenomena was observed to be induced by nanoparticles. Nanoparticles at very low mass concentrations (~ 2 % or less) were found to enhance the thermal energy storage capacity by 20-120%. This can enable the cost of solar power to be reduced by 40%. The results from this experimental study will significantly impact these energy conversion technologies [50-78].

There are six chapters in this thesis. Chapter II provides the description of the microfabrication of the TFT temperature nano-sensors and packaging; as well as the experimental apparatus and experimental procedure used in this study. Chapter III provides information on data analysis. Results of the data analysis are discussed in Chapter IV. The process of making synchronized videos is described in Chapter V. The final chapter summarizes findings and provides future direction for related studies.

CHAPTER II

MICROFABRICATION AND PACKAGING

Fabrication of Thin-Film Thermocouple Sensors

In designing the mask-layout for the TFT array used in this study, several factors were considered. Items to be taken into consideration include adequate bonding pad dimensions to ensure adequate space for wire-bonding, smooth round edges to avoid high stress concentration points during fabrication, and positioning of clear alignments marks to ensure that metal junctions are in contact. Additionally, three constraints were imposed to be consistent with the logistics and experimental apparatus available at the Air Force Research Lab (AFRL) at Wright-Patterson Air Force Base (WPAFB, OH). First, the TFT array needed to be fabricated onto a one-inch diameter (300 um thick) silicon wafer in order to match the heater used in the experimental set-up at AFRL. Second, a total of six junctions on a 300 um pitch (3×2 array of TFT) could be fabricated on the surface to match the available form factor of the experimental apparatus. The third constraint arose from the limitations associated with the commercial mask fabrication, photolithography/design rules and reliability of the lift-off process available at Texas A&M University that necessitated each thermocouple junction to be 50 μm in width. Taking these considerations and requirements into account several designs were developed using SolidWorks®. A final design was chosen and shown in the schematic of Figure 2.1. The dimensions for the chosen layout are shown in Figure 2.2. This design was chosen based on the size available for bonding pad, smoother edges, consistent alignment marks,

and width of the thermocouple junctions (each with smooth curves leading to the junction). Additionally, the TFT were fabricated from K-type thermocouple materials (alumel and chromel).

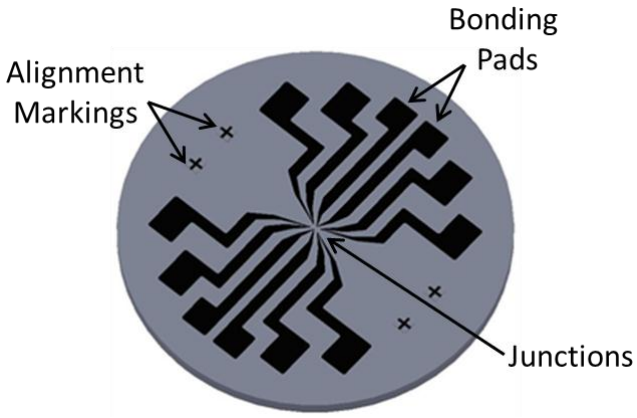

Fig. 2.1 Solid model showing the layout of TFT array.

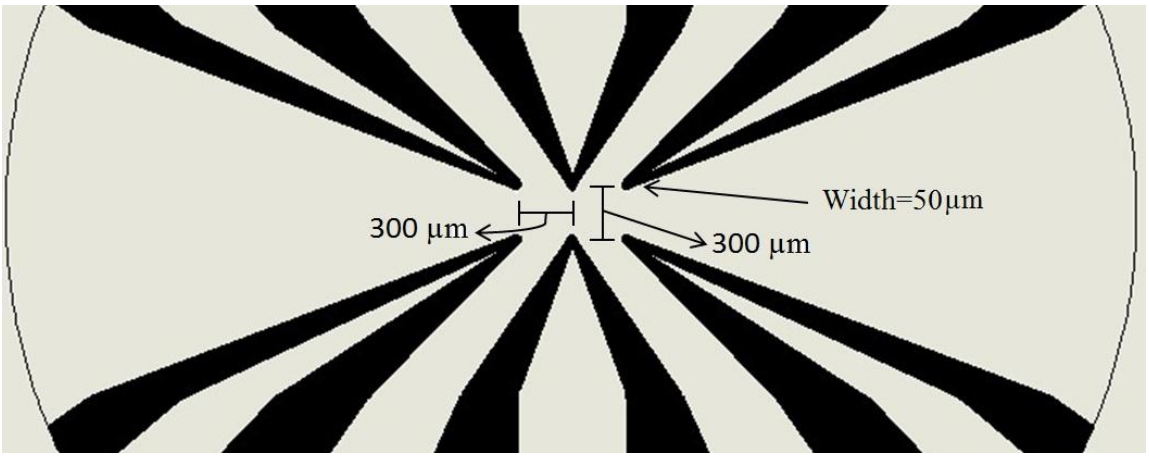

Fig. 2.2 Solid model showing the dimensions of the TFT array.

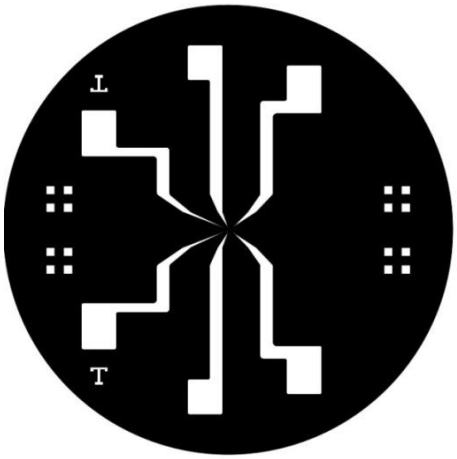

Fig. 2.3 Alumel mask.

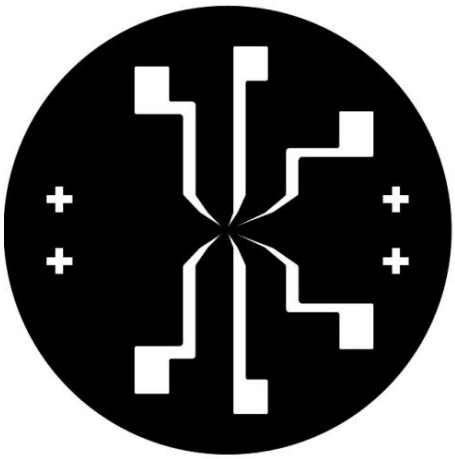

Fig. 2.4 Chromel mask.

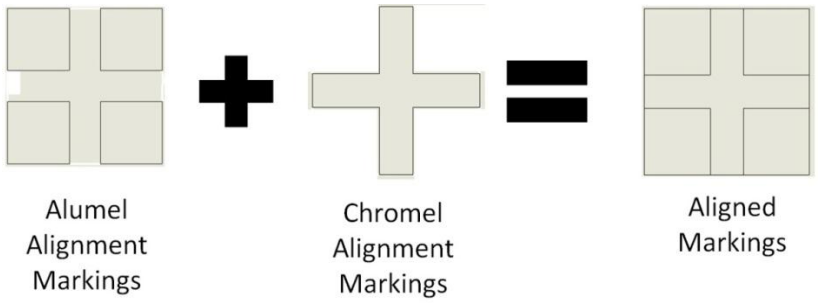

Fig. 2.5 Alignment markings

After both masks were printed commercially at South West Printing in College Station, TX, a multi-step lithography and Physical Vapor Deposition (PVD) process was used to fabricate each TFT. This process is completed twice, once for chromel and once for alumel. In preparation for PVD, a new wafer is unpackaged in a class 1000 clean room environment and rinsed with acetone, IPA, and ultrapure water, each for fifteen seconds. After rinsing, the wafer is blown dry with compressed nitrogen and the process is repeated. Next, the wafer is heated to 200 ºC on a hot plate for five minutes and then allowed to cool for one minute. It is then placed in a MARCH Model CS-170 Reactive Ion Etcher (RIE),

seen in Figure 2.6, where it undergoes an Oxygen Plasma Descum for 300 seconds at 350W. This process works by generating directed fluorine containing plasma. The plasma reacts with the surface to create gas-phase species, which etches the surface. It is important to note that since the plasma is induced by only oxygen and reacts only with organic species and does not affect the silicon surface.

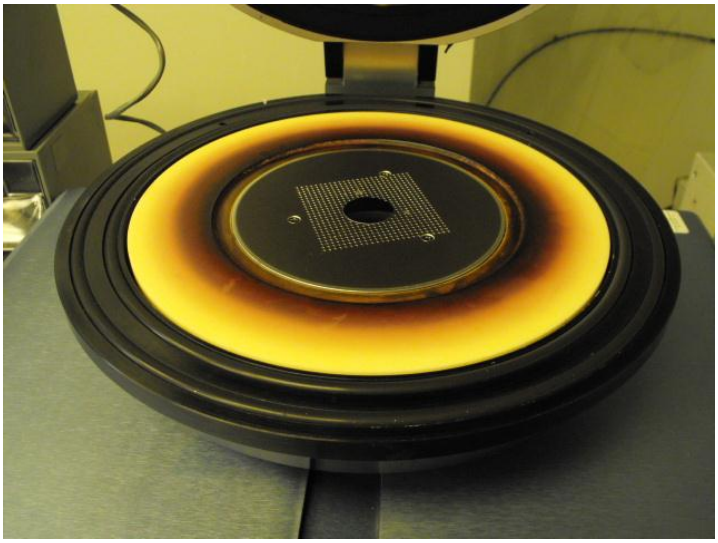

Fig. 2.6 Reactive Ion Etcher (RIE).

After the wafer is removed from the RIE, the wafer is placed on a hotplate at 100 ºC for five minutes for a pre-bake. It is then removed and placed onto the chuck of the spin-coater (Figure 2.7). SU-1827 positive photoresist is then pipetted onto the wafer surface ensuring coverage of the entire wafer and the absence of bubbles after application. Presence of bubbles could lead to an uneven distribution of photoresist during spin-coating. SU-1827 is chosen since it is a non-hazardous chemical, has low toxicity,

provides excellent adhesion to silicon wafers, provides good coating uniformity, and for its reliability.

A spin-coating protocol was implemented (individual step of the protocol are listed Table 1), to obtain a thin film of approximately 2.7 micrometers thickness of photoresist on the wafer. The wafer was visually inspected for foreign materials and evenness of coating (e.g., striation marks can form during the spinning process due to specs of dust). If the coating quality was detected to be unsatisfactory the wafer was cleaned with acetone and spin-coating was repeated.

Fig. 2.7 Spin-coater with chuck.

Table 2.1 Spin-coater settings

Run Time	1 minute
Acceleration	1,000 rpm/second
RPM	3,000

Next, the wafer, with deposited photoresist, was placed onto the 100ºC heater for a quick thirty second soft-bake. This added "bake" ensures the photoresist is "cured" to provide adequate adhesion to the wafer. If this post-bake is not completed, extra photoresist (in addition to what had been exposed to UV light) may be removed during the development process in which specific portions of the photoresist are removed. After post-bake the wafer is ready for exposure to UV light using MCF's Quintel Q4000 Mask Aligner (Figure 2.8).

Prior to performing mask alignment, several steps were followed. First, the alumel or chromel mask (Figure 2.3 or 2.4) is rinsed with acetone and IPA and dried with compressed nitrogen to ensure foreign debris are removed. It is then attached to a glass plate with scotch tape and placed on the masking mount. Next, the silicon wafer is carefully attached to a 3" Pyrex wafer using double sided tape and placed on the mask aligner chuck. Vacuum suction ensures that the wafer does not move during exposure (Figure 2.8). The next step is to align the silicon wafer and mask using alignment markings (Figure 2.5). If the wafer is undergoing its first exposure, the mask is simply aligned with the center of the silicon wafer.

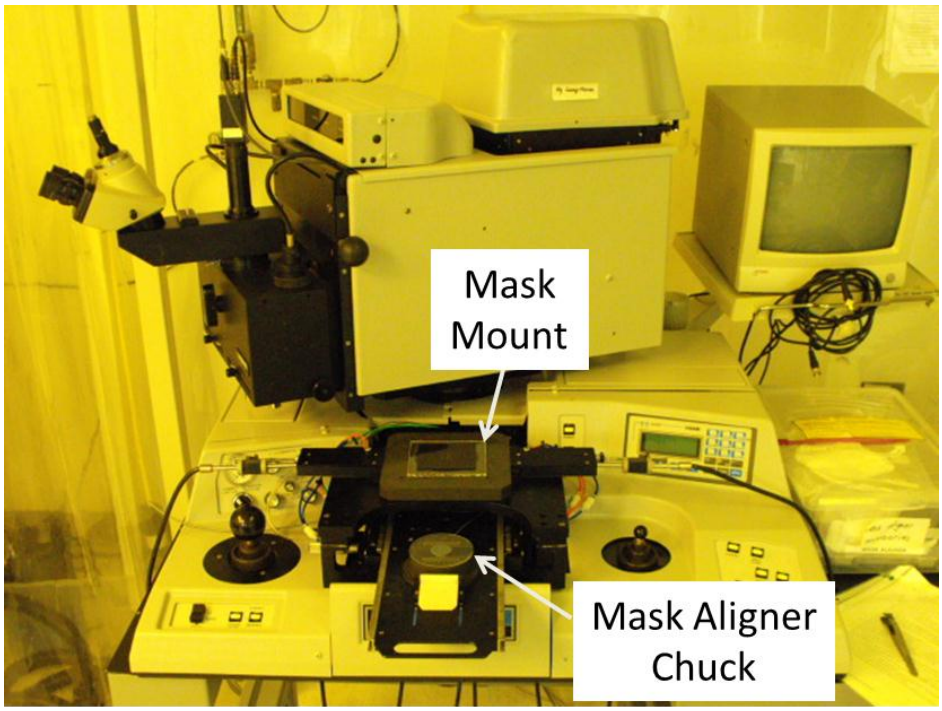

Fig. 2.8 Mask aligner with mask and wafer in place (UV light turned to side)

Once aligned, both the mask and silicon wafer are exposed to UV light for twenty seconds at an intensity setting of 13 $\frac{W}{cm^2}$ The dosage is prescribed as

$$\text{Intensity*Time=Dose } \left[\frac{mJ}{cm^2}\right] \tag{2}$$

This exposure rate provides 260 $\frac{W}{cm^2}$. Once exposed, the silicon wafer is removed from the Pyrex wafer and placed into a bath of MF-319 developer fluid and agitated by swirling by hand for approximately one minute, or until all exposed photoresist has been dissolved. This process removes exposed photoresist but leaves photoresist covered by the alumel or chromel mask. After adequate development, the wafer is rinsed only with ultra-pure water and blown dry with compressed air. With the mask alignment and development complete, the wafer is now ready for PVD.

PVD is a process whereby materials are deposited in the form of a thin film by condensing an evaporated mass of a chosen material (also called the "target") onto a rotating work piece. This is accomplished by heating a tungsten boat (containing the chosen material such as a metal) by passing electrical current to a very high temperature under a low vacuum environment. The target material in the boat is vaporized and deposited onto the wafer surface that is mounted on a rotating disc. High temperatures are required to melt metals, hence, chromel is deposited first as its melting temperature (1420°C) is higher than that of alumel (1260°C). This provided a more reliable process for PVD, since chromel would be unaffected (or marginally affected) during the deposition of alumel layer.

In this study PVD of chromel was performed in Edwards Auto 306 evaporation chamber at the MCF (Figure 2.9) and PVD of alumel was performed in a Denton Vacuum BTT-IV in the Multi-Phase and Heat Transfer Lab at A&M. Both deposition chambers have similar operating principles. After the silicon wafer is attached to the top rotating work piece and metal (chromel or alumel) for deposition placed into a tungsten boat (the target), the chamber can be closed, sealed, and air evacuated using a roughing pump and turbo-pump. Deposition can begin as soon as the appropriate vacuum level is obtained (approximately 2 $x10^{-6}$ Torr). Thickness of deposition is measured using a quartz crystal microbalance for the Edwards instrument (located at the MCF). Calibration data developed through trial and error is used to determine thickness when using the Denton Vacuum chamber. Once the required thickness is obtained, the electrical current is stopped and the chamber is allowed to cool and re-pressurize to ambient conditions. The thickness of the

deposited metal for the TFT arrays is approximately 250 nm. The thickness of the deposited material is measured by using a Dektak 3 Stylus Profilometer at the MCF. The profilometer results are shown in Figures 2.10 and 2.11.

After the completion of PVD, the metal is "lifted-off" by submerging and ultrasonicating the wafer in a bath of "PG Remover". During lift-off process, the photoresist is chemically dissolved by the PG Remover. The metal layer in contact with the exposed regions of the wafer remains after the photo-resist is removed. This entire process is then repeated for the next metal. A schematic of the process sequence for microfabrication of TFT is shown in Figure 2.12. After completing the photo-lithography, PVD and lift-off process, the TFT array is ready for packaging using wire-bonding which is described next.

Fig. 2.9 Physical vapor deposition chamber at MCF

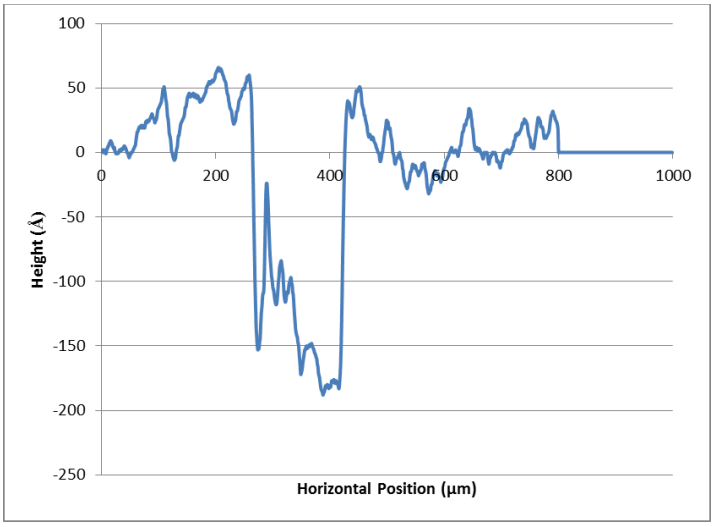

Fig. 2.10 Profilometer scan 1

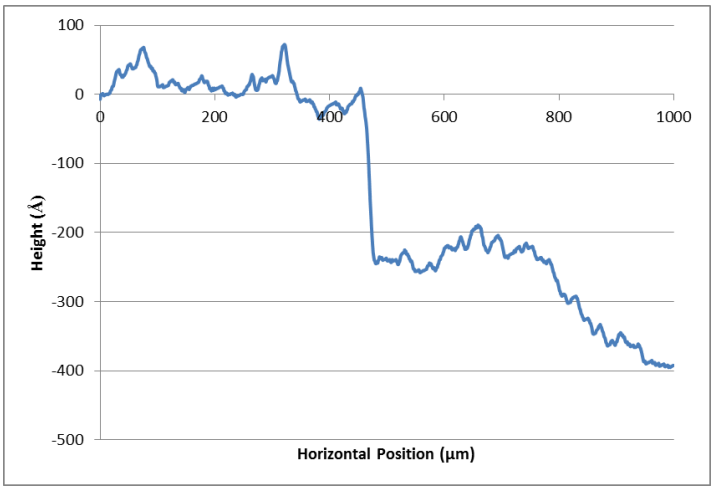

Fig. 2.11 Profilometer scan 2

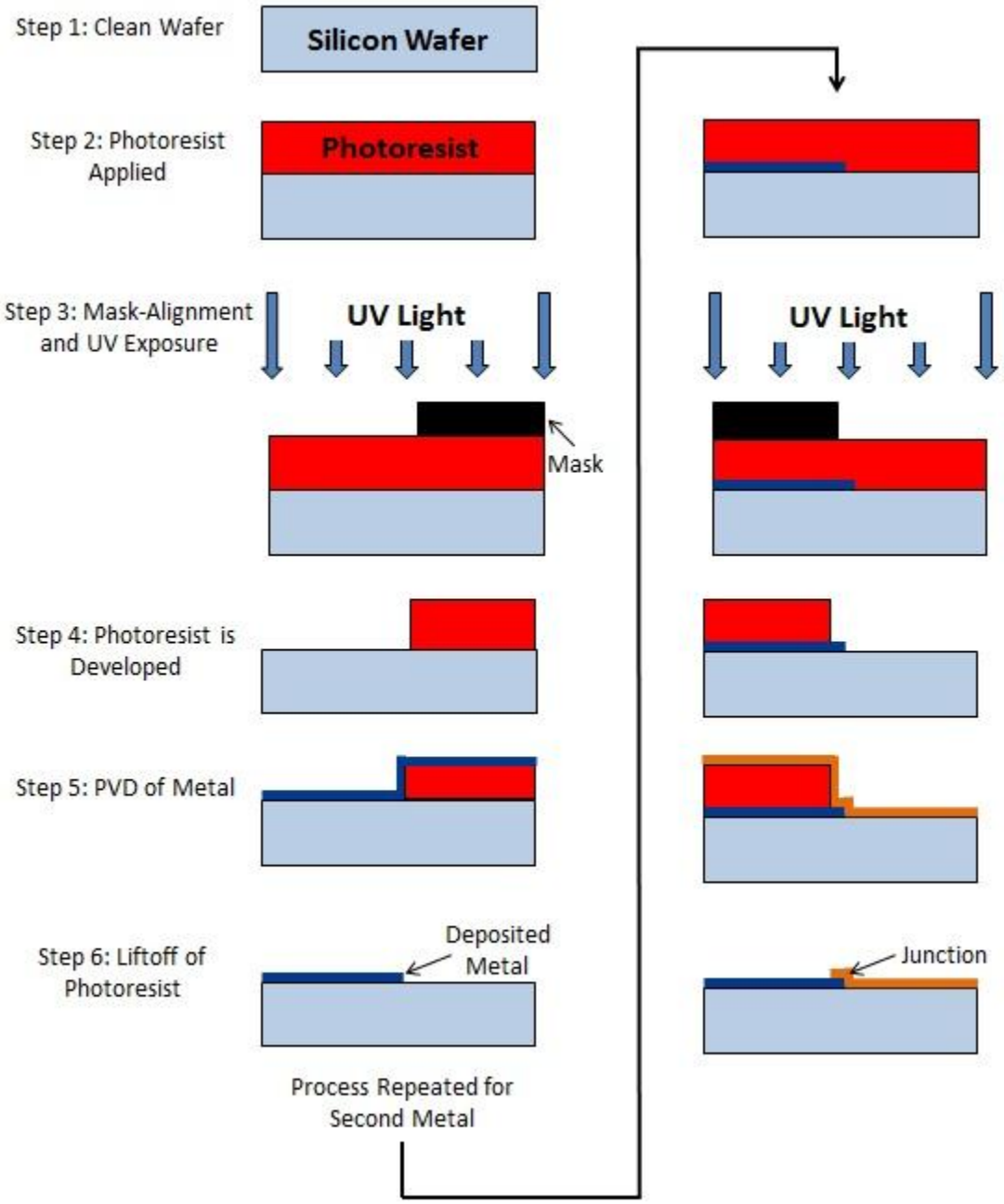

Fig. 2.12 Schematic shown the process sequence for microfabrication of TFT.

Wire-bonding is a simple process in which wire leads are connected to metal thin films. Wire-bonding provides a simple approach for attaching alumel and chromel lead wires to the corresponding bond pads on the wafer. These wires are then connected to a data acquisition instrument where the voltage (and therefore temperature) transients are recorded for the individual junctions.

In this study wire bonding was performed in three steps. First, the last 1/8" of the end of the lead wire is bent at a 90° angle to create a contact surface (instead of a contact point) for bonding to the bond pad. After positioning the wire on the appropriate bond pad, a liberal amount of silver paste was applied and allowed to dry for approximately one hour on a hot plate of 60°C. Second, a two part epoxy (Amerco-Bond 526N-A) was applied over the silver paste and allowed to dry overnight on a hotplate at 120 °C. This glue allowed for a more ductile bond. Third, a liberal amount of JB weld was applied, sealing the epoxy and silver paste. This was then allowed to dry for 4 hours on a hotplate at 120°C and a second layer was applied for added mechanical strength. After the second layer is dried the TFT is ready for use. It is important to note that some TFT's were fabricated eliminating the second step (application of the two part epoxy). Eliminating this step did not affect the performance of the TFT and was done to decrease the amount of time needed to package a TFT. A completed TFT array (before packaging) on a wafer is shown in Figure 2.13. A TFT array after wire-bonding is shown in Figure 2.14 and a magnified image of a typical TFT junction is shown in Figure 2.15.

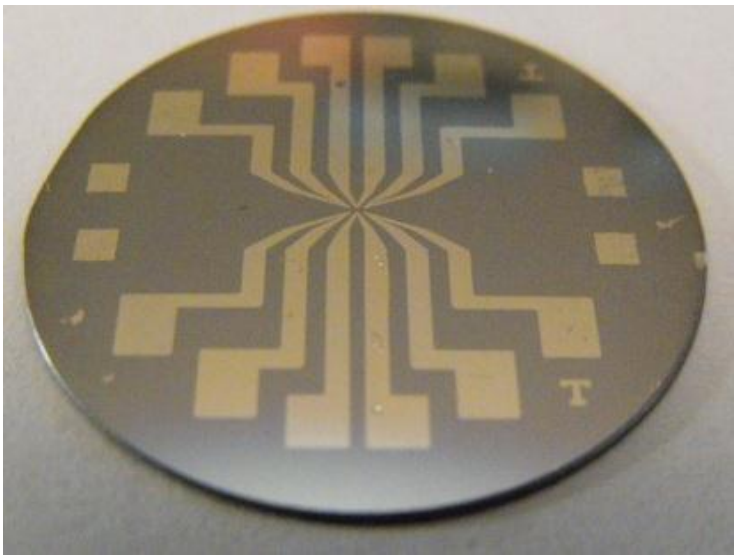

Fig. 2.13 Image of TFT Array on a silicon wafer (without wire-bonding).

Fig. 2.14 Image of TFT Array on a silicon wafer (after wire-bonding).

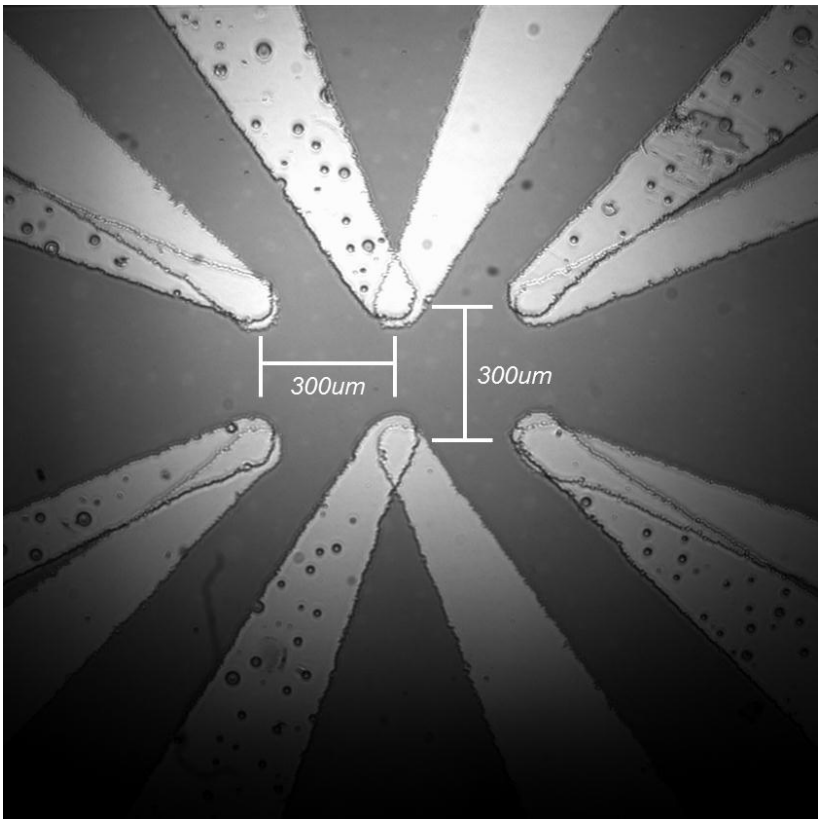

Fig. 2.15 Magnified image of typical TFT junctions

Titanium Dioxide Coating

In addition to conducting droplet impingement studies on an uncoated TFT wafer, experiments were also conducted on wafers coated with TiO_2. Since TiO_2 is conductive and adding a conductive coating to the surface of multiple thermocouples would render the thermocouples useless, a very thin layer of insulating glass (100 nm) was deposited before deposition of TiO_2. This glass layer provided an insulating barrier between the conductive TiO_2 and thermocouples. To achieve complete coating of glass and TiO_2, two additional steps were required after photolithography and PVD process but *before* the wire-bonding process. The two step process involved spin-coating a thin layer of glass

onto the surface of the wafer, followed by sputter coating of TiO_2 on top of the deposited glass layer.

Honeywell International T-11 Type 111 Spin-on-Glass was used for spin-coating of the glass layer. This special type of glass is spin-coated in liquid form and cured to form a thin and even layer of glass. Additionally, this glass was chosen because of its high crack resistance, low shrinkage upon cure, thermal stability, excellent adhesion to silicon wafers, and was readily available at AFRL. Glass was spin coated using settings listed in Table 2.2 to ensure a thickness of approximately 100 nm, which was confirmed by profilometer measurement at AFRL. It is important to note that glass was spun-on and not sputter coated. This process was preferred over sputter coating, where the thickness of glass is difficult to control because of the insulating properties of glass. After spin coating, the wafer was placed on a hot plate at 90°C for a one-hour soft-bake followed by one-hour at 400°C for hard-bake. The baking process was used to cure the liquid layer into glass, thus providing the necessary insulation between TiO_2 and thermocouples.

Table 2.2 Settings used for spinning coating of glass layer

Run Time	30 seconds
Acceleration (RPM/sec)	1,000 rpm/second
RPM	5000

Next, a magnetron sputtering instrument was used for sputter coating of a TiO_2 layer to achieve a thickness of approximately 150 nm. After sputter coating was complete, the TiO_2 coated wafer was used for wire-bonding of lead wires to the bond-pads. This procedure is described next.

Wire bonding was performed after sputter coating of the TiO_2 layer and spin-coating of the glass layer. This sequence of processing steps was developed for preventing any interference with the deposition process. During sputter coating, a non-uniform surface (such as surface with JB Weld) could lead to uneven coating of TiO_2. Similarly, using a spin-coater required the use of a wafer with uniform surface roughness to ensure uniform thickness of the spin-coated glass. In both cases, the deposited materials covered the TFT array and the bond pads. This posed a problem as the TFT needed to be packaged using wire-bonding in the subsequent steps. Two methods were investigated for wire bonding after sputter coating and spin coating processes. First, masking tape was applied over the bonding pad so the materials coated would not cover the bonding pads. This option was not viable as a somewhat sticky residue was left on the TFT and the wafer could be damaged upon removal of the tape. The second option was to coat the entire surface and scratch through the TiO_2 and glass layers, revealing the thermocouple bonding pad. This scratching process deemed to be an acceptable method of revealing the bonding pad, so it was the method used.

Calibration and Bias

After the coating step and wire bonding (packaging) step was completed, calibration of the TFT junctions was performed. Calibration for all TFT junctions was performed using an isothermal oven. The wafer containing the TFT array was suspended in the middle of the oven using adhesive tape and a wire-bead thermocouple was positioned about half inch from the surface of the TFT array. Temperature was measured

at five oven set-point temperatures; 50 ℃, 80 ℃, 100 ℃, 120 ℃, and 135 ℃. This process was repeated for all TFT junctions in the temperature nano-sensor array. Results from the calibration procedure are listed in Appendix A. All the TFT junctions used in this study showed a linear response for the output voltage as a function of temperature. After the calibration procedure was implemented it was observed that Junction 3 had a bias error. Hence a fixed bias was added to the measurements of junction 3 (for the TiO_2 coated wafer). This was performed by determining the average initial temperature between the two known temperatures and adding the correlated value to junction temperatures requiring a bias.

Description of Experimental Apparatus

Two experimental set-ups were used in this study. The first experimental apparatus was located at the AFRL-WPAFB, OH. This apparatus was used for performing experiments using TiO_2 coated (unexposed and exposed) as well as uncoated (unexposed) experiments. The experiments conducted at AFRL also involved the investigation of changes in contact angle and surface roughness on droplet impingement heat transfer. The second experimental apparatus was located in the Multi-Phase Flow and Heat Transfer Laboratory at Texas A&M University (supervised by Dr. Debjyoti Banerjee and his research group). This apparatus was virtually identical to that at AFRL. However, a different UV light source was used in the apparatus at Texas A&M University and the light intensity was varied using ND filters. The second experimental apparatus was used to perform the control experiments using uncoated (bare) wafers. The uncoated wafers were

photo-activated using different levels of UV illumination to verify if the level of illumination affected the droplet impingement heat transfer.

Experimental Apparatus 1 (AFRL)

The experimental apparatus used at AFRL-WPAFB consisted of a calorimeter for measuring the heat flux during droplet impingement. The calorimeter consisted of an one-inch diameter cylindrical copper block with an embedded cartridge heater. The power input to the calorimeter was controlled by a power supply. The wafer was mounted on the copper block by using OmegaTherm 201 thermal paste. In addition, two small pieces of electrical tape were used to secure the silicon wafer on the copper block. The DAQ system consisted of a 4-channel, 24-Bit NI 9219 Universal Analog Input Module inserted into a NI High-Speed USB Carrier. The DAQ was controlled by connecting to a laptop computer and using Labview® software. Transient voltage data from the TFT junctions in the array were recorded using Labview® and were displayed in real-time. The sampling time for each sensor for the data acquisition was fixed at 10 or 11 ms.

Droplets were generated at the end of a polished hypodermic needle using a syringe pump. This needle was polished using 400 grit sandpaper on a polishing table and was performed to minimize the size of the water droplet (~6-8 mm^3). The tip of the syringe was mounted on a 3-axis translation stage for aligning the impinging droplet with the center of the TFT array. Additionally, to control the frequency of the droplet formation a KD Scientific Legato 100 Series Syringe Pump was connected to the hypodermic needle

using a small diameter surgical tubing. This apparatus enabled the generation of impinging droplets accurately, with very high precision and at a consistent rate.

A high-speed camera (Phantom®) was used for digital image (and video) acquisition. Typical image acquisition rates ranged from 200-1000 fps. Image acquisition was initiated just prior to droplet impingement and was continued until the impinged droplet was completely evaporated. Time stamps were also recorded in each image. This was utilized subsequently to ensure the synchronization of temperature data acquisition with image acquisition. Additional details are provided in Chapter IV. The camera was mounted on a stage with a single axis for rotation. The camera angle was fixed at 12° to enable the visualization of the TFT junctions in the array. Additionally, back-side illumination was provided using a light source (Fiber Optic Illuminator Model 190). The UV light source (ThorLabs blue laser diode module, 405 nm illumination at an intensity of 4.0mW) was positioned above the TFT junctions and the UV light was focused at the location of the TFT junctions in the array. The chosen illumination wavelength was slightly higher than the illumination sources reported in the literature. For Hao and Liu's droplet impingement experiment a UV light source with peak wavelengths between 275-315 nm was used [3]. The implications of using a higher wavelength illumination source are discussed further in Chapter IV. It is also important to note that all devices were attached to an optics table, thereby eliminating any interference from structural vibrations in the building. A photograph of the test set-up is shown in Figure 2.16 and the schematic of the experimental apparatus is shown in Figure 2.17.

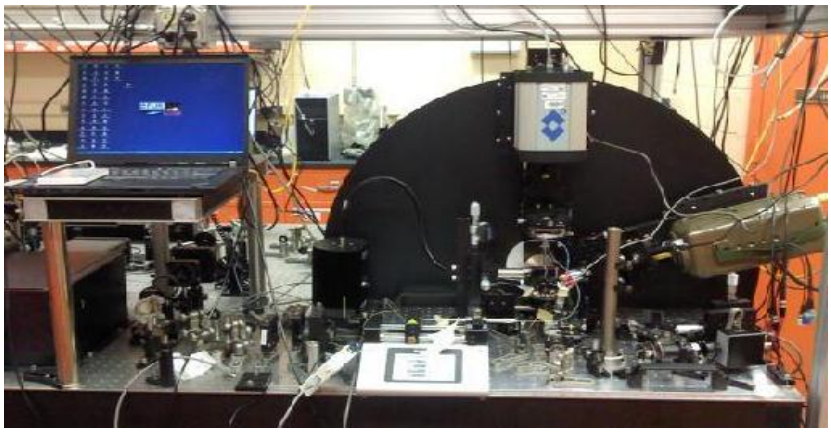

Fig. 2.16 Photograph of experimental apparatus 1 (at AFRL)

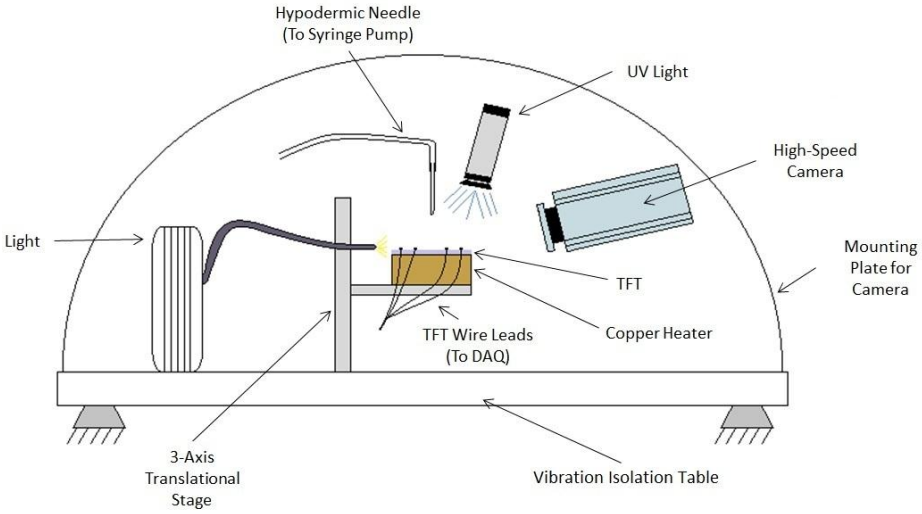

Fig. 2.17 Schematic of experimental apparatus 1 (at AFRL)

Experimental Apparatus 2 (TAMU)

The second experimental apparatus was located at Texas A&M University and was very similar to the apparatus at AFRL, however, different components were used to realize identical configuration of the experimental apparatus. The most noticeable difference between the two set-ups is the use of a higher power UV light (at TAMU), high-speed camera with higher frame rate capability but smaller onboard memory card (at TAMU), and the use of a hot plate (at TAMU) instead of a calorimeter apparatus with a copper block integrated with embedded heater (at AFRL). The high speed camera (at TAMU) was used to capture images at 25 fps (Model: Troubleshooter, Manufacturer: Fastec Imaging). The slower frame rate was used in order to accommodate the complete sequence of images required for capturing the complete evaporation of a single impinged droplet using a smaller onboard memory card (512 MB) that was available in the camera.

The UV light source (at TAMU) had an illumination power rating of 3W for a wavelength of 405nm. The intensity of the illumination was adjusted using a Newport ND filter which filtered approximately 50% of the UV light. Additionally, a Cole-Parmer hotplate (Model: Stable Temp; Rating: 120 V, 8.8 A) was used to heat the wafer (with TFT array) to a specified initial temperature. Thermal paste (Omegatherm 201) was used to minimize thermal resistance between the heater surface and the silicon wafer (similar to that used in Apparatus 1 at AFRL) and to mount the wafer to the surface of the hot plate (for better adhesion). A photograph of Apparatus 2 is shown in Figure 2.18 and corresponding schematic is shown in Figure 2.19.

Fig. 2.18 Photograph of experimental apparatus 2 (at Texas A&M University)

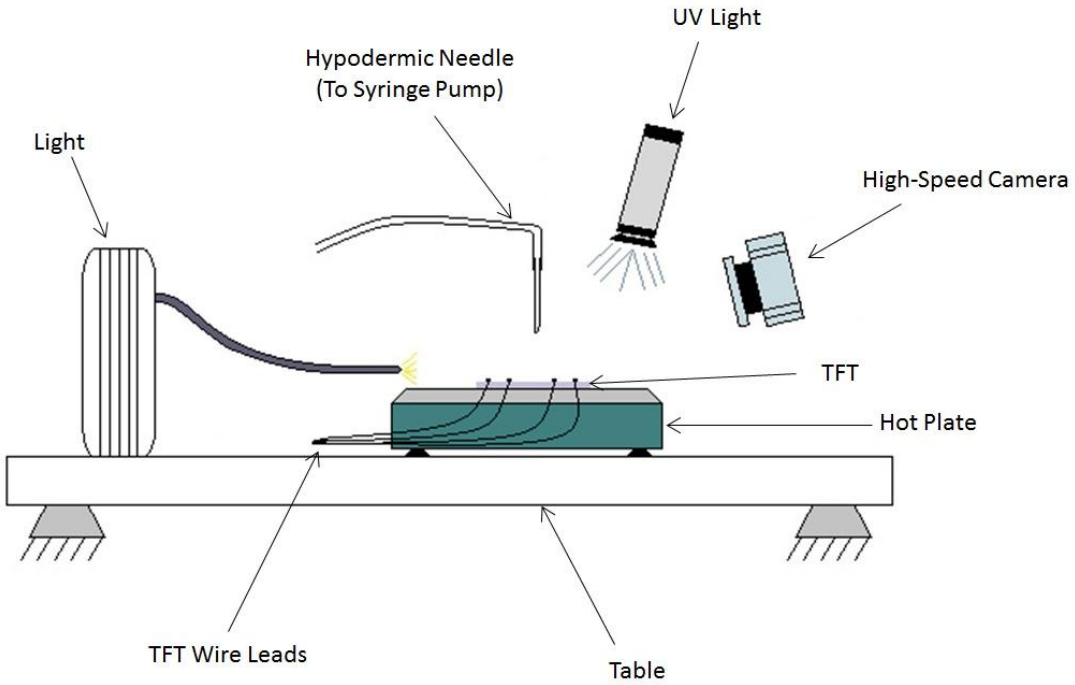

Fig. 2.19 Schematic of experimental apparatus 2 (at Texas A&M University)

Test Surface Preparation and Test Liquids

For both experimental apparatus (1 and 2) the wafer surfaces with packaged TFT array was rinsed with IPA for approximately thirty seconds followed by rinsing with DI water for thirty seconds. The wafer was then attached to the surface of the heater primarily by using thermal paste (as mentioned earlier in this chapter).

Due to constraints imposed by the high-speed camera, the test surface was not cleaned between each droplet impingement event, nor was the surface rotated so a different portion of the wafer could be exposed to a different droplet for each impingement. Therefore, a small "footprint" from the deposition (precipitation) can be noted in some of the recorded images. The precipitation of minute quantities of residues from a completely evaporated droplet for successive cycles of droplet impingement led to the formation of these small "footprints".

Ultra-pure water (at AFRL) and DI water (Texas A&M) were used as the test liquids.

Experimental Procedure

Droplet experiments were initiated after ensuring all TFT lead wires were connected to the DAQ, the video camera was in focus, the wafer (containing the TFT array) was securely mounted, and the hypodermic needle was aligned with the center of the TFT array. The following paragraph describes the sequence of steps implemented in the experimental procedure.

First, the Labview program was started to record transient voltage data. Next, the syringe pump was started with a very small volume flow rate. As the water was pumped, it accumulated on the tip of the hypodermic needle until the weight of the liquid exceeded the surface tension forces. Immediately before droplet impingement, video recording was started at an appropriate frame rate to ensure the entire droplet evaporation was recorded. After impingement, the syringe pump was stopped and after the droplet evaporated completely, data acquisition and video recording were stopped. Image and data files were saved with an appropriate filename that reflected the heater set-point, exposure, and droplet number. This process was then repeated for subsequent experiments. For experiments requiring exposure to UV light, the light was turned on approximately thirty minutes to one hour before droplet impingement experiments were initiated. The UV light source was powered on for the duration of the droplet experiments. The same experimental procedure was implemented in both experimental apparatus (1 and 2; at AFRL and TAMU, respectively).

CHAPTER III

DATA ANALYSIS

Thermal Data Analyses

The surface temperature data from the Thin Film Thermocouple (TFT) array that was recorded by the high-speed digital data acquisition system was analyzed to determine the heat transfer coefficients and heat flux values. Both local and global heat flux values were determined based on the surface temperature data. To determine local heat flux values, the "semi-infinite solid model" was used [79]. Global heat flux values were also calculated using experimental correlations for natural convection and using the surface temperature transient data [35]. It is important to note that all thermo-physical properties were obtained from property tables [79]. The semi-infinite solid model provides a useful idealization for this problem since the silicon wafer (the solid) is large (in comparison to the size of the water droplet). Thus, transient one-dimensional conduction occurs within the solid when a droplet impinges upon the surface. This assumption has also been used by Tio and Sadhal [27, 36], Sadhal and Plesset [25], and White and Tinker [80]. The analytical solution for a convective surface condition is as follows

$$\frac{T(x,t)-T_i}{T_\infty-T_i}=\operatorname{erfc}\left(\frac{x}{2\sqrt{\alpha t}}\right)-\left[\exp\left(\frac{hx}{k}+\frac{h^2\alpha t}{k^2}\right)\right]\left[\operatorname{erfc}\left(\frac{x}{2\sqrt{\alpha t}}+\frac{h\sqrt{\alpha t}}{k}\right)\right] \qquad (3)$$

where $T(x,t)$ is temperature at time t, T_i is initial temperature, T_∞ is room temperature, x is length, h is heat transfer coefficient, k is thermal conductivity of the silicon wafer, t is time, and α is absorptivity. On the wafer surface x is set to a value of zero and the following equation is derived from Equation 3, in order to obtain the convective heat

transfer coefficient (*h*) from the non-dimensional surface temperature (recorded by each TFT junction):

$$\frac{T(0,t)-T_i}{T_\infty-T_i}=1-\left[\exp\left(\frac{h^2\alpha t}{k^2}\right)\right]\left[\operatorname{erfc}\left(\frac{h\sqrt{\alpha t}}{k}\right)\right] \quad (4)$$

This is an implicit equation that can be solved by using an iterative procedure. Hence, this equation is solved for the heat transfer coefficient using the "fzero" Matlab® function, which is a root finding function allowing for quick and accurate solution of implicit (or non-linear) equations. This function begins with an initial guess (40,000 in this study) and uses iterative procedure to obtain the solution for the implicit equation. The typical solution procedure is highlighted in Tables 3.1 and 3.2 and the error associated with each iteration is shown in Figure 3.1. The solution was verified by substituting the root of the equation in Equation 4. In addition, custom codes were utilized to implement Newton-Raphson method and bisection methods as an additional verification for the solutions generated by the "fzero" function. Additionally, the heat transfer coefficient obtained from these methods was used in Equation 4 to calculate the temperature at each time step. This estimated value was compared to the experimental data to verify the accuracy of the solutions.

Table 3.1 Iterative solution procedure to determine root of Equation 4

Count	a	f(a)	b	f(b)	Procedure
1	40000	-0.187649	40000	-0.187649	Initial Interval
9	36800	-0.210437	43200	-0.166873	Search
17	27200	-0.293876	52800	-0.114427	Search
25	3796.13	***-1.20582***	91200	***0.00855024***	Search (Sign Change)
Initial Guess: 40,000					

Table 3.2 Solution procedure to determine root of Equation 4 using Matlab®

Iteration	Value	Error (%)	Method Used
1	91200	0.855024%	Initial
2	87199	-0.022113%	Interpolation
3	87299.2	0.000658%	Interpolation
4	87296.3	0.000001%	Bisection
5	87296.3	0.000000%	Interpolation
6	87296.3	0.000000%	Interpolation

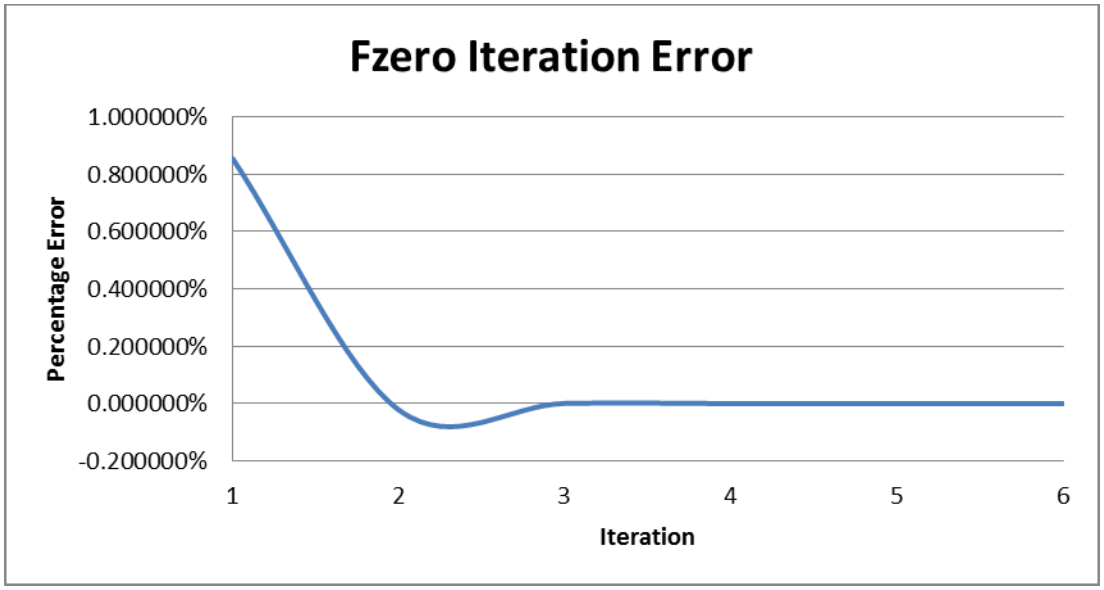

Fig. 3.1 Iteration error for calculating the roots of Equation 4.

After calculating the heat transfer coefficient from the experimental data, the heat flux values are calculated using the experimental data for surface temperature fluctuations, *T(t)*, as follows:

$$q''(t)=h[T(t)-T_{\infty}] \tag{5}$$

This calculation was repeated for all working TFT junctions on each wafer to obtain the local heat flux values at the location of the TFT junctions in the temperature nano-sensor array. The local heat flux values at the location of each TFT junction provides detailed insight about the temporal and spatial variation of heat transfer under an individual impinging droplet undergoing boiling and evaporation.

Global heat transfer coefficient and heat flux values were calculated using the following procedure [35]. An empirical correlation for Nusselt number (based on Rayleigh number) was used to determine the heat transfer coefficient for natural convection (prior to droplet impingement). This was used to estimate the contact resistance between the heater apparatus and the TFT array. The contact resistance value is used to estimate the two-phase heat flux values after droplet impingement occurs. Therefore, the first step in the calculation procedure for global heat flux is to determine the heat transfer coefficient for natural convection using the following equation:

$$h_{nc}=\frac{k_{air}*Nu_{nc}}{L_c}\ \left[\frac{W}{m^2K}\right] \tag{6}$$

where L is the characteristic length (surface area divided by perimeter) of the silicon wafer and Nu_{nc} is defined as:

$$Nu_{nc}=0.54*Ra^{0.25}\ \left(10^4\leq Ra\leq 10^7\right) \tag{7}$$

This correlation is derived from experimental results compiled by Lloyd and Moran [81]. Ra is defined as the Rayleigh number and can be calculated as

$$Ra=\frac{g\beta(T_{tft,avg}-T_{\infty})L^3}{\nu\alpha} \tag{8}$$

where $T_{tft,avg}$ is the average surface temperature of the TFT prior to droplet impingement, ν is kinematic viscosity of air, β is thermal expansion coefficient of air, and g is gravity. The value of natural convection heat flux (single-phase regime) was calculated by multiplying the natural convection heat transfer coefficient by the change in temperature between room temperature and the average of the temperature recorded by the TFT array prior to droplet impingement, as:

$$q''_{nc}=h_{nc}\left(T_{tft,avg}-T_{\infty}\right)\left[\frac{W}{m^2}\right] \tag{9}$$

Now, thermal contact resistance between the heater and the wafer can be calculated as

$$R_c=\frac{T_{heater}-T_{tft,\,avg}}{q''_{nc}}\left[\frac{m^2K}{W}\right] \tag{10}$$

where T_{heater} is the heater set-point temperature (for the hot plate). With the contact resistance known, the two-phase heat flux can be found as

$$q''_{2\text{-}phase}=\frac{T_{heater}-T_{tft}(t)}{R_c}\left[\frac{W}{m^2}\right] \tag{11}$$

where $T_{tft}(t)$ is the value of the surface temperature transient data recorded by each TFT in the array. Two different calculations were used to calculate the heat transfer coefficient, each calculation was dependent on the initial temperature values. For experiments involving surface temperature values less than the saturation temperature:

$$h_{2\text{-phase}} = \frac{q''_{2\text{-phase}}}{T_{tft}(t) - T_{room}} \left[\frac{W}{cm^2 K}\right] \quad (12)$$

For experiments involving surface temperature values higher than the saturation temperature:

$$h_{2\text{-phase}} = \frac{q''_{2\text{-phase}}}{T_{tft}(t) - T_{sat}} \left[\frac{W}{cm^2 K}\right] \quad (13)$$

Using Equations 6 through 13, a Matlab code was used to determine the global transient heat transfer coefficients and transient values of heat flux for all of the droplet impingement experiments.

Non-Dimensional Analysis

To non-dimensionalize data reported in this study and determine relationships between parameters of the system, the Buckingham Pi Theorem was used. The goal of this study was to estimate the transient heat flux as a function of various experimental parameters. The heat flux was affected by several properties of the liquid which included droplet impact velocity, droplet radius (corresponding to surface area), density change between the liquid droplet and surrounding gas medium, surface tension, dynamic viscosity, specific heat, latent heat of vaporization, saturation temperature, and superheat temperature. These are represented, respectively, by

$$q'' = f(v, r, \Delta\rho, g, \sigma, \mu, C_p, h_{fg}, T_{sat}, \Delta T) \quad (14)$$

The π-groups that will be determined are a function of these variables. From these ten dimensional parameters (n=10), four primary dimensions are determined (r=4),

corresponding to mass, length, time, temperature ([M], [L], [t], [C], respectively). Thus, four repeating parameters are selected (m=r=4) which are $v, r, \sigma, \Delta T$. This set (m) of parameters includes the four primary dimensions of [M], [L], [t], and [C]. With these parameters selected, six π-groups can be calculated. The first π-group is determined to be the Weber number and is expressed as:

$$\pi_1=\mathrm{We}=\frac{\rho v^2 r}{\sigma} \tag{15}$$

where *r* is a characteristic length, typically the droplet diameter. This dimensionless number relates the drop's inertia to its surface tension and indicates that the larger the surface tension, the larger impact velocity to break the droplet apart.

The next π-group is determined to be the Bond number, which is

$$\pi_2=\mathrm{Bo}=\frac{gL^2(\rho_l-\rho_g)}{\sigma} \tag{16}$$

where ρ_l is the density of the droplet, ρ_g is the density of the surrounding medium, *L* is the droplet diameter (which is substituted by *r*, the radius). This non-dimensional parameter is the ratio of gravitational forces to surface tension forces.

The third π-group is the well-known Reynolds number. This number is a measure of the ratio of the inertial forces to viscous forces, and is expressed as:

$$\pi_3=\mathrm{Re}=\frac{\rho v D}{\mu} \tag{17}$$

In this case *r*, for radius, is substituted by D, the diameter of the droplet.

The fourth π-group is the Jakob number. This non-dimensional quantity is the ratio of the sensible heat content to the latent heat content (two-phase), and is expressed as:

$$\pi_4=Ja=\frac{C_{pf}(T_{sat}-T_{wall})}{h_{fg}} \tag{18}$$

The fifth π-group (Equation 19) corresponds to the ratio of droplet impact velocity to latent heat of vaporization and the sixth π-group (Equation 20) corresponds to a relation in the temperature change into the system to the saturation temperature of the liquid. These two π-groups were found to be

$$\pi_5=\frac{v^2}{h_{fg}} \tag{19}$$

$$\pi_6=\frac{\Delta T}{T_{sat}} \tag{20}$$

The Weber, Bond, Reynolds, and Jakob numbers are calculated for each droplet impingement experiment and values can be found in Appendix D.

CHAPTER IV

RESULTS AND DISCUSSION

Two sets of experiments were performed in this study. The first set of experiments was performed at the Air Force Research Lab. In these experiments droplet impingements on uncoated (unexposed) and TiO_2 coated (unexposed and exposed) wafers were studied. The second set of experiments was conducted at Texas A&M University. The experiments were performed by exposing an uncoated wafer (with TFT) to varying intensities of UV light during droplet impingement. The second set of experiments served as control to obtain base-line data. These experiments were performed to verify if the intensity of UV light affects heat flux on uncoated silicon wafers. A summary of the experiments conducted at Texas A&M is listed in Table 4.1 and experiments conducted at AFRL are listed in Table 4.2. It is important to note that the highlighted cells in Table 4.2 indicate that high-speed video and temperature data was captured for these droplets. For un-highlighted cells in Table 4.2, only temperature data is recorded. High speed imagery at 25 fps was captured for all experiments performed at Texas A&M University.

The experimental parameters consisted of a series of three droplets at four different heater set-point temperatures were conducted and at three different values of intensity of exposure to UV illumination. For the UV illumination: 0% exposure indicates the UV light is off during droplet impingement; 50% indicates the wafer was exposed to 50% of the 3 Watt intensity of the bulb, and 100% indicates full exposure to the UV light. This exposure rate was controlled by attaching a ND filter onto the UV light source, thus

reducing the intensity of the light. Four of the data points resulted in aberrant behavior which was caused by potential malfunctioning of the TFT sensor, possibly due to silver paste reaching a melting point at the higher temperatures for which the experiments were conducted.

Experiments at AFRL were conducted at four different set-points for the heater temperature (i.e., initial heater steady state temperature). For the uncoated wafer at 121°C only one drop was recorded. This was due to the TFT, again, behaving erratically and resulting in very inconsistent temperature data for recording of the surface temperature data for further droplet impingements. Thus, experiments extending beyond heater temperature of 121°C were not completed.

Measurement uncertainty was estimated using the Kline and McClintock method, for the droplet impingement experiments for both local and global heat flux values. Local uncertainty ranged from 14-24% while global uncertainty ranged from 16-27% for both experimental set-ups. A more detailed discussion of measurement uncertainty is provided in Appendix C. These uncertainty values are indicated by error bars in the plots showing the average value of heat flux.

Table 4.1 Summary of droplet experiments at Texas A&M for bare wafer (uncoated wafer)

	Heater Set-Point			
	105°C	110°C	115°C	120°C
0%	Bad Data	Drop 1	Bad Data	Drop 1
	Drop 2	Drop 2	Drop 2	Drop 2
	Drop 3	Drop 2	Bad Data	Drop 3
50%	Drop 1	Drop 1	Bad Data	Drop 1
	Drop 2	Drop 2	Drop 2	Drop 2
	Drop 3	Drop 3	Drop 3	Drop 3
100%	Drop 1	Drop 1	Drop 1	Drop 1
	Drop 2	Drop 2	Drop 2	Drop 2
	Drop 3	Drop 3	Drop 3	Drop 3

Table 4.2 Summary of droplet experiments at AFRL (blue highlight indicates video data available)

	Heater Set-Point			
	105°C	115°C	121°C	131°C
Uncoated	Drop 1	Drop 1	Drop 1	
	Drop 2	Drop 2		
	Drop 3	Drop 3		
	Drop 4	Drop 4		
		Drop 5		
Unexposed	Drop 1	Drop 1	Drop 1	Drop 1
	Drop 2	Drop 2	Drop 2	Drop 2
		Drop 3	Drop 3	Drop 3
			Drop 4	
			Drop 5	
Exposed	Drop 1	Drop 1	Drop 1	Drop 1
	Drop 2	Drop 2	Drop 2	Drop 2
	Drop 3	Drop 3	Drop 3	Drop 3
	Drop 4	Drop 4	Drop 4	Drop 4
	Drop 5	Drop 5	Drop 5	Drop 5
			Drop 6	
			Drop 7	
			Drop 8	

Droplet Impingement Results at Texas A&M (Control Experiments, Bare Wafer)

Using the equations discussed in Chapter III, the local and global heat flux values were calculated using the transient data recorded by each functioning TFT in the array. These experiments were conducted for bare wafers (without any nanocoatings). The TFT used for these experiments had two working junctions, 3 and 4, indicated by J.3 and J.4. Time averaged values of heat flux (as well as maximum values of heat flux) were plotted as a function of heater temperature (initial steady-state value of heater temperature) for these junctions (both individual values and junction averaged values). This provided insights about heat flux values at different exposure levels and temperatures.

Contact angles were measured using ImageJ image analysis software. Contact angle measurements were made immediately after droplet impact and after the surface oscillations had subsided, but before commencement of nucleate boiling, thus ensuring consistent results from drop to drop. Additionally, measurements were obtained for each image for both contact angles on the left and right side. Some of the droplets were larger than the field of view of the camera. In these cases, only the left side contact angle was measured. These values of contact angle are plotted in Tables 4.3 and 4.4. The values listed in the tables show that the measured values of contact angle are unaffected by the intensity of exposure to UV illumination source and temperature of the heater. Additionally, the results show that the standard deviation of the left side contact angle is 2.2° while the standard deviation of the right side is 5.5°. Hence, the measured values of it can be concluded that contact angle does not change with varying UV light intensities (for the uncoated wafers).

Table 4.3 Contact angle measurements for the left side of droplet, uncoated (°)

	Temperature (°C)			
	105	110	115	120
0%	63	66	68	70
	67	65	69	69
	67	69	63	67
50%	65	68	66	68
	65	67	67	68
	65	65	69	72
100%	66	62	63	68
	67	65	68	68
	67	64	63	68

Table 4.4 Contact angle measurements for the right side of droplet, uncoated (°)

	Temperature (°C)			
	105	110	115	120
0%	70	71	65	
	66	68	74	
	71	67	70	
50%	77	79	78	
	78	79	77	
	79	77	78	
100%				

In addition to contact angle, it is desirable to investigate impact velocity which has been shown to affect heat flux [3, 9]. However, due to the low speed of image capture (25 fps), images could not be analyzed for determining the impact velocity and the corresponding Weber number. However, as all experiments were conducted over the course of one day, the height of the hypodermic needle did not change. Thus, it was assumed that the impact velocity between droplets was similar and within acceptable range. Similarly, since the same TFT sensor array was used for all experiments the surface

roughness is assumed to remain fairly constant over the duration of experimentation. However, surface roughness may have increased with use, due to any precipitation of dissolved impurities in the water that could be deposited on the heater surface after repeated impingement and evaporation of a series of droplets at different heater temperatures.

Time-Averaged Heat Flux (Local and Global)

The time-averaged values of local heat flux and global heat flux at different intensities of UV illumination were plotted (as shown in Figures 4.1 – 4.4 as well as listed in Tables 4.5 and 4.6). These values were calculated using methods discussed in Chapter III. As shown in Figure 4.2 and the values listed in Table 4.5, the values of local heat flux at similar heater temperatures at various exposure rates are virtually unchanged. The average values of the local and global heat flux are found to increase monotonously with heater temperature (i.e., the initial steady state values of the heater temperature). The average variation is ~2.0% between all drop impingements with a maximum change of 24%. Additionally, the max standard deviation is within 18%. This result is expected since there is no significant change in contact angle, impact velocity, and surface roughness.

Time averaged values of global heat flux, shown in Figures 4.3 and 4.4 as well as listed in Table 4.6, remains at similar heater temperatures at various exposure rates are also virtually unchanged. The average difference is ~13% and the maximum difference in the global heat flux values is ~35%. One can note that as temperature increases, data points appear more scattered. This uncertainty is due to larger fluctuations in initial temperature.

Additionally, as the heater temperature increases, the phase change process for droplet impingement cooling (as well as bubble nucleation and departure cycles within the droplets) is associated with higher magnitudes of surface temperature fluctuations. Thus, larger fluctuations in heat flux may occur. Additionally, standard deviations within this data are large, up to 28%. Hence this data set shows that for the control experiments, no appreciable change in heat flux values (local and global heat flux) were observed with or without exposure to UV illumination.

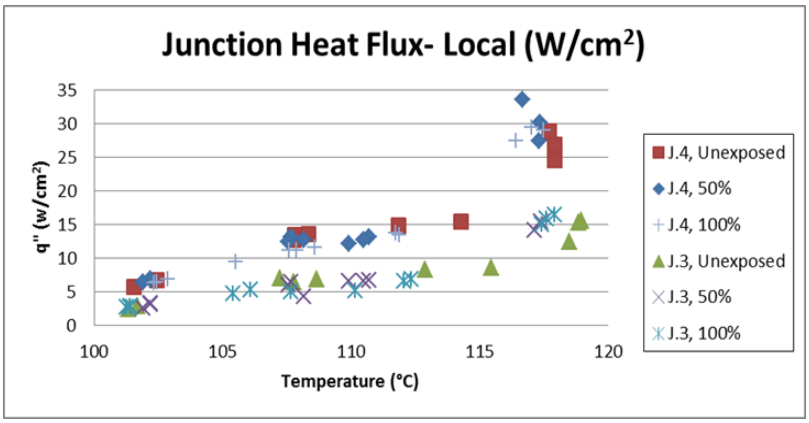

Fig. 4.1 Local time-averaged heat flux values for individual TFT junctions plotted as a function of heater temperature (bare wafer).

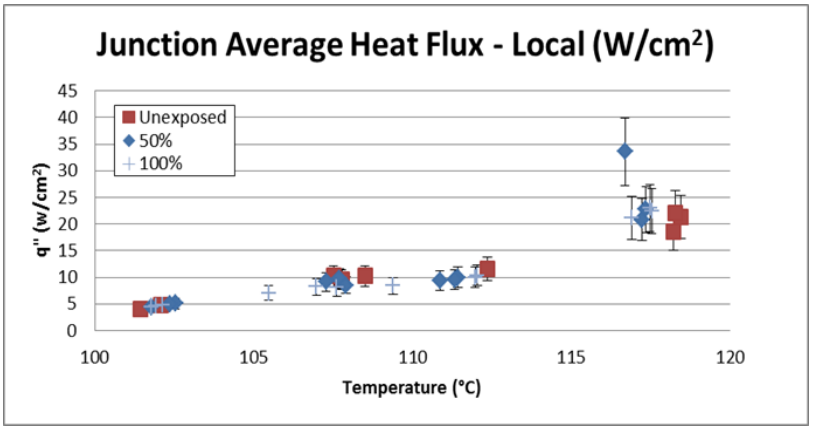

Fig. 4.2 Local time-averaged heat flux values (average for all TFT junctions) plotted as a function of heater temperature.

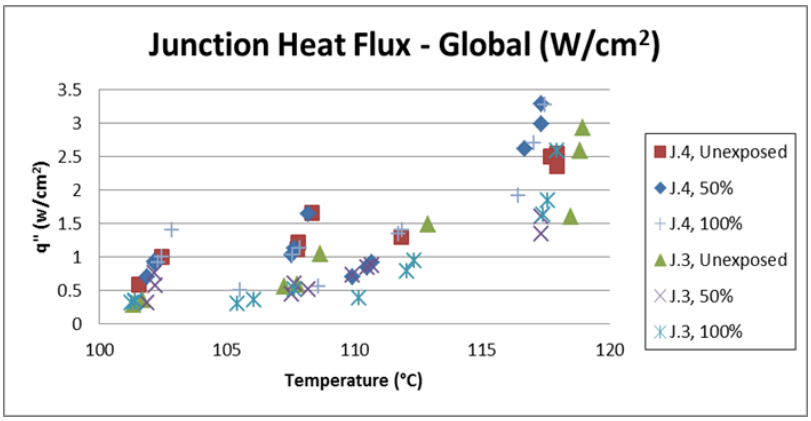

Fig. 4.3 Global time-averaged heat flux values for individual TFT junctions plotted as a function of heater temperature.

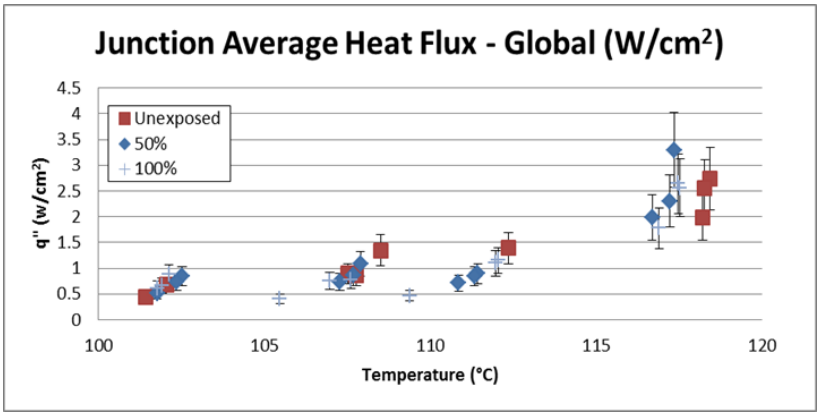

Fig. 4.4 Global time-averaged heat flux values (average for all TFT junctions) plotted as a function of heater temperature.

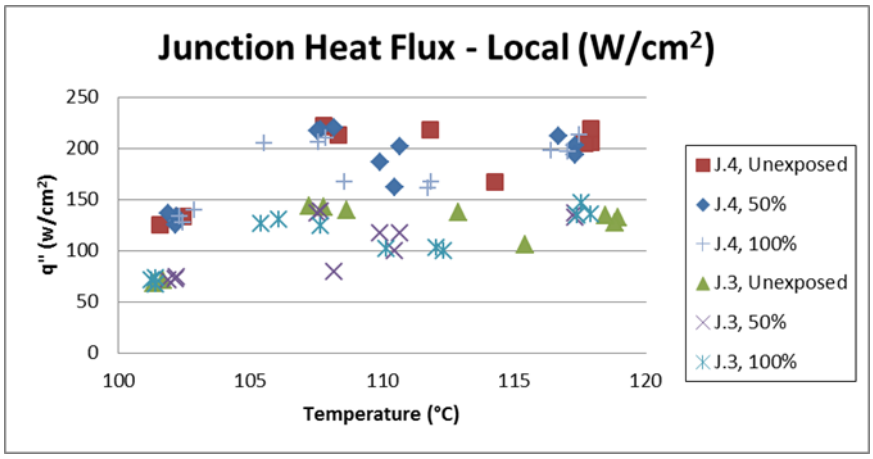

Fig. 4.5 Local maximum heat flux values for individual TFT junctions plotted as a function of heater temperature.

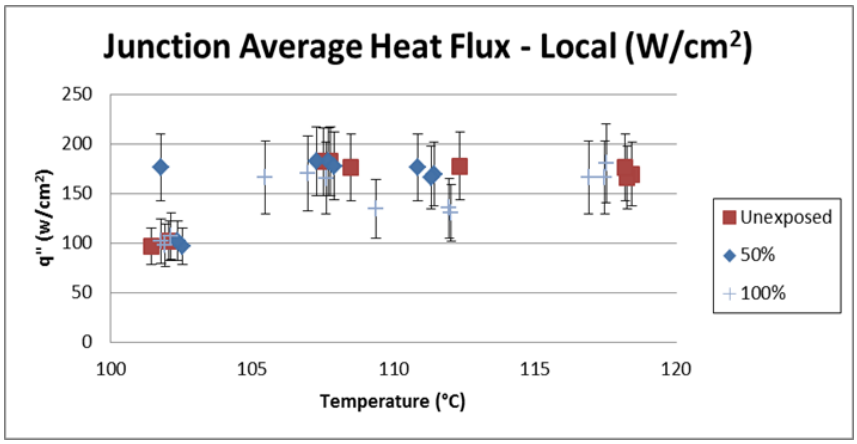

Fig. 4.6 Local maximum heat flux values (average for all TFT junctions) plotted as a function of heater temperature.

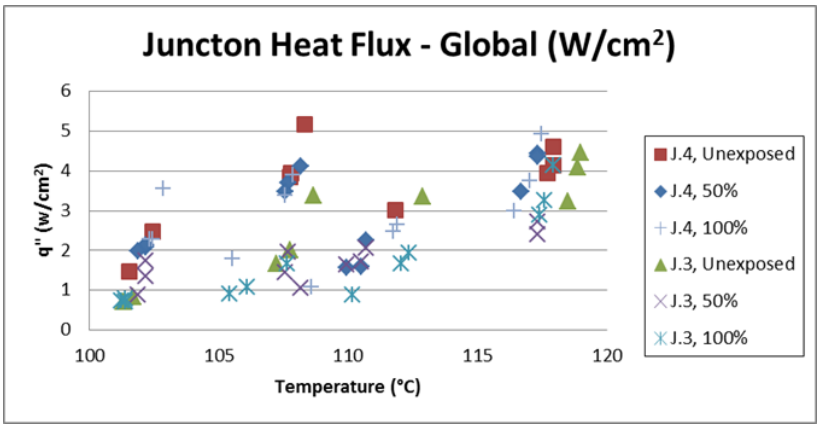

Fig. 4.7 Global maximum heat flux values for individual TFT junctions plotted as a function of heater temperature.

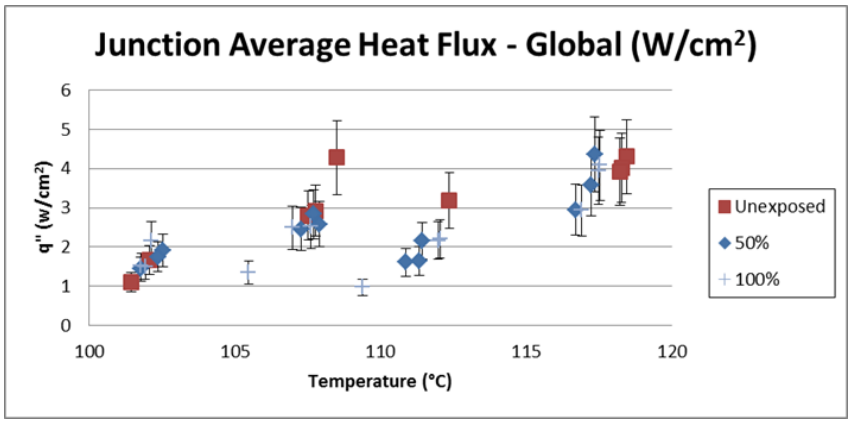

Fig. 4.8 Global maximum heat flux values (average for all the TFT junctions combined) plotted as a function of heater temperature.

Table 4.5 Change in local time-averaged heat flux values (average of all TFT junctions) at similar heater temperatures (initial steady state values)

Exposure Rates at Similar Temperature (°C)						*Percent Increase*		
Temp.	0%	Temp.	50%	Temp.	100%	0% -50%	0% -100%	50% -100%
101.4	4.1	101.8	4.5	101.8	4.5	10.7%	10.3%	-0.3%
102.1	4.8	102.4	5.0	102.1	4.9	5.5%	2.5%	-2.9%
107.5	10.3	107.7	9.8	107.6	8.1	-4.9%	-21.5%	-17.4%
112.4	11.6	111.4	10.0	112.0	10.0	-14.2%	-14.0%	0.2%
118.2	18.5	117.2	20.8	117.5	22.9	12.6%	24.0%	10.1%
					Average	***2.0%***	***0.3%***	***-2.1%***
					Std. Dev.	***11.3%***	***18.3%***	***9.9%***

Table 4.6 Change in global time-averaged heat flux values (average of all TFT junctions) at similar heater temperatures (initial steady state values)

Exposure Rates at Similar Temperature (°C)						*Percent Increase*		
Temp.	0%	Temp.	50%	Temp.	100%	0% -50%	0% -100%	50% -100%
101.4	0.4	101.8	0.5	101.8	0.6	16.2%	39.8%	20.3%
102.1	0.7	102.4	0.7	102.1	0.9	8.0%	28.6%	19.1%
107.5	0.9	107.7	0.9	107.6	0.8	-3.7%	-14.0%	-10.7%
112.4	1.4	111.4	0.9	112.0	1.1	-35.8%	-21.2%	22.8%
118.2	2.0	117.2	2.3	117.5	2.6	15.9%	33.1%	14.8%
					Average	***0.1%***	***13.3%***	***13.2%***
					Std. Dev.	***21.6%***	***28.6%***	***13.7%***

Table 4.7 Change in local maximum heat flux values (average for all TFT junctions) at similar heater temperatures (initial steady state values)

Exposure Rates at Similar Temperature (°C)						*Percent Increase*		
Temp.	0%	Temp.	50%	Temp.	100%	0% -50%	0% -100%	50% -100%
101.4	97.0	102.4	104.4	101.8	102.4	7.6%	5.6%	-1.9%
102.1	102.6	101.8	104.0	102.1	107.0	1.4%	4.3%	2.9%
107.5	182.3	107.7	179.1	107.6	165.7	-1.7%	-9.1%	-7.5%
112.4	178.2	111.4	159.9	112.0	135.4	-10.3%	-24.0%	-15.3%
118.2	177.0	117.2	170.1	117.5	166.3	-3.9%	-6.0%	-2.2%
					Average	***-1.4%***	***-5.9%***	***-4.8%***
					Std. Dev.	***6.6%***	***12.0%***	***6.9%***

Table 4.8 Change in global maximum heat flux values (average for all TFT junctions) at similar heater temperatures (initial steady state values)

Exposure Rates at Similar Temperature (°C)						*Percent Increase*		
Temp.	0%	Temp.	50%	Temp.	100%	0% -50%	0% -100%	50% -100%
101.4	1.1	102.4	1.7	101.8	1.5	59.2%	38.4%	-13.1%
102.1	1.7	101.8	1.4	102.1	2.2	-13.8%	30.2%	51.0%
107.5	2.8	107.7	2.8	107.6	2.5	1.2%	-10.3%	-11.4%
112.4	3.2	111.4	2.2	112.0	2.2	-32.4%	-32.1%	0.5%
118.2	3.9	117.2	3.6	117.5	3.9	-8.7%	0.6%	10.2%
					Average	***1.1%***	***5.4%***	***7.5%***
					Std. Dev.	***34.7%***	***29.1%***	***26.1%***

Maximum Value of Heat Flux (Local and Global)

In addition to time-averaged heat flux, maximum heat flux values were also identified from the data sets (both for local and global heat flux values). The results for local values of maximum heat flux are plotted in Figures 4.5 and 4.6 as well as listed in Table 4.7. The results for global values of maximum heat flux are plotted in Figures 4.7 and 4.8 as well as listed in Table 4.8.

Figure 4.6 shows that maximum heat flux remains fairly constant over the range of heater temperatures in the experiments. This is because the maximum heat flux is weakly sensitive to the initial values of surface temperature and is more sensitive to the surface conditions. Therefore, with higher initial values of heater temperature, maximum values of heat flux remains almost unchanged. However, data points at 100°C are significantly below the typical values for other experimental data. This could be due to smaller droplet volume, since the droplet volumes for these experiments range from ~2.4 - 2.9 mm^3, while for other experiments the droplet volumes range from ~2.5 - 4.0 mm^3 (this data can be found in Appendix D). For droplets with smaller mass (and diameter) the impact force of the impinging droplet and the contact area of the impinged droplets on the heater surface are reduced which may result in lower values of maximum heat flux (that occurs during impingement). Additionally, Table 4.7 shows that the maximum difference between heat flux data at similar temperatures is around ~24% while the average difference is ~5%. The maximum standard deviation is ~12% while the nominal value of standard deviation is ~7%. Hence the data shows that the local maximum values of heat transfer do not change appreciably, with or without exposure to different intensities of UV illuminations.

Global maximum values of heat flux data are plotted in Figures 4.7 and 4.8 as well as summarized in Table 4.8. There is larger variation in the global maximum heat flux values than the time-averaged data for global heat flux values. The data summarized in Table 4.8 shows the average change of about 6% while the maximum of change is ~30%. As with global time-averaged values of heat flux, the standard deviations for the global maximum values of heat flux are also significantly large (26% - 35%). Hence, the large values of standard deviation indicate that there is no perceptible increase in maximum values of global heat flux with or without exposure to different levels of exposure to UV illumination.

Droplet Impingement Results at AFRL

Equations presented and discussed in Chapter III for calculating local and global values of heat flux were used for post-processing of the experimental measurements conducted at AFRL. In these experiments nanocoating of TiO_2 was applied on the wafer with TFT array. The wafer used in these experiments consisted of three working TFT junctions: J.1, J.3, and J.6 (while for the uncoated wafer used in the experiments at Texas A&M University had only two of working junctions: J.1 and J.4). Time averaged values of heat flux (as well as maximum values of heat flux) were plotted as a function of heater temperature (initial steady-state value of heater temperature) for these junctions.

Contact angle of the droplets on the wafer surface were also measured. Contact angles were measured using ImageJ image processing software. Contact angle measurements were made immediately after droplet impact and after the oscillations

subsided but before commencement of onset of nucleate boiling (for each droplet impingement experiments). Additionally, measurements for contact angle were performed for both left and right side of each droplet in the experiments. A summary of the measurements of the contact angles for each individual droplet is listed in Appendix D and a summary of the contact angles measured (averaged values) are listed in Tables 4.9 and 4.10. This data indicates that the TiO_2 nano-coatings resulted in a decrease in contact angle by ~15-20% (representing a nominal decrease in the average values of contact angle by ~10-13° over that of the unexposed wafer). In addition, exposing the wafer to UV light decreases the contact angle by ~10%, (representing a nominal decrease in the average values of contact angle by ~ 5-10° over that of the unexposed wafer with nanocoating). One possible reason for the smaller change in contact angle (compared to those reported in the literature for similar experiments) is because the wavelength of the UV light source was 405 nm). This value of wavelength is slightly higher compared to the ideal range of required wavelength for photo-activation of TiO_2 nanocoating. A previous droplet impingement study activated titanium dioxide with a smaller wavelength at 275-315 nm, which transitioned the coating to hydrophilic [19]. Additionally, an organic chemistry journal reported that TiO_2 coatings are activated at a wavelength of 387 nm [82]. Hence, alternate light sources with different values of illumination wavelength could have provided better results for change in contact angle on photo-activation of the nanocoatings.

Table 4.9 Change in average contact angle for bare wafer and wafer with nanocoating of TiO_2 (measurements were performed for both left side and right side of each droplet)

	Left	Right
Uncoated	78.24	79.96
Unexposed	65.22	69.11
% Decrease	**19.96%**	**15.70%**

Table 4.10 Change in average contact angle for wafer with nanocoating of TiO_2 for unexposed and exposure to UV illuminations (measurements were performed for both left side and right side of each droplet)

	Left	Right
Unexposed	65.22	69.11
Exposed	59.58	61.71
% Decrease	**9.47%**	**11.99%**

The mass of each droplet was determined by measuring the volume of the droplet while in free-fall between the needle and the heated surface (spherical form) and multiplying by the density of water at room temperature. Mass of each droplet was very fairly uniform. The mass of each droplet was estimated to range from 3.7 to 4.5 mg with a standard deviation of 0.21 mg. More complete and detailed information on droplet mass and volume is provided in Appendix D.

Impact velocity of each droplet was also fairly uniform for these experiments involving wafers with nanocoatings as Table 4.11 highlights. Typical Weber numbers for the experiments are about 0.02-0.1, except for unexposed experiments performed for a heater initial steady state temperature of 131°C (for wafers with nanocoatings). These experiments were performed at Weber numbers of ~0.6-0.7. In contrast the Weber number for experiments performed with bare (uncoated) wafers is ~50-90% lower. Hence,

since exposed wafers (with nanocoatings) have slightly higher impact velocities, their heat transfer rates may be marginally higher.

Table 4.11 Impact velocity and corresponding Weber numbers

Titanium Dioxide: Unexposed			Titanium Dioxide: Exposed			Uncoated: Exposed		
Drop	Velocity (mm/s)	Weber #	Drop	Velocity (mm/s)	Weber #	Drop	Velocity (mm/s)	Weber #
105C			105C			105C		
Drop 1	16	0.01	Drop 1	53	0.12	Drop 1	21	0.02
Drop 2	25	0.02	Drop 4	*Not Available*		Drop 2	41	0.07
115C			Drop 5	30	0.04	115C		
Drop 1	55	0.12	115C			Drop 1	25	0.03
Drop 2	50	0.12	Drop 1	56	0.13	Drop 3	23	0.02
Drop 3	46	0.09	Drop 3	56	0.14	Drop 4	30	0.04
121C			Drop 5	93	0.38	Drop 5	25	0.03
Drop 1	78	0.09	121C			121C		
Drop 5	38	0.06	Drop 5	38	0.06	Drop 1	30	0.04
131C			Drop 7	55	0.13	**Average**	**28**	**0.03**
Drop 1	138	0.72	131C					
Drop 3	131	0.66	Drop 1	47	0.09			
Average	**64**	**0.2104**	Drop 5	46	0.08			
			Average	**53**	**0.13**			

In addition to impact velocity and contact angle, surface roughness of both the coated and uncoated wafers was measured after the conclusion of the experiments. The measurements were performed at the Material Characterization Facility (MCF) at Texas A&M University using Atomic Force Microscopy (AFM) in topography mode (NScriptor, NanoInk Inc., Skokie, IL). While this system is traditionally used for dip pen nanolithography, it has the capability of operating in an atomic force microscopy (AFM) mode in which a cantilever (scanning probe) scans the surface, generating roughness data and a nanoscale topography image of the surface. The details of the measurements are provided in Appendix B. Scan sizes ranging between 50-100 microns were completed at the location of the individual TFT junctions and at the center of the wafer (in between the TFT junctions). The results show that uncoated wafers have significantly lower levels of

surface roughness than for the wafers with nanocoatings. The root mean square values of surface roughness for uncoated wafers ranged from 62 nm – 86 nm, with peak values as high as ~1,000 nm. By contrast, for the coated wafers, the root mean square values of surface roughness ranged from 104 nm - 315 nm with typical peak values from ~2,000 nm – 3,000 nm (one sample showed a peak value at ~6,000 nm). Additionally, nano-scale surface cracks were observed in the wafer with nanocoatings. These are presumed to be cracks in the glass coating and are approximately ~300 nm thick (including the thickness of TiO_2 coating). The existence of surface cracks caused an increase in the effective surface roughness of the wafers with nanocoatings which could serve as sites for bubble nucleation (thus enhancing bubble nucleation site density) and could potentially skew the results for higher heat flux values.

Based on the surface roughness measurements performed using AFM, the enhancement of the effective surface area was found and compared to the plan (projected) area of the uncoated surface. The estimates for the increased surface area are listed in Table 4.12. The results in the table and indicate the surface area is significantly increased between uncoated and coated wafers. The percentage increase in surface area for uncoated wafers ranges from a 1-5% (compared to that of a completely smooth and flat surface). However, the percentage increase for coated wafers is much greater, ranging from 5-34%. The nano-scale protrusions (roughness) act as nano-fins and increase the surface area available for heat transfer to the liquid droplet. This phenomenon is termed as the “nano-fin effect” and has been described in earlier experiments involving pool boiling heat transfer for wafers with carbon nanotube coatings [44, 45]. In addition to the nano-fin

effect, increase in surface roughness also causes enhancement of the nucleation site density of the bubbles formed within the impinged droplet.

Table 4.12 Comparison of effective surface area (S3A) with the plan area (S2A) for wafers with nanocoaters and bare wafers, respectively (based on measurements for surface roughness)

	Location (Scan Length)	S2A (nm^2)	S3A (nm^2)	Pecent Increase
Uncoated	J.4 (100um)	1.0E+04	1.0E+04	1%
	J.2 (100um)	1.0E+10	1.0E+10	2%
	Center (50um)	2.5E+09	2.6E+09	5%
Coated	Center (100um)	1.0E+10	1.2E+10	16%
	Center (50um)	2.5E+09	3.3E+09	34%
	J.1 (50um)	2.5E+09	2.6E+09	5%
	J.3 (50um)	2.5E+09	2.6E+09	4%
	J.6 (50um)	2.5E+09	2.7E+09	10%

Time-Averaged Heat Flux (Local and Global)

The time-averaged values of local heat flux and global heat flux at different intensities of UV illumination were plotted (as shown in Figures 4.9 – 4.12 as well as listed in Tables 4.13 – 4.16). These values were calculated using methods discussed in Chapter III.

A large increase in the mean values for heat flux data is observed between coated and uncoated wafers (Figure 4.10). Locally, the heat flux value increases approximately 675-860% from uncoated to coated (unexposed and exposed, respectively), as shown in Table 4.13. However, there is a small increase between coated exposed and unexposed, an average of about 26% with a standard deviation of 22% (Table 4.14). With the outlier 1.15% removed standard deviation decreases to 20% and average heat flux increases to

30%. With this value not taken into consideration, it can be concluded that a marginal reduction in contact angle (less than 10°) causes an enhancement in the local time-averaged heat flux by about 25%. Additionally, it is important to note that the heat flux increase between uncoated and coated (unexposed and exposed) is not necessarily indicative of an increase strictly from exposure to UV light. As stated above, surface roughness (nano-fin effect and enhancement of nucleation site density) may play a more dominant role in enhancing the heat flux for coated wafers. With this taken into consideration it can be concluded that local, time-averaged heat flux increases from uncoated to coated by 675% and 860% for unexposed and exposed, respectively.

Increase in global heat flux from uncoated to coated (both unexposed and exposed) wafers was found to be approximately 275%. However, no significant increase in heat flux values for coated wafers was observed between unexposed and exposed cases. As with local values, this large increase may result in part from the increase in surface roughness of the wafer. With this data, it can be concluded that an increase in surface roughness and exposure to UV light results in a 275% increase in global time-averaged heat flux data when comparing an uncoated wafer to coated wafer (both unexposed and exposed). Additionally, exposure to UV light has no perceptible impact on the time-average values of global heat flux.

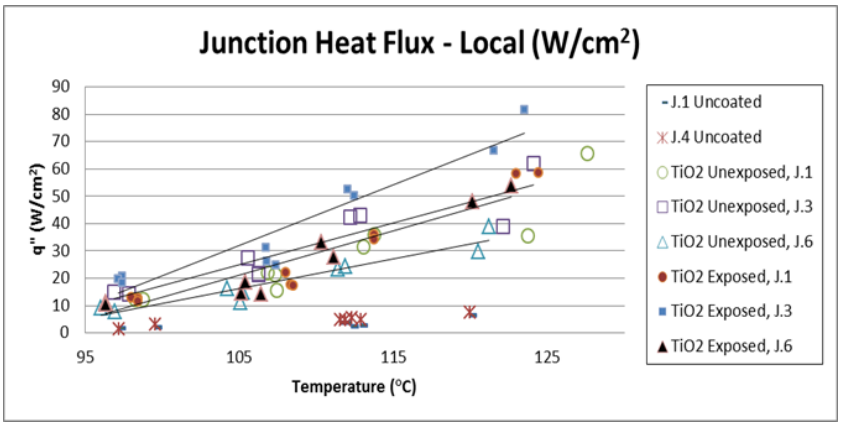

Fig. 4.9 Local time-averaged heat flux values for individual TFT junctions plotted as a function of initial TFT temperature (comparison of bare wafer and wafer with nanocoating: unexposed and exposed to UV illumination).

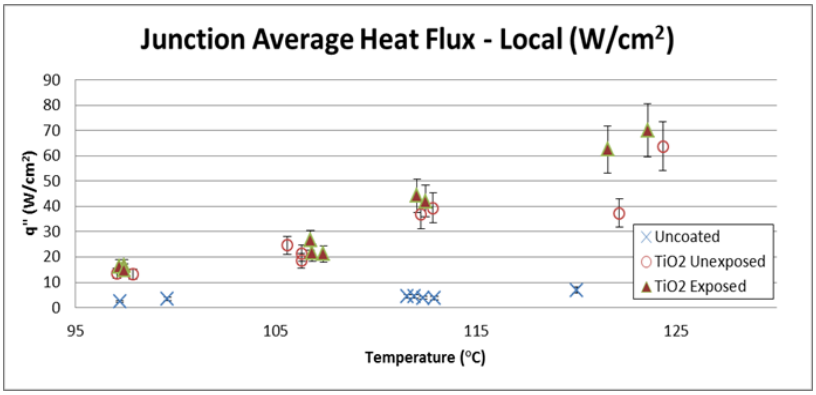

Fig. 4.100 Local time-averaged heat flux values (average for all the TFT junctions combined) plotted as a function of initial TFT temperature (comparison of bare wafer and wafer with nanocoating: unexposed and exposed to UV illumination).

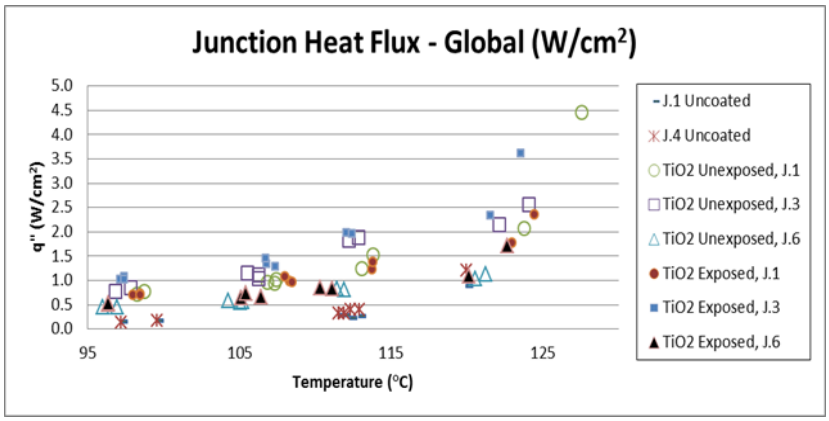

Fig. 4.11 Global time-averaged heat flux values for individual TFT junctions plotted as a function of initial TFT temperature (comparison of bare wafer and wafer with nanocoating: unexposed and exposed to UV illumination).

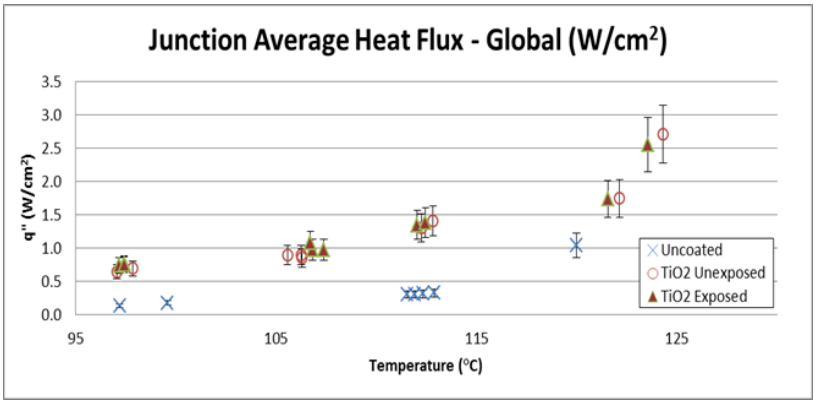

Fig. 4.12 Global time-averaged heat flux values (average for all the TFT junctions combined) plotted as a function of initial TFT temperature (comparison of bare wafer and wafer with nanocoating: unexposed and exposed to UV illumination).

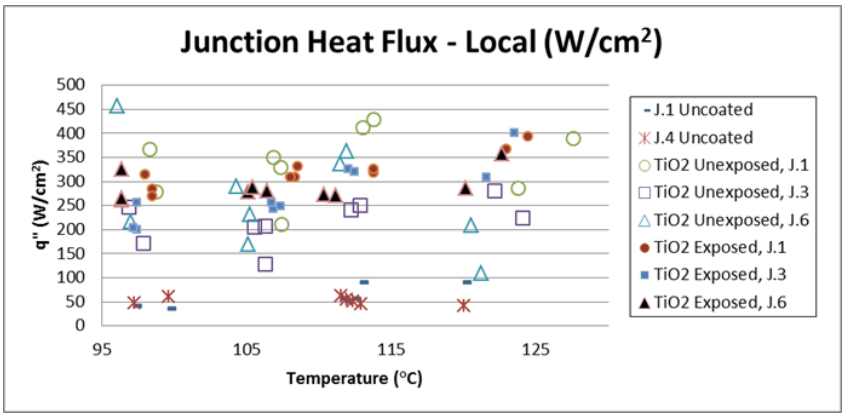

Fig. 4.13 Local maximum heat flux values for individual TFT junctions plotted as a function of initial TFT temperature (comparison of bare wafer and wafer with nanocoating: unexposed and exposed to UV illumination).

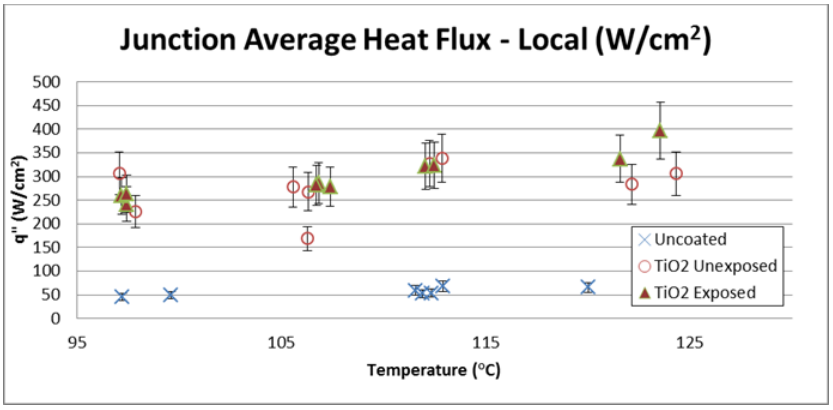

Fig. 4.14 Local maximum heat flux values (average for all the TFT junctions combined) plotted as a function of initial TFT temperature (comparison of bare wafer and wafer with nanocoating: unexposed and exposed to UV illumination).

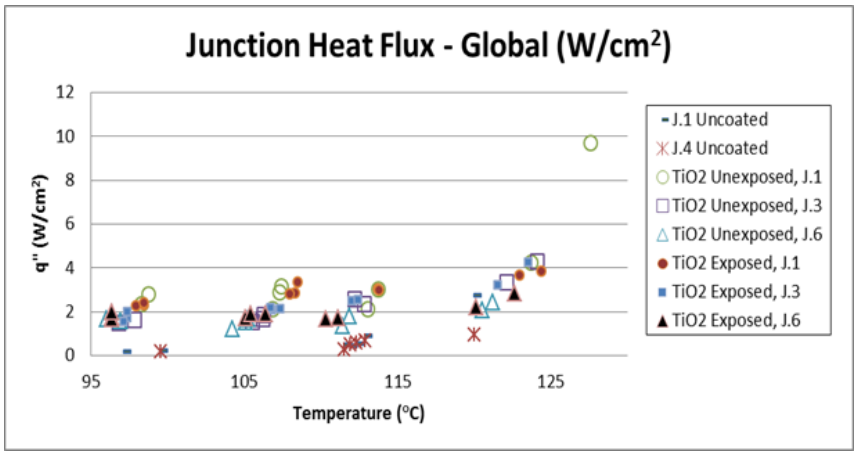

Fig. 4.15 Global maximum heat flux values for individual TFT junctions plotted as a function of initial TFT temperature (comparison of bare wafer and wafer with nanocoating: unexposed and exposed to UV illumination).

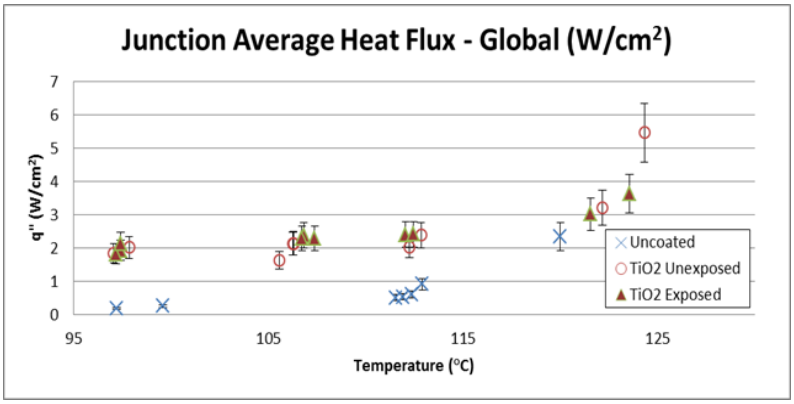

Fig. 4.16 Global maximum heat flux values (average for all the TFT junctions combined) plotted as a function of initial TFT temperature (comparison of bare wafer and wafer with nanocoating: unexposed and exposed to UV illumination).

Table 4.13 Change in local time-averaged heat flux values (average for all TFT junctions) at similar initial TFT temperature for bare wafer and wafer with nanocoatings (unexposed and exposed to UV illumination)

Average Heat Flux- Local (W/cm^2)				
Temp. (°C)	Uncoated	Temp. (°C)	Unexposed	% Increase
97.2	2.3	97.1	13.5	481.14%
112.4	3.9	112.2	36.8	842.75%
112.9	3.8	112.8	39.4	939.58%
120.0	7.0	122.2	37.4	437.33%
			Average	675.20%
			Std. Dev.	253.12%
Increase Between Uncoated and TiO2 Unexposed				

Average Heat Flux- Local (W/cm^2)				
Temp. (°C)	Uncoated	Temp. (°C)	Exposed	% Increase
97.2	2.3	97.2	16.4	603.29%
112.4	3.9	112.1	44.2	1032.04%
112.9	3.8	112.5	42.1	1010.63%
120.0	7.0	121.6	62.5	797.94%
			Average	860.97%
			Std. Dev.	201.69%
Increase Between Uncoated and TiO2 Exposed				

Table 4.14 Change in local time-averaged heat flux values (average for all TFT junctions) at similar initial TFT temperature for wafer with nanocoatings (unexposed and exposed to UV illumination)

Average Heat Flux- Local (W/cm^2)				
Temp. (°C)	Unexposed	Temp. (°C)	Exposed	% Increase
97.1	13.5	97.2	16.4	21.02%
97.9	13.3	97.4	16.6	25.27%
106.3	18.5	106.7	26.6	43.64%
106.3	21.5	106.8	21.7	1.15%
112.2	36.8	112.5	42.1	14.25%
112.8	39.4	112.1	44.2	12.28%
122.2	37.4	121.6	62.5	67.11%
			Average	26.39%
			Std. Dev.	22.24%
Increase Between TiO2 Unexposed and Exposed				

Table 4.125 Change in global time-averaged heat flux values (average for all TFT junctions) at similar initial TFT temperature for bare wafer and wafer with nanocoatings (unexposed and exposed to UV illumination)

Average Heat Flux- Global (W/cm^2)				
Temp. (°C)	Uncoated	Temp. (°C)	Unexposed	% Increase
97.2	0.1	97.1	0.6	373.45%
112.4	0.3	112.2	1.3	313.91%
112.9	0.3	112.8	1.4	329.66%
120.0	1.0	122.2	1.7	67.33%
			Average	271.09%
			Std. Dev.	138.16%
Increase Between Uncoated and TiO2 Unexposed				

Average Heat Flux- Global (W/cm^2)				
Temp. (°C)	Uncoated	Temp. (°C)	Exposed	% Increase
97.2	0.1	97.2	0.7	439.69%
112.4	0.3	112.1	1.3	328.42%
112.9	0.3	112.5	1.4	322.68%
120.0	1.0	121.6	1.7	66.20%
			Average	289.25%
			Std. Dev.	158.15%
Increase Between Uncoated and TiO2 Exposed				

Table 4.16 Change in global time-averaged heat flux values (average for all TFT junctions) at similar initial TFT temperature for wafer with nanocoatings (unexposed and exposed to UV illumination)

Average Heat Flux- Global (W/cm^2)				
Temp. (°C)	Unexposed	Temp. (°C)	Exposed	% Increase
97.1	0.6	97.2	0.7	13.99%
97.9	0.7	97.4	0.8	10.61%
106.3	0.9	106.7	1.1	21.11%
106.3	0.9	106.8	1.0	15.20%
112.2	1.3	112.5	1.4	6.30%
112.8	1.4	112.1	1.3	-4.21%
122.2	1.7	121.6	1.7	-0.67%
			Average	8.90%
			Std. Dev.	9.02%
Increase Between TiO2 Unexposed and Exposed				

Table 4.137 Change in local maximum heat flux values (average for all TFT junctions) at similar initial TFT temperature for bare wafer and wafer with nanocoatings (unexposed and exposed to UV illumination)

Max Average Heat Flux- Local (W/cm^2)				
Temp. (°C)	Uncoated	Temp. (°C)	Unexposed	% Increase
97.2	44.9	97.1	306.7	583.69%
112.4	53.2	112.2	326.5	513.21%
112.9	68.2	112.8	339.1	397.16%
120.0	65.5	122.2	283.5	332.51%
			Average	456.64%
			Std. Dev.	112.97%
Increase Between Uncoated and TiO_2 Unexposed				

Max Average Heat Flux- Local (W/cm^2)				
Temp. (°C)	Uncoated	Temp. (°C)	Exposed	% Increase
97.2	44.9	97.2	258.9	477.06%
112.4	53.2	112.1	321.8	504.40%
112.9	68.2	112.5	323.4	374.14%
120.0	65.5	121.6	337.6	415.13%
			Average	442.68%
			Std. Dev.	59.01%
Increase Between Uncoated and TiO_2 Exposed				

Table 4.148 Change in local maximum heat flux values (average for all TFT junctions) at similar initial TFT temperature for wafer with nanocoatings (unexposed and exposed to UV illumination)

Max Average Heat Flux- Local (W/cm^2)				
Temp. (°C)	Unexposed	Temp. (°C)	Exposed	% Increase
97.1	306.7	97.2	258.9	-15.60%
97.9	225.2	97.4	263.2	16.85%
106.3	169.3	106.7	282.0	66.59%
106.3	268.0	106.8	286.5	6.90%
112.2	326.5	112.5	323.4	-0.96%
112.8	339.1	112.1	321.8	-5.09%
122.2	283.5	121.6	337.6	19.10%
			Average	12.54%
			Std. Dev.	26.77%
Increase Between TiO_2 Unexposed and Exposed				

Table 4.159 Change in global maximum heat flux values (average for all TFT junctions) at similar initial TFT temperature for bare wafer and wafer with nanocoatings (unexposed and exposed to UV illumination)

Max Average Heat Flux-Global (W/cm^2)				
Temp. (°C)	Uncoated	Temp. (°C)	Unexposed	% Increase
97.2	0.2	97.1	1.8	873.41%
112.4	0.6	112.2	2.0	231.54%
112.9	0.9	112.8	2.4	160.58%
120.0	2.3	122.2	3.2	37.34%
			Average	325.71%
			Std. Dev.	373.84%
Increase Between Uncoated and TiO_2 Unexposed				

Max Average Heat Flux-Global (W/cm^2)				
Temp. (°C)	Uncoated	Temp. (°C)	Exposed	% Increase
97.2	0.2	97.2	1.8	867.94%
112.4	0.6	112.1	2.4	292.89%
112.9	0.9	112.5	2.4	163.52%
120.0	2.3	121.6	3.0	29.27%
			Average	338.41%
			Std. Dev.	369.07%
Increase Between Uncoated and TiO_2 Exposed				

Table 4.20 Change in global maximum heat flux values (average for all TFT junctions) at similar initial TFT temperature for wafer with nanocoatings (unexposed and exposed to UV illumination)

Max Average Heat Flux-Global (W/cm^2)				
Temp. (°C)	Unexposed	Temp. (°C)	Exposed	% Increase
97.1	1.8	97.2	1.8	-0.56%
97.9	2.0	97.4	2.1	5.46%
106.3	2.1	106.7	2.3	7.57%
106.3	2.1	106.8	2.4	10.70%
112.2	2.0	112.5	2.4	19.28%
112.8	2.4	112.1	2.4	0.48%
122.2	3.2	121.6	3.0	-5.88%
			Average	5.29%
			Std. Dev.	8.29%
Increase Between TiO_2 Unexposed and Exposed				

Maximum Value of Heat Flux (Local and Global)

In addition to time-averaged heat flux, maximum heat flux values were also identified from the data sets (both for local and global heat flux values). The results for local values of maximum heat flux are plotted in Figures 4.13 and 4.14 as well as listed in Tables 4.17 and 4.18. The results for global values of maximum heat flux are plotted in Figures 4.15 and 4.16 as well as listed in Table 4.19 and 4.20.

The maximum value of local heat flux also increases substantially (~450%) between uncoated and coated wafers for the local values. Similar trends in experimental data for maximum heat flux values were found in the experiments performed at Texas A&M. The same reasoning holds true for these wafers; maximum heat flux is a weak function of the surface temperature and is more sensitive to the surface conditions. However, the maximum values of local heat flux increases by approximately ~100 - 300 W/cm^2 for the same heater temperature for the exposed wafer with nanocoating (Figure 4.14).

Local heat flux is found to increase by ~450% (Table 4.16) while global values increase by approximately 325% (Table 4.18) when comparing uncoated and coated wafers. Again, this large increase may not solely be caused by the reduction in contact angle, since surface roughness may play a dominant role. Local and global heat flux values for the coated (unexposed to exposed) wafers were found to be weakly sensitive to the effects of exposure to UV light. Average values for heat flux showed an increased by 12% (locally) with standard deviation of 26.77% and no significant increase in global heat flux values was observed.

Droplet Evaporation Results (AFRL)

Droplet evaporation times were also significantly reduced for coated wafers (compared to that of uncoated wafers). A 3-dimensional plot was created to capture these results. The initial steady state temperature of heater surface, volume of impinging droplet, and evaporation rate (mg/sec) were explored in these plots. This plot is shown in Figure 4.17. The figure shows that for the same temperature and volume, for the coated wafers both exposed and unexposed conditions yield a higher evaporation rate compared to that of the uncoated wafers. This plot takes initial volume of droplet into account, but can be somewhat difficult to read. Since droplet volumes varied very little, Figure 4.18 shows a simplified version of Figure 4.17. The figures show that the evaporation time decreases by 25-40% for experiments with coated wafers when compared to that of bare wafers.

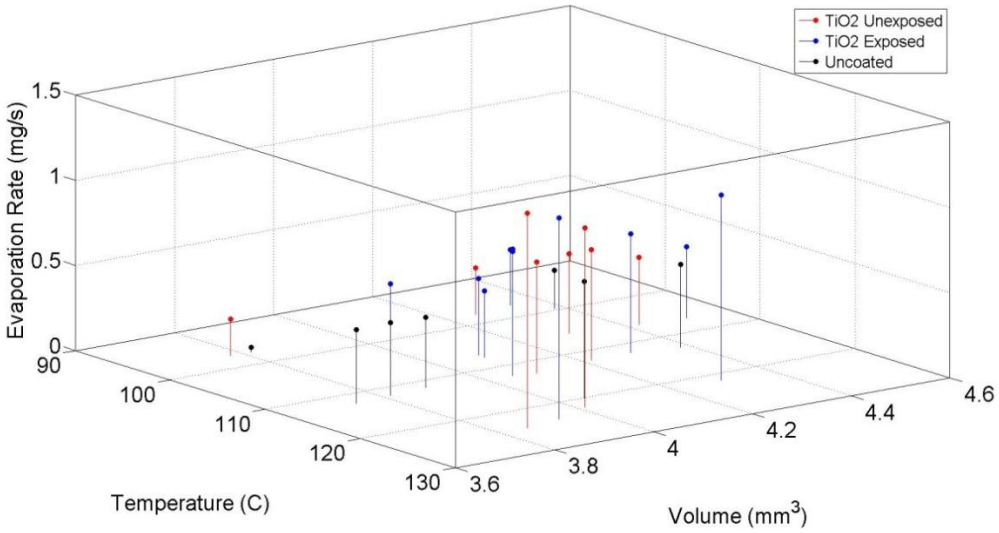

Fig. 4.17 Evaporation rate of individual droplets as a function of heater temperature and droplet volume (for experiments performed at AFRL).

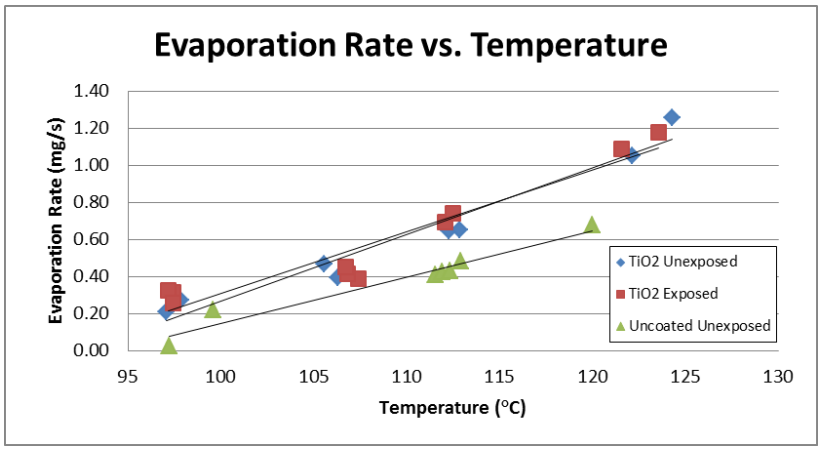

Fig. 4.18 Evaporation rate of individual droplets as a function of heater temperature (for experiments performed at AFRL).

CHAPTER V

VIDEO ANALYSIS

A unique aspect of this investigation is the use of high speed digital image acquisition that was integrated and synchronized with high-speed digital data acquisition from the temperature nano-sensors. The combination of these two aspects simultaneously enables quantitative data analyses along with qualitative analyses of flow regimes of the boiling/evaporating droplet (i.e., hydrodynamic phenomena coupled non-linearly with the thermal response of the surface temperature and heat flux). The transient temperature data as well as high-speed video files were combined and synchronized using a multi-step process (highlighted in Table 5.1). Synchronized videos of experimental data were generated for the experiments conducted at AFRL (since the image acquisition rate for experiments conducted at A&M was very low).

Table 5.1: Procedure used to synchronize temperature, time, and image data

Step	Procedure	Program
1	Raw video file is converted to .avi file	Phantom
2	.avi file is broken into an image series	Midas Player
3	Images are given a filename corresponding to elapsed time	Matlab
4	Temperature, time, image, and heat flux data are synchronized and visually inspected to ensure synchronization	Matlab
5	Correct synchronized data is saved as an image sequence	Matlab
6	Images sequence saved as a .avi file	Matlab

Of particular difficulty in aligning these images was the inconsistent frequency of data acquisition. The DAQ used at AFRL recorded at an inconsistent rate of either 100 Hz or 91 Hz (i.e., recording one sample every 10 or 11 ms). In order to correctly synchronize images with this inconsistent data, the filenames of the image sequences were saved with a number corresponding to elapsed time. A Matlab program was then written to search for the closest image number, given an elapsed time from the DAQ data. This process can be seen in Figure 5.1 and worked very effectively. The matching scheme between the synchronized temperature, time, and video images are shown in Figure 5.1.

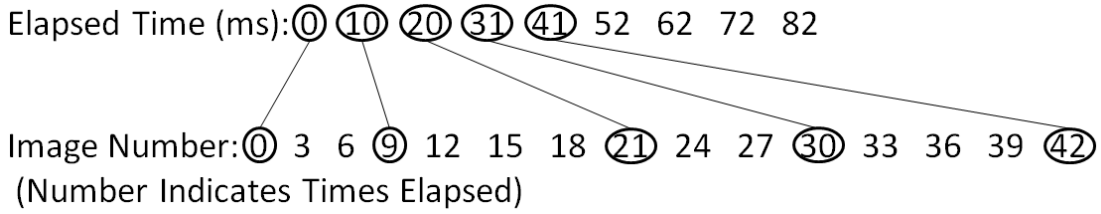

Fig. 5.1 Summary of time and image synchronization process

With the images synchronized with the appropriate temporal value of the temperature fluctuation data, a Matlab program was created to create a figure of not only temperature, elapsed time, and an image, but also local and global heat flux data. Each graph consisted of a green tracking bug (marker) that tracks data synchronized with the elapsed time. Data for each TFT junction is also color coordinated so one can easily correlate TFT junction information from graph to graph and easily compare response between TFT junctions at each time step. In creating these videos it was noted that temperature and time data for fully developed nucleate boiling can be very difficult to decipher since the plots were found to overlap. To provide better visualization of the

temperature information an additional movie was created in which individual graphs for each TFT junction was plotted. These are called “split videos” and are saved accordingly.

Discussions in the remainder of this chapter explore the typical regimes for boiling and evaporation of the impinged droplet that was observed in the synchronized videos. The boiling/evaporation regimes were found to vary for each droplet as a function of the experimental parameters (e.g., initial steady state surface temperature for the heater, bare/ coated wafers, unexposed/exposed to UV illumination, etc.). Figure 5.2 shows a typical frame from the synchronized videos generated in this study. Figure 5.2 is a typical frame showing the droplet (and TFT array) just prior to impact with the heater surface. All movies commenced immediately before droplet impingement on the surface, as indicated in Figure 5.2. At the moment before impact, elapsed time is zero. Temperature information is plotted for half second before impact so that the initial temperature of each junction is shown in the synchronized video. Additionally, since local (maximum) heat fluxes are considerably larger, the maximum values are individually listed and color coordinated with their individual junction. This allows a better perception of the smaller local scale transient phenomena. Within these videos, it is possible to clearly identify several stages of the droplet evaporation process starting with (1) heat transfer to semi-infinite body; transitioning to (2) boiling inside the droplets; and then to (3) film evaporation (where bubbles within the bubbles cease to exist).

Video files are attached for all experiments where video was recorded. To view these videos, a power point file is included and can be used to navigate between video files.

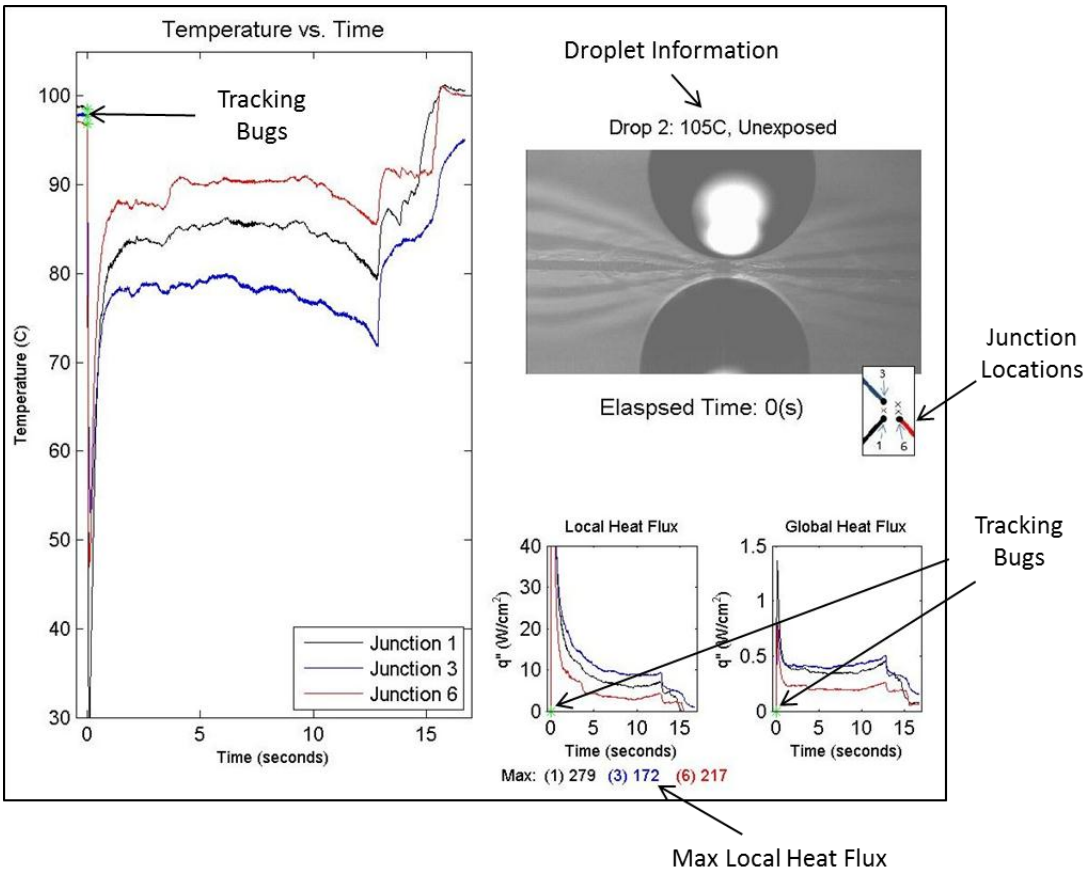

Fig. 5.2 Representative frame for synchronized movies of droplet impingement

For videos corresponding to initial surface temperature of 105°C, onset of nucleate boiling can be identified by the formation of bubbles (which is accompanied by large fluctuation is the surface temperature). Additionally, these videos verify what many studies have concluded before; droplet diameter remains constant for the majority of droplet lifetime with the contact angle decreasing continually, an effect known as "pinning" [33]. A gradual increase in heat flux during this "pinning" time is also apparent in the synchronized videos. This has not been observed in previous literature reports. After the droplet contact angle reaches 20-40° the diameter of the droplet begins to shrink at a

fast rate [6, 33]. This phenomena occurs immediately after detachment of the last bubble, as shown in Figure 5.3, and is noted by a spike in temperature (in the vicinity of the green tracking bugs shown in the figure) and this is accompanied by a sudden decrease in both global and local heat flux values. After this event, film evaporation regime dominates and the droplet evaporates completely without the nucleation of any vapor bubble.

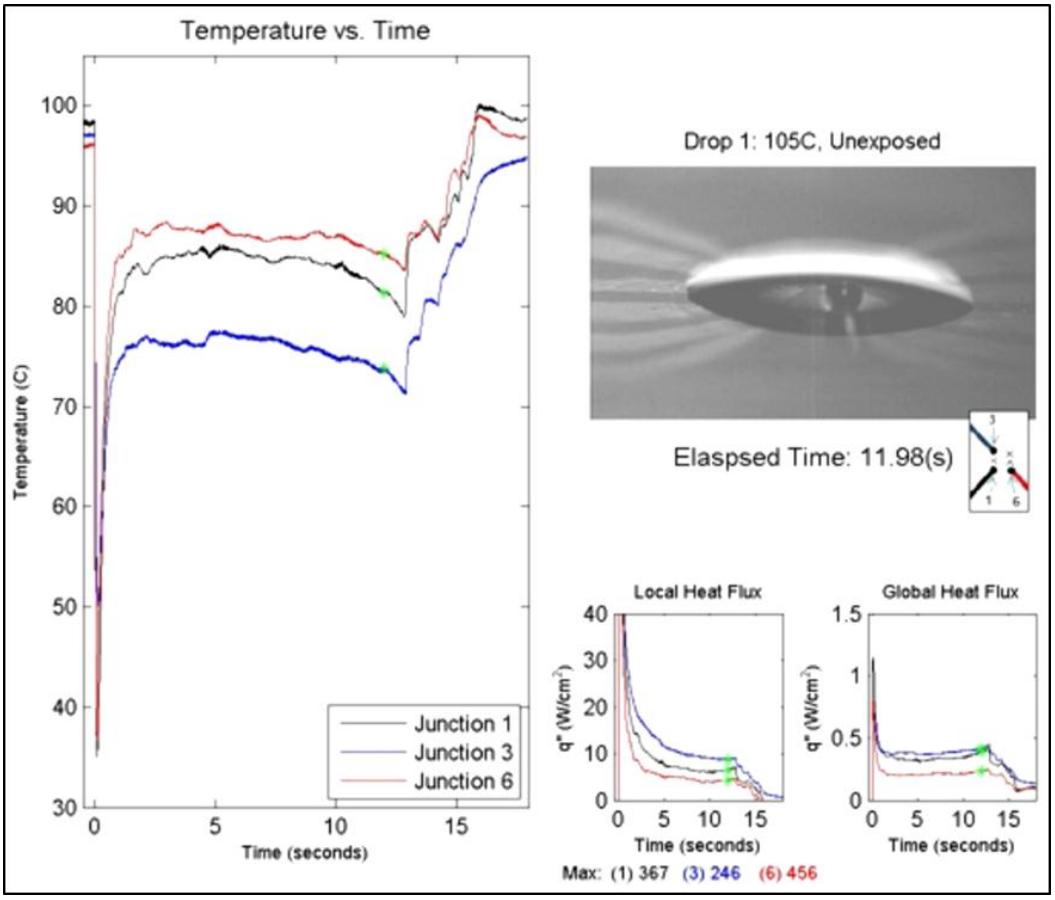

Fig. 5.3 Typical synchronized video frame at heater temperature (initial steady state value) of 105 °C.

For videos corresponding to initial surface temperature of 115°C, nucleate boiling is observed to be more prevalent. Nucleate boiling commences earlier and leads to reduction in temperature as noted by the blue colored plot (for J.3, temperature plot). Additionally, discrete, isolated bubbles are formed and released from various nucleation sites. At this temperature the pinning effect for the droplet is also apparent.

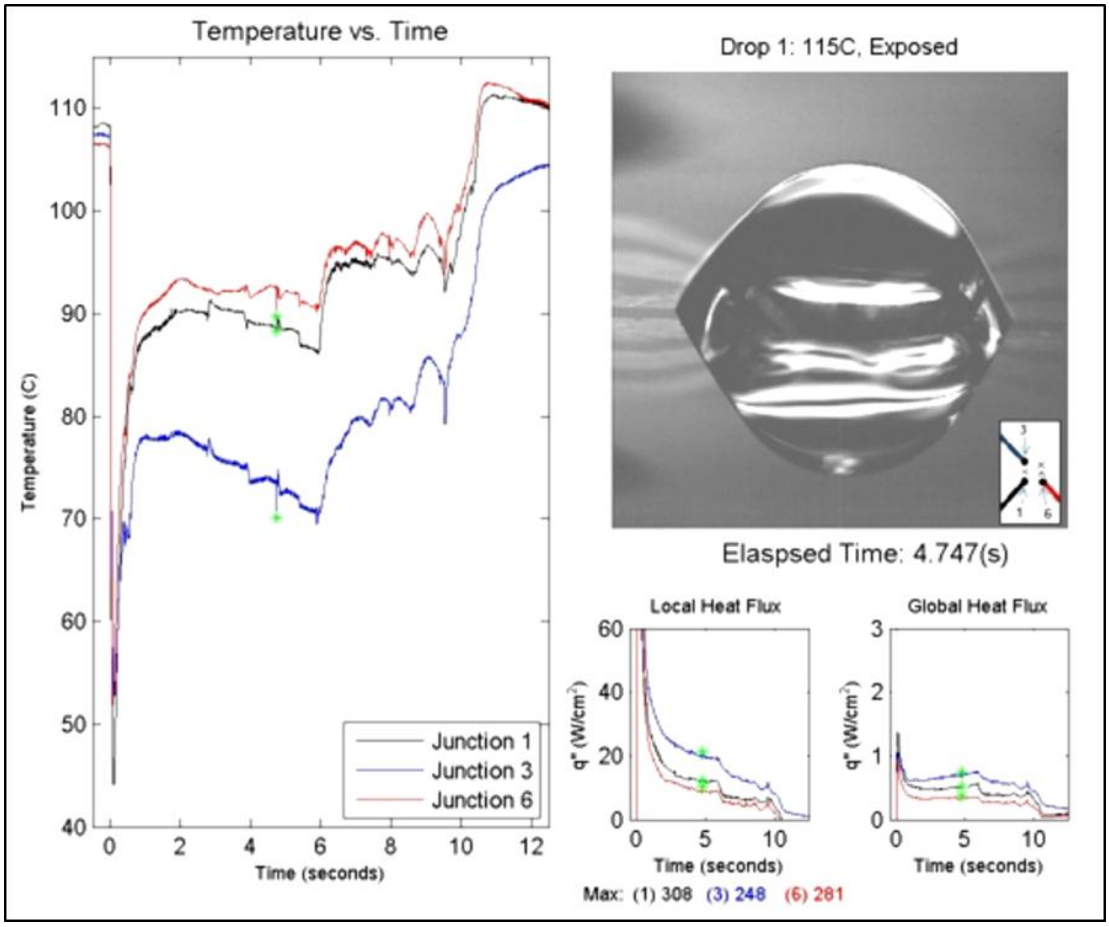

Fig. 5.4 Typical synchronized video frame at heater temperature (initial steady state value) of 115 °C.

For videos corresponding to initial surface temperature of 121°C, fully developed nucleate boiling region is observed and nucleate boiling is found to be more prevalent. Large fluctuations in the surface temperature (shown by the location of the tracker bug or "marker") are accompanied with "explosive boiling" phenomena. This is observed to occur within the droplet – where the vapor bubbles are generated at a rapid rate and depart with a violent behavior causing the droplet to break up and spit out smaller droplets around the droplet that initially impinged on the surface. These explosions cause a sudden increase in local and global heat transfer values and are associated with a decrease in temperature. Additionally, it can be noted (at the location of the tracker bugs) that during an explosion, temperature does not drop by an equal amount for all junctions. The change in temperature for the red junction (J.6) is approximately 15°C while for the blue junction (J.3), the temperature drop is only about 5°C. This could be indicative of a bubble forming near the front of the droplet causing a high heat flux for J.1 and J.6 and a lower flux for J.3. Additionally, the distance between these two junctions is approximately 670 nm and is an indicator of the large temporal and spatial fluctuations in temperature occurring within a small water droplet.

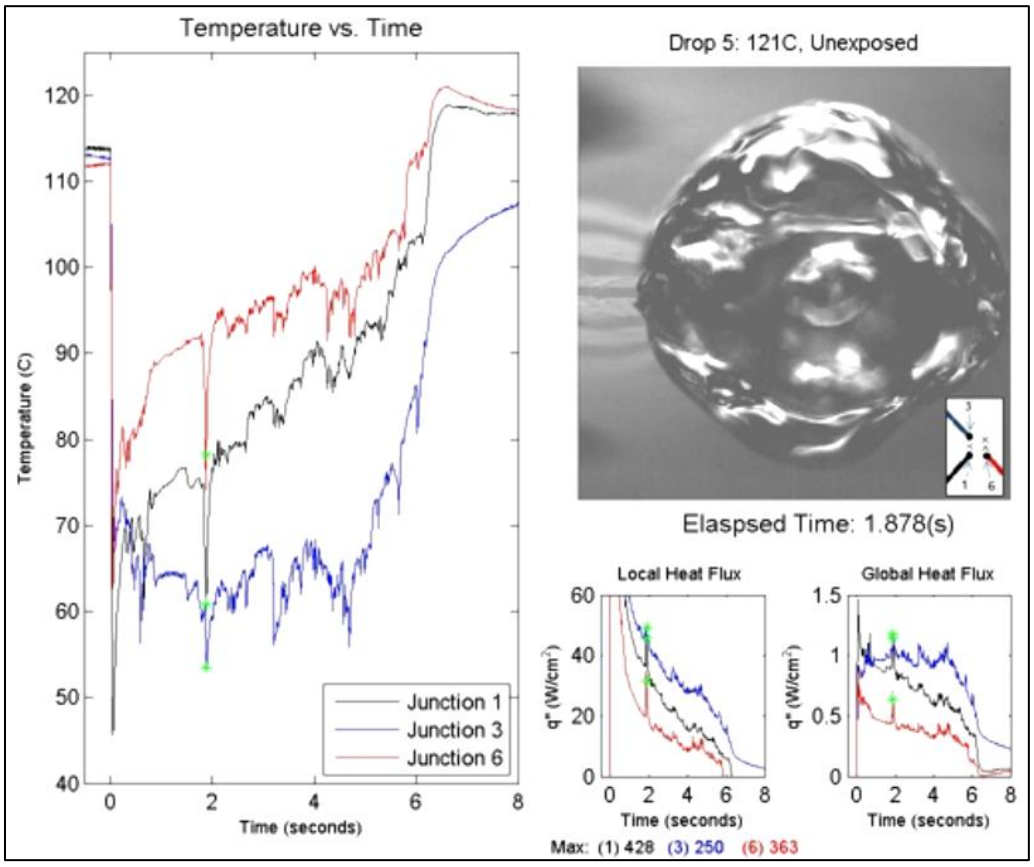

Fig. 5.5 Typical synchronized video frame at heater temperature (initial steady state value) of 121 °C

For videos corresponding to initial surface temperature of 131°C the fully developed nucleate boiling regime was observed to occur. This was accompanied by violent spluttering, ejection of individual bubbles, lateral merger with adjacent bubbles, and the excision of the water droplet. Very large fluctuations in temperature were observed in the plots (J.1), indicating large temporal and spatial variations in temperature existing over time scales less than 10 ms and length scales of ~ 600 microns.

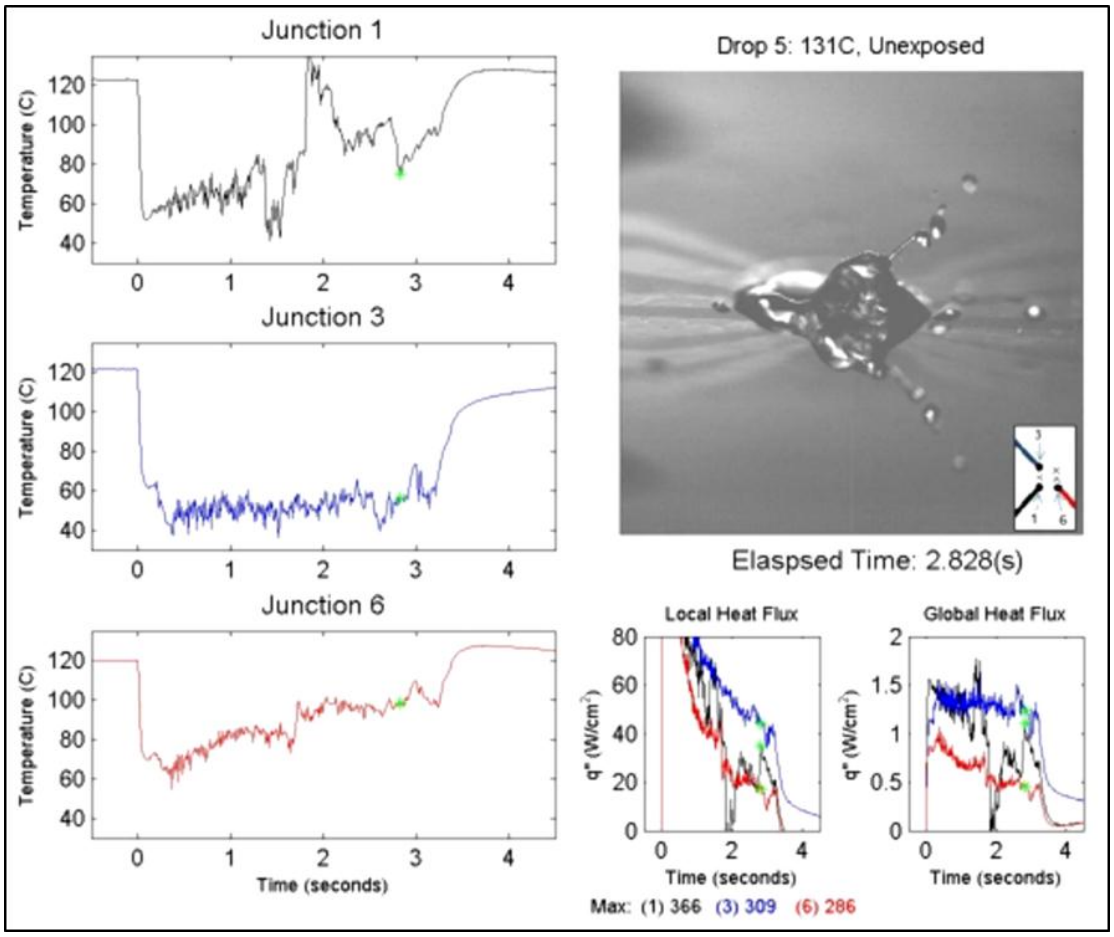

Fig. 5.6 Typical synchronized video frame at heater temperature (initial steady state value) of 131 °C

Synchronized videos generated for the uncoated wafer experiments show similar behavior to that of the coated wafers (Figure 5.7). However, a few distinct differences were observed for the uncoated wafers. First, the initial temperature drop is significantly smaller than that of coated wafers (~10°C verses ~60°C), and consequently significantly enhanced heat flux values were recorded for wafers with nanocoatings (as discussed in Chapter IV). The two TFT junctions that were functional (J.1 and J.4) displayed larger frequencies and smaller magnitude of temperature fluctuations for the same boiling/ evaporation regimes (as shown in Figure 5.7). In addition, the droplet oscillations were more "graceful" with more orderly bubble generation and departure cycles (and lesser amounts of droplet splitting occurring at elevated surface temperatures).

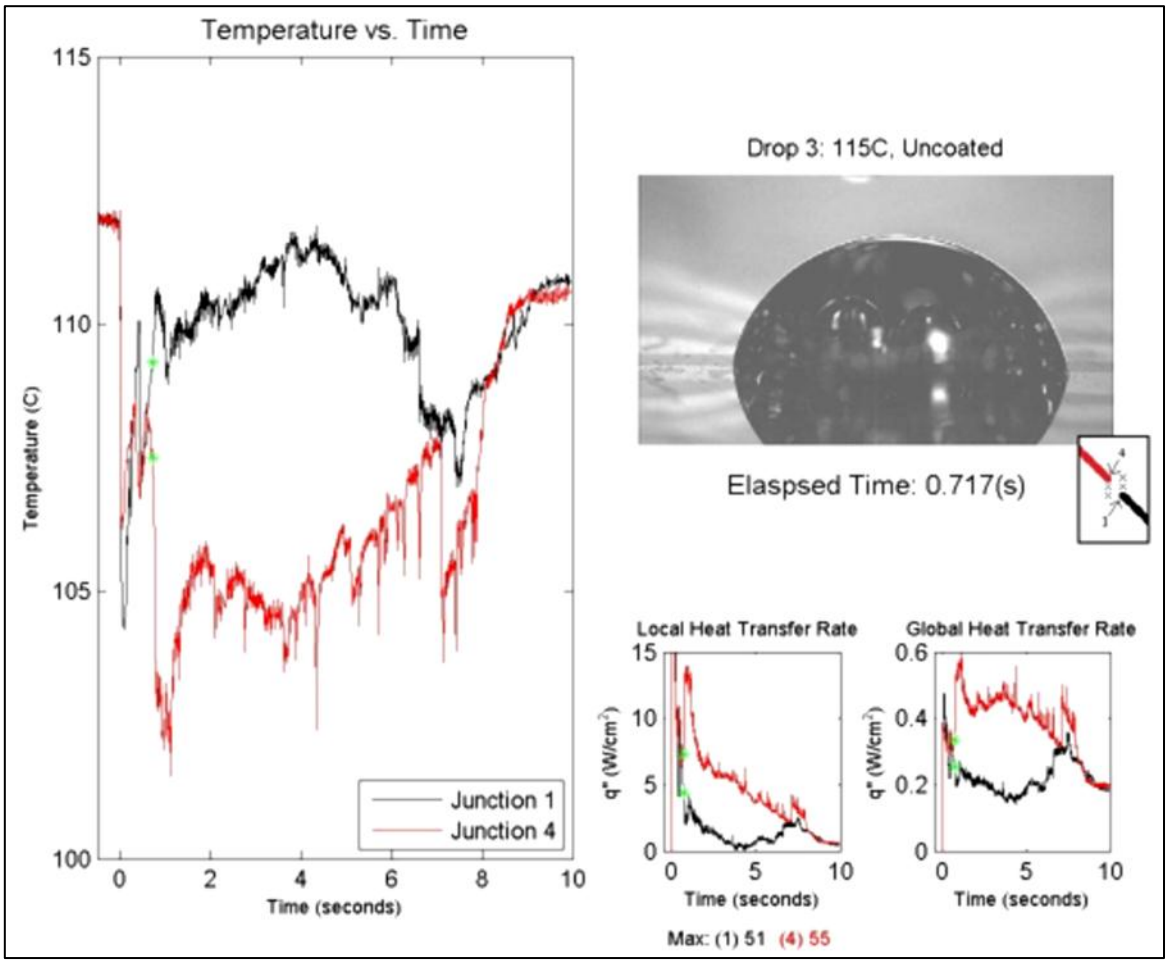

Fig. 5.7 Typical frame from synchronized video for droplet impingement at heater temperature (initial steady state value) of 115 °C for uncoated wafer.

CHAPTER VI

SUMMARY AND FUTURE DIRECTION

In this study water droplet impingement on a silicon wafer coated with TiO_2 and exposed to UV light was explored. These results were compared with data from the control experiments (bare surface - both with and without UV illumination). Through the use of novel temperature nano-sensors called "Thin Film Thermocouples" (TFT's), high-frequency data acquisition of the temperature at the liquid-solid interface was performed. High-speed video was also recorded of each impinging droplet. These images were synchronized with the high speed temperature data acquired. Both local and global heat flux values were calculated from the experimental data. The transient profiles for temperature, local and global heat flux, and images of the boiling/evaporating droplet were combined into a single synchronized video file for each droplet. These video images enabled the quantitative and qualitative comparison of the thermal and hydrodynamic features during phase-change and as a function of the experimental parameters (presence or absence of coating, exposure to UV illumination, effect of contact angle, surface roughness, wall superheat, droplet impingement velocity, droplet size, etc.). The control experiments conclusively demonstrated that light intensity for the UV illumination did not affect the heat flux values during droplet impingement on a bare wafer. This research complements the observations reported by Qiu and Liu [19]. The authors reported that different UV light intensities had no effect on the contact angle of a TiO_2 coated surface.

A significant improvement in heat flux was obtained for both local and global heat flux values (time averaged and maximum value) for a nanocoating of TiO_2. However, the surface roughness of the TiO_2 nanocoatings (accompanied by the nano-fin effect and enhancement of nucleation site density) are observed to be the dominant factors responsible for heat flux enhancements observed in the experiments performed in this study. The following conclusions are summarized for experimental results obtained from the wafers with TiO_2 nanocoatings (unexposed and exposed experiments).

- For time-averaged heat flux:
    - When comparing an uncoated wafer to coated wafer, unexposed or exposed to UV illumination at 405 nm wavelength, contact angle is reduced by ~10° and ~20°, respectively and with significantly increased surface roughness:
        - *Local* values increased by ~ 650-850%
        - *Global* values increased by ~275%
    - A titanium dioxide coated wafer exposed to UV light (405 nm) decreases contact angle by no greater than 10° and shows a 25% increase in heat flux locally, while no perceptible increase is observed globally when compared to an unexposed TiO_2 coated wafer.
- For maximum heat flux:
    - When comparing an uncoated wafer to coated wafer, unexposed or exposed, contact angle is reduced by ~10° and ~20°, respectively, and with significantly increased surface roughness:

- *Local* values increased by ~ 450%
- *Global* values increased by ~325%

- A titanium dioxide coated wafer exposed to UV light (405 nm) has no perceptible increase in maximum heat flux values (local or global values) when compared to an unexposed TiO_2 coated wafer.

In addition to the heat flux data, the surface temperature transients recorded by the TFT array show large temperature gradients. Temperature fluctuations of ~15°C occur over a time period of 10 ms and temperature drop of ~15°C are observed to occur over distances spanning only 670 microns. This translates to spatial gradients of ~2.2×10^4 °C/m and ramp rates of ~1500 °C/s. Thus, such high magnitudes for temperature fluctuations and gradients are classical examples of "inverse problems", where the heat fluxes along the surface are of comparable magnitude (or larger) than the heat fluxes perpendicular to the surface.

Future work with similar droplet impingement studies should ensure that both uncoated and coated wafers have similar values of surfaces roughness (e.g., using Chemical Mechanical Polishing or "CMP"). Additionally, the effect of a thicker coating of TiO_2 (~250 nm) could be explored. An UV illumination source with a shorter wavelength (275-315 nm range) can be used in addition to exposing the wafers to longer duration of illumination (~ two hours or more). With the combination of these two factors, creating a superhydrophilic surface could be achieved, as reported in the literature (but was not observed in this study).

In addition to new studies that are recommended, further data analysis from the existing video images of the individual droplets can be performed. A myriad of information is available in these videos. The image analyses of these videos can focus on determining different boiling regimes. Inverse problem techniques can be used to analyze the temporal and special variations of temperature between each TFT junction to obtain better estimates for heat flux in different directions on the heater surface. Additionally, new synchronized videos can be developed containing the entire image series which is synchronized with temperature and heat flux data. Including the entire image series will allow a better appreciation of the flow features for the different boiling/ evaporation regimes. Additional insights can be gained from such synchronized videos, especially for the chaotic boiling phenomena (along with explosive boiling) that were observed to occur at heater temperature (initial steady state values) of 121°C and 131°C.

REFERENCES

[1] Wangcun, J., "Study of Spray Cooling by Advanced Optical Diagnostics." Ph.D. Dissertation, Dept. of Mechanical Engineering, Hong Kong University of Science and Technology, 2001.

[2] Mudawar, I., "Assessment of High-Heat-Flux Thermal management Schemes," *IEEE Transactions on Components and Packaging Technologies*, Vol. 24, 2001, pp. 122-141.

[3] Yarin, L.P., Masyak, A., Hetsroni, G., "*Fluid Flow Heat Transfer and Boiling in Micro-Channels*," Spring Publishing, Berlin, Germany, 208.

[4] Chandra, S., diMarzo, M., Qiao, Y. M., and Tartarini, P., "Effect of Liquid-Solid Contact Angle on Droplet Evaporation," *Fire Safety Journal,* Vol. 27, 1996, pp. 141-158.

[5] Park, C., Vallury, A., "Advanced Hybrid Cooling Loop Technology for High Performance Thermal Management," *AIAA, 4th International Energy Conversion Engineering Conference,* San Diego, California. June 26-29, 2006,

[6] Crafton, E. F. and Black, W.Z., "Heat Transfer and Evaporation Rates of Small Liquid Droplets on Heated Horizontal Surfaces," *Int. J. Heat Mass Transfer,* Vol. 47, 2004, pp. 1187-1200.

[7] Bernardin, J.D., Stebbins, C.J., and Mudawar, I., "Mapping of Impact and Heat Transfer Regimes of Drops Impinging on a Polished Surface," *Int. J. Heat Mass Transfer,* Vol. 40, 1997, pp. 247-267.

[8] Mehdizadeh, N. Z. and Chandra, S., "Boiling During High Velocity Impact of Water Droplets on a Hot Stainless Steel Surface," *Proceedings of the Royal Society*, Mathematical, Physical, and Engineering Sciences, Toronto, Ontario, 2012, pp. 3115-3131.

[9] Pederson, C. O., "An Experimental Study of the Dynamic Behavior and Heat Transfer Characteristics of Water Droplets Impinging Upon a Heated Surface," *Int. J. Heat Mass Transfer,* Vol. 13, 1970, pp. 339-381.

[10] Nikolopoulous, N. and Theodorakakos, A., Bergeles, G., "A Numerical Investigation of the Evaporation Process of a Liquid Dropt Impinging onto a Hot Substrate," *Int. J. Heat Mass Transfer,* Vol. 50, 2007, pp. 303-319.

[11] Wachterst, L.H.J. and Westerling, N.A.J., "The Heat Transfer From a Hot Wall to Impinging Water Drops in the Spheroidal State," *Chemical Engineering Science,* Vol. 21, 1966, pp. 1047-1056.

[12] Healy, W. M., Halvorson. P. J., Hartley, J. G., and Abdel-Khalik, S.T., "A Critical Heat Flux Correlation for Droplet Impact Cooling at Low Weber Numbers and Various Ambient Pressures," *Int. J. Heat Mass Transfer*, Vol. 41, 1997, pp. 975-978.

[13] Sawyer, M.L., Jeter, S.M., and Abdel-Khalik, S.I., "A Critical Heat Flux Correlation for Droplet Impact Cooling," *Int. J. Heat Mass Transfer*, Vol. 40, 1997, pp. 2153-2131.

[14] Avedisian, C. T. and Koplik, J., "Leidenfrost Boiling of Methanol Droplets on Hot Porous/Ceramic Surfaces," *Int. J. Heat Mass Transfer*, Vol. 30, 1987, pp. 379-393.

[15] Engel, O. G., "Waterdrop Collision with Solid Surfaces," *J. Res. National. Bur. Standards*, Vol. 54, 1955.

[16] Ganic, E. N. and Rohsenow, W. M., "Dispersed Flow Heat Transfer," *Int. J. Heat Mass Transfer,* Vol. 20, 1977, pp. 855-866.

[17] Bernardin, J. D., Stebbins, C. J., and Mudawar, I., "Effects of Surface Roughness on Water Droplet Impact History and Heat Transfer Regimes," *Int. J. Heat Mass Transfer,* Vol. 40, 1997, pp. 73-88.

[18] Bernardin, J. D., Mudawar, I., Walsh, C. B., and Mranses, E. I., "Contact Angle Temperature Dependence for Water Droplets on Practical Aluminum Surfaces," *Int. J. Heat Mass Transfer,* Vol. 40, 1997, pp. 1017-1033.

[19] Qiu, Y. and Liu, Z., "Nucleate Boiling on the Superhydrophilic Surface with a Small Water Impingement Jet," *Int. J. Heat Mass Transfer*, Vol. 51, 2008, pp. 1683-1690.

[20] Takata, Y., Hidaka, S., Cao, J.M., Nakamura, T., Yamamoto, H., et.al., "Effect of Surface Wettability on Boiling and Evaporation," *Energy*, Vol. 30, 2005, pp. 209-220.

[21] Golovko, D. S., Butt, H. J., and Bonaccurso, E., "Transition in the Evaporation Kinetics of Water Microdrops on Hydrophilic Surfaces," *Langmuir*, Vol. 25, 2009, pp. 75-78.

[22] Chan, Y., Charbel, F., Xhang, Y., Zhang, Y., Ray, S. S., and Yarin A. L., "Hydrodynamics of Drop Impact and Spray Cooling Through Nanofiber Mats*," Journal of Undergraduate Research,* 2011, pp. 43-47.

[23] Bonacina, C., Del-Giudice, S., and Comini, G., "Dropwise Evaporation," *Journal of Heat Transfer*, Vol. 101, 1979, pp. 441-446.

[24] Grisson, W. M. and Wierum, F. A., "Liquid Spray Cooling of a Heated Surface," *Int. J. Heat Mass Transfer*, Vol. 24, 1981, pp. 261-271.

[25] Sadhal, S. S. and Plessert, M. S., "Effect of Solid Properties and Contact Angle in Dropwise Condensation and Evaporation," *Journal of Heat Transfer*, Vol. 101, 1979, pp. 48-54.

[26] Yang, W. J., "Mechanics of Droplet Evaporation on Heated Surfaces," *Letters in Heat and Mass Transfer,* Vol. 5, 1978, pp. 151-166.

[27] Tio, K. K. and Sadhal, S. S., "Dropwise Evaporation: Thermal Analysis of Multidrop Systems," *Int. J. Heat Mass Transfer*, Vol. 35, 1992, pp. 1987-2004.

[28] Hirt, C. W. and Nichols, B. D., "Volume of Fluid (VOF) Method for the Dynamics of Free Boundaries," *Journal of Computational Physics*, Vol. 39, 1981, pp. 201-225.

[29] Nichols, B. D., Hirt, C. W., and Hotchkiss, R.S., "SOLVA-VOF: A Solution Algorithm for Transient Fluid Flow with Multiple Free Boundaries," Technical Report LA-8355, Los Alamos National Laboratory, August 1980.

[30] Hirt, C. W. and Nichols, B. D., "Volume of Fluid (VOF) Method for the Dynamics of Free Boundaries," *Journal of Computational Physics*, Vol. 39, 1981, pp. 201-225.

[31] Sussman, M., Smereka, P., and Osher, S., "A Level Set Approach for Computing Solutions to Incompressible Two-Phase Flow," *Journal of Computational Physics,* Vol. 114, 1994, pp. 146-159.

[32] Sussman, M. and Smereka, P., "Axisymmetric Free Boundary Problems," *Journal of Fluid Mechanics*, Vol. 341, 1997, pp. 269-294.

[33] Sodtke, C., Ajaev, V.S., and Stephan, P., "Evaporation of Thin Liquid Droplets on Heated Surfaces," *Heat Mass Transfer*, Vol. 43, 2007, pp. 649-657.

[34] Stasiek, J., Stasiek, A., Jewartowski, M., and Collins, M.W., "Liquid Crystal Thermography and True-Color Digital Image Processing," *Optics and Laser Technology,* Vol. 38, 2006, pp. 243-256.

[35] Jeon, S. I., "Development of Mico/Nano-Scale Sensors for Investigation of Heat Transfer in Multi-Phase Flows," Ph.D. Dissertation, Dept. of Mechanical Engineering, Texas A&M University, 2011.

[36] Sinha, N., Ahn, H.S., Williams, R., and Banerjee, D., "Packaging of Surface Micromachined Thin Film Thermocouples (TFT): Comparison of the Resistance Arc Microwelding Technique with Wire Bonding," *Components and Packaging Technologies, IEEE Transactions*, Vol. 32, 2009, pp. 252-260.

[37] Chu, D., Bilir, D. T., Fabian, R., Pease, W., andGoodson, K.E., "Thin-film Nano Thermocouple Sensors for Application in Laser and Electron Beam Irradiation," *Proc. 12th Int. Conf. Solid State Sensors Actuators Microsyst.*, Boston, MA, 2003, pp. 1112–1115.

[38] Kreider, K. G. and Gillen, G., “High Temperature Materials for Thin-Film Thermocouples on Silicon Wafers,” *Thin Solid Films*, Vol. 376, 2000, pp. 32–37.

[39] Singh, N., Sathyamurthi, V., Petersen, W., Arendt, J., and Banerjee D., "Flow Boiling Enhancement on a Horizontal Heater using Carbon Nanotube Coatings," *International Journal of Heat and Fluid Flow,* Vol. 31, 2010, pp. 201-207.

[40] Sathyamurthi, V., and Banerjee, D., "Non-linear Dynamical Analyses of Transient Surface Temperature Fluctuations During Subcooled Pool Boiling on a Horizontal Disk," *International Journal of Heat and Mass Transfer,* Vol. 52, 2009, pp. 5608-5623.

[41] Sathyamurthi, V., Ahn, H.S., Banerjee, D., and Lau, S. C., "Subcooled Pool Boiling Experiments on Horizontal Heaters Coated With Carbon Nanotubes," *Journal of Heat Transfer,* Vol. 131, 2009, pp. 071501.1-071501.10.

[42] Sinha, N., Ahn, H.S., Williams, R., and Banerjee, D., "Packaging of Surface Micromachined Thin Film Thermocouples (TFT): Comparison of the Resistance Arc Microwelding Technique With Wire Bonding," *Components and Packaging Technologies, IEEE Transactions*, Vol. 32, 2009, No. 2, pp. 252-260.

[43] Ahn, H.S., Sathyamurthi, V., and Banerjee, D., "Pool Boiling Experiments on a Nano-Structured Surface," *Components and Packaging Technologies, IEEE Transactions*, Vol. 32, No. 1, 2009, pp. 156-165.

[44] Sunder, M. and Banerjee D., "Experimental Investigation of Micro-scale Temperature Transients in Sub-cooled Flow Boiling on a Horizontal Heater," *International Journal of Heat and Fluid Flow,* Vol. 30, 2009, pp. 140-149.

[45] Sinha, N., "Design, Fabrication, and Testing of Thin Film Thermocouples for Boiling Studies," M.S. Thesis, University of Pennsylvania, August, 2006.

[46] Sathyamurthi, V., "Pool Boiling Studies on Nanotextured Surfaces under Highly Subcooled Conditions," M.S. Thesis, Department of Mechanical Engineering, Texas A&M University, December, 2006.

[47] Sathyamurthi, V., "Dynamics of Pool Boiling: Impact of Surface Texturing and Subcooling," Ph.D. Dissertation, Department of Mechanical Engineering, Texas A&M University, December, 2009.

[48] Ahn, H.S., "Heat Transfer Enhancement in Single-Phase Forced Convection with Blockages and in Two-Phase Boiling with Nano-Structured Surfaces," Ph.D. Dissertation, Department of Mechanical Engineering, Texas A&M University, May, 2007.

[49] Sriraman, S.R., "Pool Boiling on Nano-Finned Surfaces," M.S. Thesis, Department of Mechanical Engineering, Texas A&M University, December, 2007.

[50] Glenn, S., "Effects of Carbon Nanotube Coating on Bubble Departure Diameter and Frequency in Pool Boiling on a Flat, Horizontal Heater," M.S. Thesis, Department of Mechanical Engineering, Texas A&M University, Spring, 2009.

[51] Unnikrishnan, V.U., Reddy, J.N., and Banerjee, D., "Atomistic-Mesoscale Thermal Analysis of Carbon Nanotube Systems", *International Journal of Thermal Sciences,* Vol. 47, Issue 12, December 2008, pp. 1602-1609.

[52] Unnikrishnan V. U., Reddy J. N., Banerjee D., and Rostam-Abadi F., "Thermal Characteristics of Defective Carbon Nanotube-Polymer Nanocomposites,"

Interaction and Multiscale Mechanics, An International Journal, Vol. 1, No. 4, 2008, pp. 397-410.

[53] Shin, D., and Banerjee, D., "Effects of silica nanoparticles on enhancing the specific heat capacity of carbonate salt eutectic (work in progress)", *International Journal of Structural Change in Solids – Mechanics and Applications,* Vol. 2, No. 2, November 2010, pp. 25-31.

[54] Shin, D., and Banerjee, D., "Enhanced Specific Heat of Silica Nanofluid", *ASME Journal of Heat Transfer*, Vol. 133, Issue 2, February 2011.

[55] Shin, D., and Banerjee, D., "Enhancement of specific heat of high-temperature silica nanofluids synthesized in alkali chloride salt eutectics for solar thermal-energy storage applications", *International Journal of Heat and Mass Transfer*, Vol. 54, Issues 5-6, February 2011, pp. 1064-1070.

[56] Singh, N., Unnikrishnan, V., Banerjee, D., and Reddy, J.N., "Analysis of Thermal Interfacial Resistance between Nanofins and Various Coolants", *International Journal of Computational Methods in Engineering Science and Mechanics,* Vol. 12, Issue 5, December 2011, pp. 254-260.

[57] Shin, D. and Banerjee, D., "Enhanced specific heat capacity of nanomaterials synthesized by dispersing silica nanoparticles in eutectic mixtures", *ASME Journal of Heat Transfer*. (accepted, in print), January, 2012.

[58] Yang, H., and Banerjee, D., "Study of Specific Heat Capacity Enhancement of Molten Salt Nanomaterials for Solar Thermal Energy Storage (TES)", Paper No.

MNHMT2012-75338, ASME 2012 3rd Micro/Nanoscale Heat and Mass Transfer International Conference, Atlanta, GA, Mar. 3-6, 2012.

[59] Jo, B. and Banerjee, D., "Enhanced Specific Heat Capacity of Nanocomposites using Organic Nanoparticles", Paper No. IMECE2011-64001, ASME 2011 International Mechanical Engineering Congress and Exposition, Hyatt Regency Denver and Colorado Convention Center, November 11-17, 2011.

[60] Yu, J., Kang, S., Jeon, S., and Banerjee, D., "Investigation of Convective Heat Transfer of Aqueous Nanofluids in Microchannels integrated with Temperature Nanosensors", Paper No. IMECE2011-64082, ASME 2011 International Mechanical Engineering Congress and Exposition, Hyatt Regency Denver and Colorado Convention Center, November 11-17, 2011.

[61] Jo, B., Jung, S., Shin, D., and Banerjee, D., "Anomalous Rheological Behavior of Complex Fluids (Nanofluids)", Paper No. IMECE2011-64091, ASME 2011 International Mechanical Engineering Congress and Exposition, Hyatt Regency Denver and Colorado Convention Center, November 11-17, 2011.

[62] Jung, S., and Banerjee, D., "A simple analytical model for specific heat of nanofluid with tube shaped and disc shaped nanoparticles", Paper No. AJTEC2011-44372, ASME/JSME 8th Thermal Engineering Joint Conference, Honolulu, Hawaii, March 13-17, 2011.

[63] Jo, B., and Banerjee, D., "Interfacial Thermal Resistance between a Carbon Nanoparticle and Molten Salt Eutectic: Effect of material properties, particle shapes

and sizes", Paper No. AJTEC2011-44373, ASME/JSME 8th Thermal Engineering Joint Conference, Honolulu, Hawaii, March 13-17, 2011.

[64] Lang, S., Jeon, S., and Banerjee, D., "Experimental Study of Thermal Performance of Nanofluids During Flow in Microchannels using Surface Temperature-Nano-Sensors", Paper No. AJTEC2011-44374, ASME/JSME 8th Thermal Engineering Joint Conference, Honolulu, Hawaii, March 13-17, 2011.

[65] Shin, D., and Banerjee, D., "Experimental Investigation of molten salt nanofluid for solar thermal energy application", Paper No. AJTEC2011-44375, ASME/JSME 8th Thermal Engineering Joint Conference, Honolulu, Hawaii, March 13-17, 2011.

[66] Shin, D., and Banerjee, D., "Enhancement of Heat Capacity of Molten Salt Eutectics Using Inorganic Nanoparticles for Solar Thermal Energy Applications", Proceedings of the 35th International Conference and Exposition on Advanced Ceramics and Composites (ICACC 2011), Organized by the Engineering Ceramics Division of The American Ceramic Society, January 23 - 28, 2011, Hilton Daytona Beach Resort and Ocean Center, Daytona Beach, Florida.

[67] Jung, S., and Banerjee, D., "Enhancement of Heat Capacity of Nitrate Salts Using Mica Nanoparticles", Proceedings of the 35th International Conference and Exposition on Advanced Ceramics and Composites (ICACC 2011), Organized by the Engineering Ceramics Division of The American Ceramic Society, January 23 - 28, 2011, Hilton Daytona Beach Resort and Ocean Center, Daytona Beach, Florida.

[68] Jo, B., and Banerjee, D., "Enhanced Viscosity of Aqueous Silica Nanofluids", Proceedings of the 35th International Conference and Exposition on Advanced

Ceramics and Composites (ICACC 2011), Organized by the Engineering Ceramics Division of The American Ceramic Society, January 23 - 28, 2011, Hilton Daytona Beach Resort and Ocean Center, Daytona Beach, Florida.

[69] Jung, S., Jo, B., Shin, D., and Banerjee, D., "Experimental Validation of a Simple Analytical Model for Specific Heat Capacity of Aqueous Nanofluids", Paper No. SAE-10PSC-0134, SAE Power Systems Conference, November 2-4, Fort Worth, Texas, 2010.

[70] Jeon, S., Kang, S., and Banerjee, D., "Investigation of Thermal Characteristics of Nanofluids during Flow in a Micro-channel using an Array of Surface Temperature-nanosensors", Paper No. SAE-10PSC-0135, SAE Power Systems Conference, November 2-4, Fort Worth, Texas, 2010.

[71] Shin, D., and Banerjee, D., "Enhanced specific heat capacity of molten salt-metal oxide nanofluid as heat transfer fluid for solar thermal applications", Paper No. SAE-10PSC-0136, SAE Power Systems Conference, November 2-4, Fort Worth, Texas, 2010.

[72] Singh, N., and Banerjee, D., "Thermal Analysis of Carbon Nanotubes suspended in PAO Mixtures", Paper No. SAE-10PSC-0137, SAE Power Systems Conference, November 2-4, Fort Worth, Texas, 2010.

[73] Singh, N., and Banerjee, D., "Investigation of Thermal Interfacial Resistance on Nano-Structures Using Molecular Dynamics", Paper No. IHTC14-22930, 14th International Heat Transfer Conference, August 8-13, Washington, D.C., 2010.

[74] Shin, D., Jo, B., Kwak, H., and Banerjee, D., "Investigation of High Temperature Nanofluids for Solar Thermal Power Conversion and Storage Applications", Paper No. IHTC14-23296, 14th International Heat Transfer Conference, August 8-13, Washington, DC, 2010.

[75] Shin, D., and Banerjee, D., "Enhanced Thermal Properties of PCM Based Nanofluid For Solar Thermal Energy Storage", Paper No. ES2010-90293, ASME 4th International Conference on Energy Sustainability, May 17-22, Phoenix, AZ, 2010.

[76] Kwak, H., Shin, D., and Banerjee, D., "Enhanced Sensible Heat Capacity of Molten Salt Based Nanofluid For Solar Thermal Energy Storage Application", Paper No. ES2010-90295, ASME 4th International Conference on Energy Sustainability, May 17-22, Phoenix, AZ, 2010.

[77] Jo, B., and Banerjee, D., "Study of High Temperature Nanofluids using Carbon Nanotubes (CNT) for Solar Thermal Storage Applications", Paper No. ES2010-90299, ASME 4th International Conference on Energy Sustainability, May 17-22, Phoenix, AZ, 2010.

[78] Shin, D. *, and Banerjee, D., "Investigation of Nanofluids for Solar Thermal Storage Applications", Paper No. ES2009-90465, ASME Energy Sustainability Conference, July 20-25, San Francisco, CA, 2009.

[79] F. P. Incropera, D. P. Dewitt, T. L. Bergman, and A. S. Lavine, *Fundamentals of Heat and Mass Transfer*, 2007, John Wiley and Sons, Inc.

[80] White, G., Tinker, S., and di Marzo, M., "Modeling of Dropwise Evaporative Cooling on a Semi-infinite Solid Subjected to Radiant Heat Input," *Proceedings of*

the 4th International Symposium-Fire Safety Science, Ottawa, Ontario, Canada, 1994, pp. 217-228.

[81] Lloyd, J. R. and Moran, W. R., "Natural Convection Adjacent to Horizontal Surface of Various Planforms," *Journal of Heat Transfer*, 1974, pp. 443-447.

[82] Jeena, V. and Robinson, R. S., "Titanium Dioxide Induced Tandem Oxidation Coupling Reactions," *Beilstein Journal of Organic Chemistry*, Vol. 5, 2009, pp.1-4.

APPENDIX A

CALIBRATION DATA

Each working TFT junction was calibrated by suspending the TFT in an isothermal oven. A calibrated wire bead thermocouple was positioned about half inch from the surface of the TFT junctions and temperature from each thermocouple was recorded for each set point to obtain the calibration curve fit.

The following figures provide a summary of the calibration curves for each TFT junction for each wafer. TFT-C was used for the TiO_2 experiments, TFT-D was used for the uncoated unexposed experiments, and TFT-E was used in experiments conducted at Texas A&M.

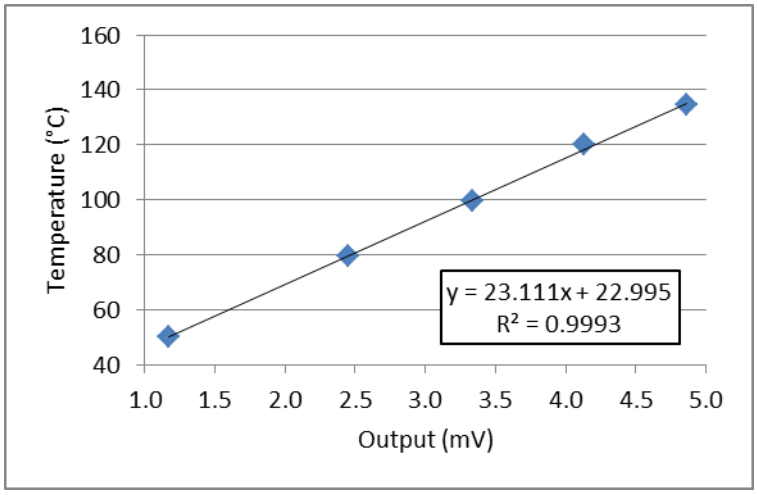

Fig. A.1 Calibration curve for TFT-C, J.1

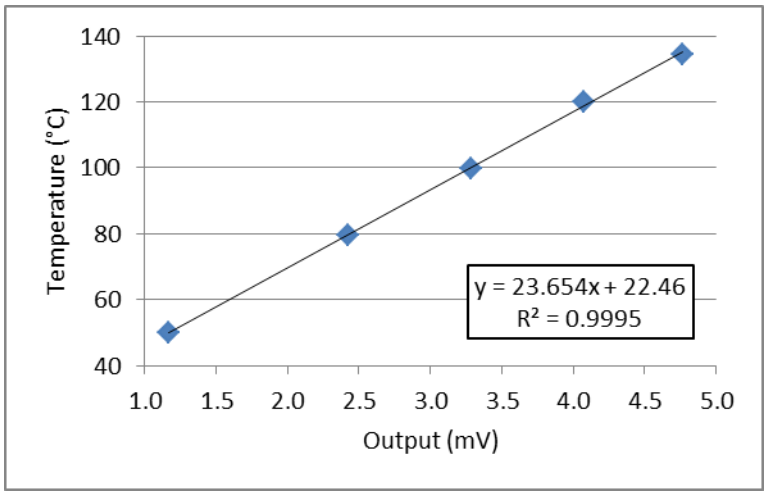

Fig. A.2 Calibration curve for TFT-C, J.3

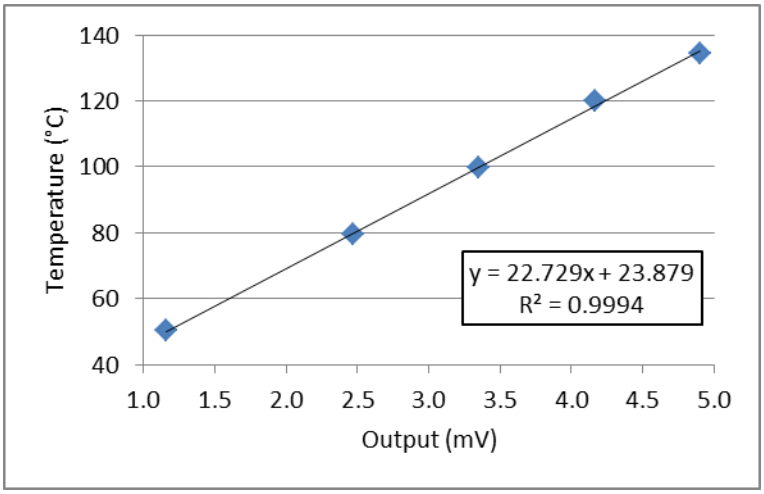

Fig. A.3 Calibration curve for TFT-C, J.6

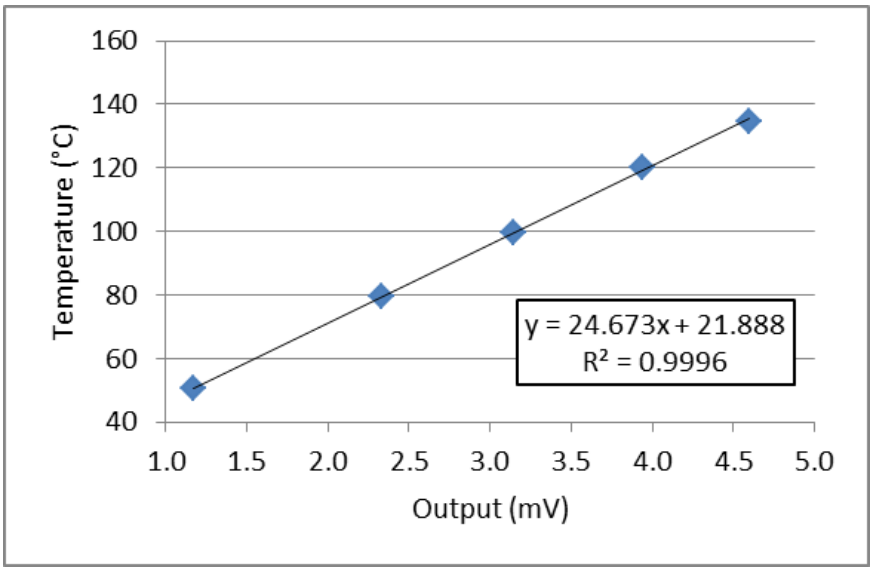

Fig. A.4 Calibration curve for TFT-D, J.1

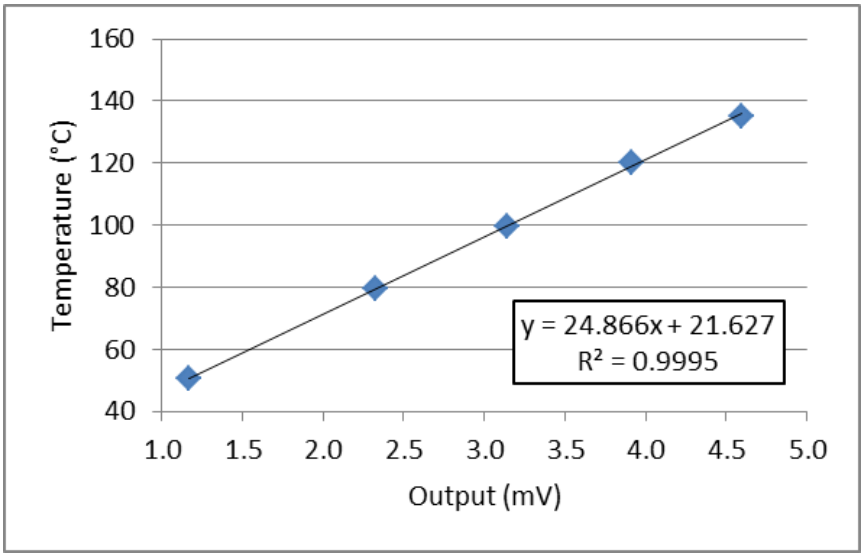

Fig. A.5 Calibration curve for TFT-D, J.4

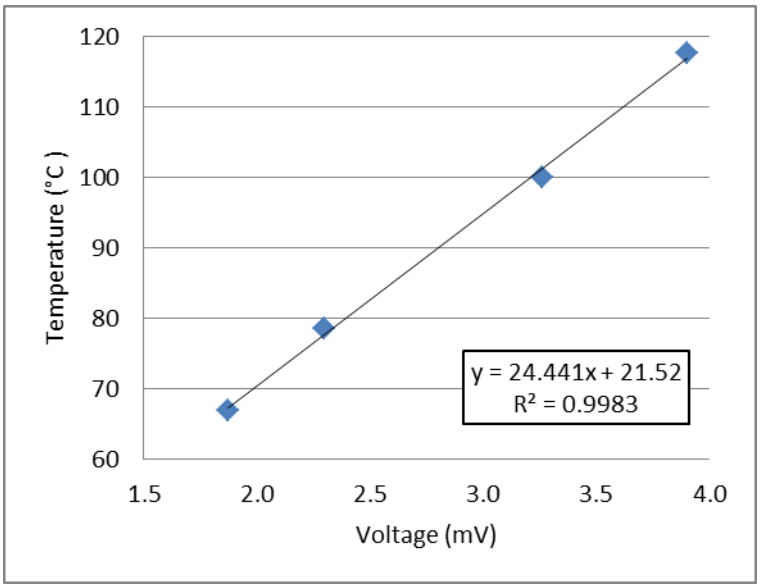

Fig. A.6 Calibration curve for TFT-E, J.1

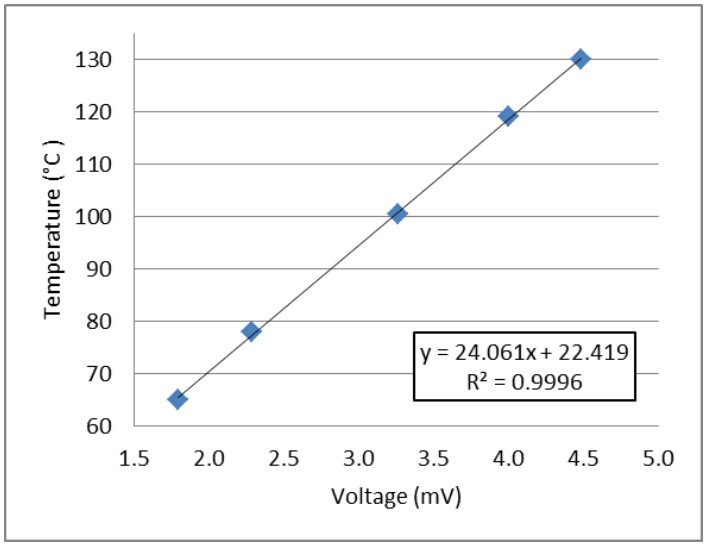

Fig. A.7 Calibration curve for TFT-E, J.3

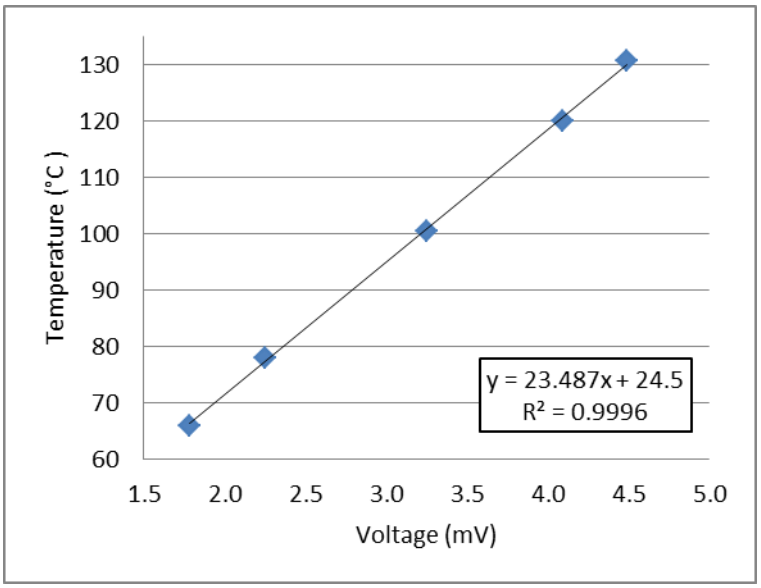

Fig. A.8 Calibration curve for TFT-E, J.4

APPENDIX B

SURFACE ROUGHNESS

Surface roughness was measured after the conclusion of all the experiments. Surface roughness was measured using a Nscriptor® (DPN™) Instrument located at the Materials Characterization Facility (MCF) at Texas A&M University. This instrument is typically used for dip-pen nanolithography (DPN), but can also be used as an Atomic Force Microscope to measure surface roughness. Measurements were performed for wafers with TiO_2 nanocoatings (for experiments at AFRL). Surface roughness prior to performing the experiments is not available. Figures B.1 and B.2 provide a summary of results from the line analysis shown in Figures B.3-10.

Table B.1 Summary of surface roughness measurements: uncoated wafer

Location	Scan (um)	Peak (nm)	RMS (nm)	Average (nm)
J.4	100	920	62	53
J.2	50	1,080	86	68
Center	100	500	57	44

Table B.2 Summary of surface roughness measurements: TiO_2 coated wafer

Location	Scan (um)	Peak (nm)	RMS (nm)	Average (nm)
Center	100	6,000	315	251
Center	50	2,000	155	125
J.1	50	1,200	104	85
J.3	50	3,000	121	101
J.6	50	2,500	126	94

Uncoated Wafer

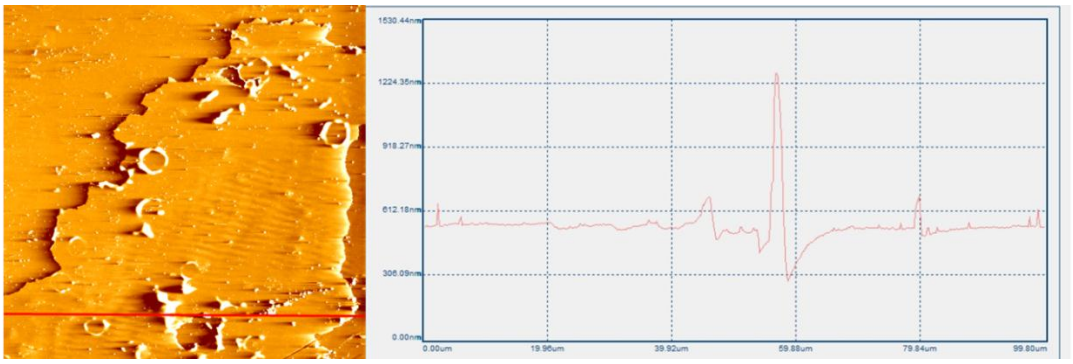

Fig. B.1 Junction 4: Scan (100um), RMS (62nm), Peak (920nm)

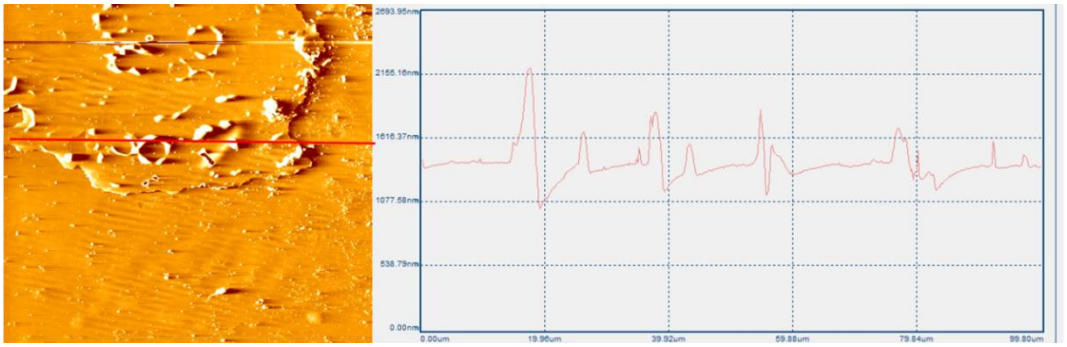

Fig. B.2 Junction 2: Scan (50um), RMS (86nm), Peak (1080nm)

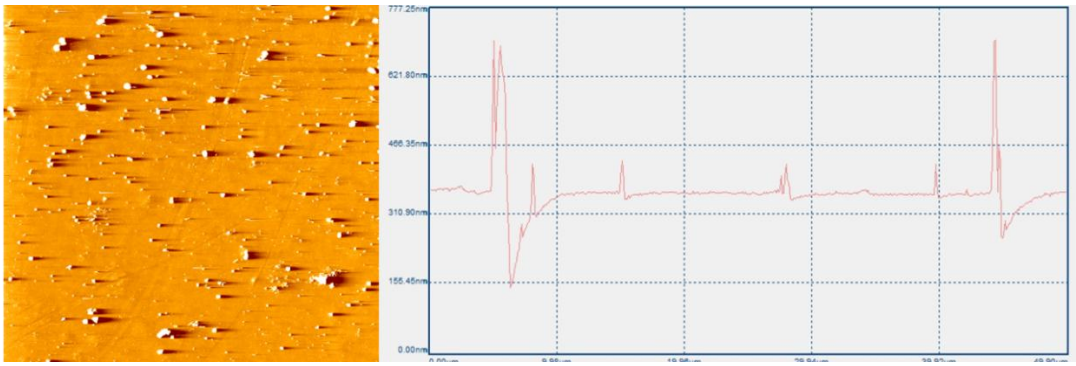

Fig. B.3 Center: Scan (100um), RMS (57nm), Peak (500nm)

TiO_2 Coated Wafer

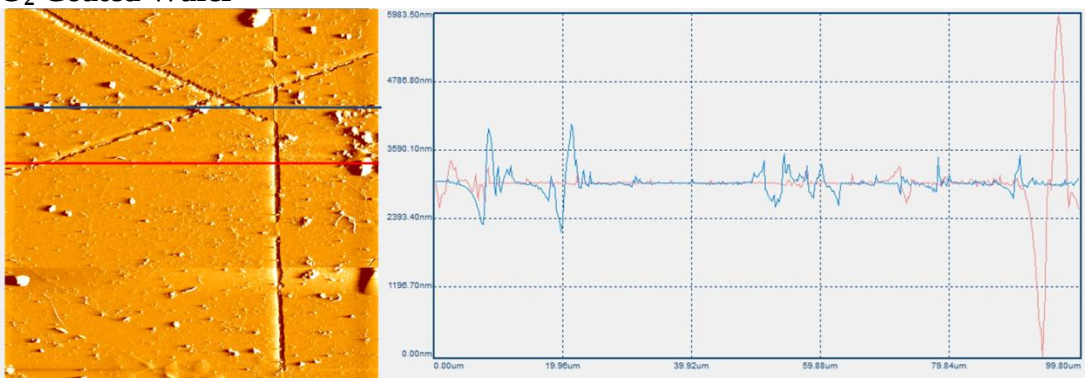

Fig. B.4 Center: Scan (100um), RMS (315nm), Peak (6000nm)

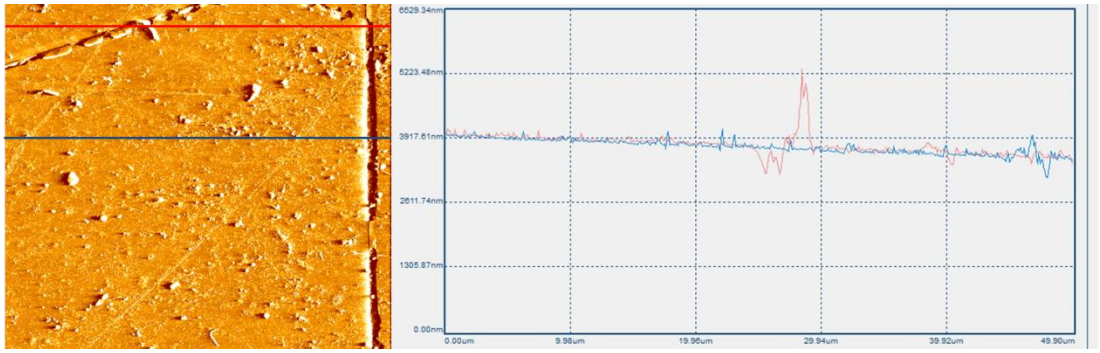

Fig. B.5 Center: Scan (50um), RMS (155nm), Peak (2000nm), Crack ~300nm

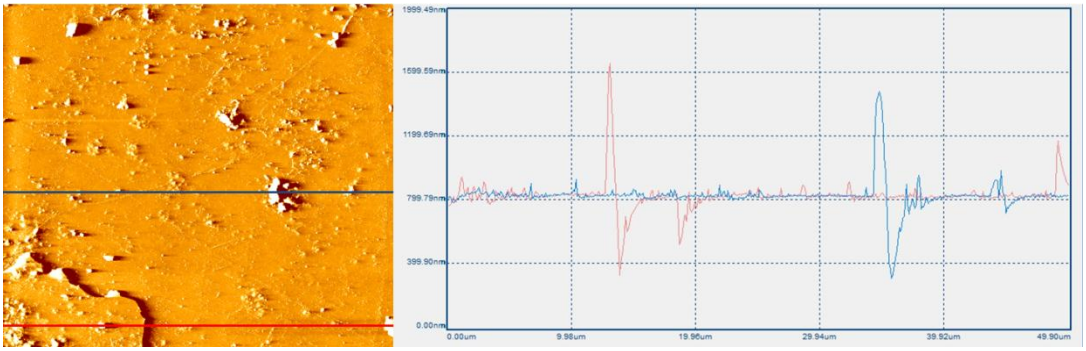

Fig. B.6 Junction 1: Scan (50um), RMS (104nm), Peak (1200nm)

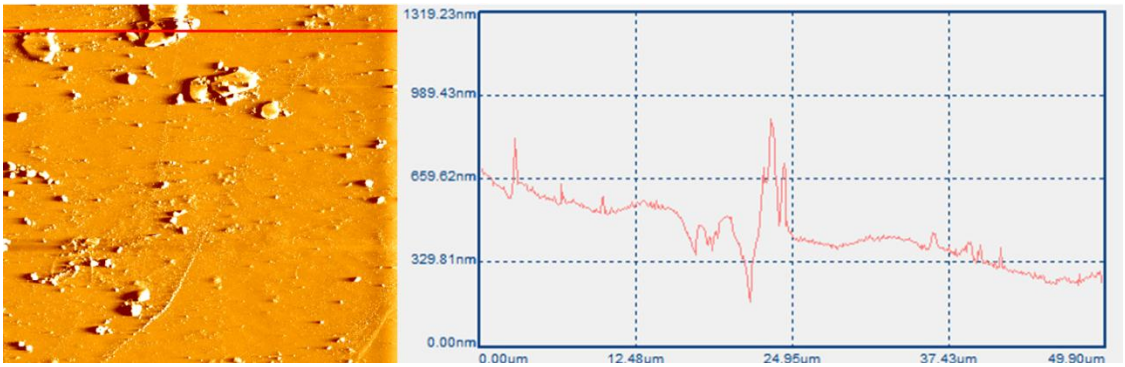

Fig. B.7 Junction 3: Scan (50um), RMS (121nm), Peak (3000nm)

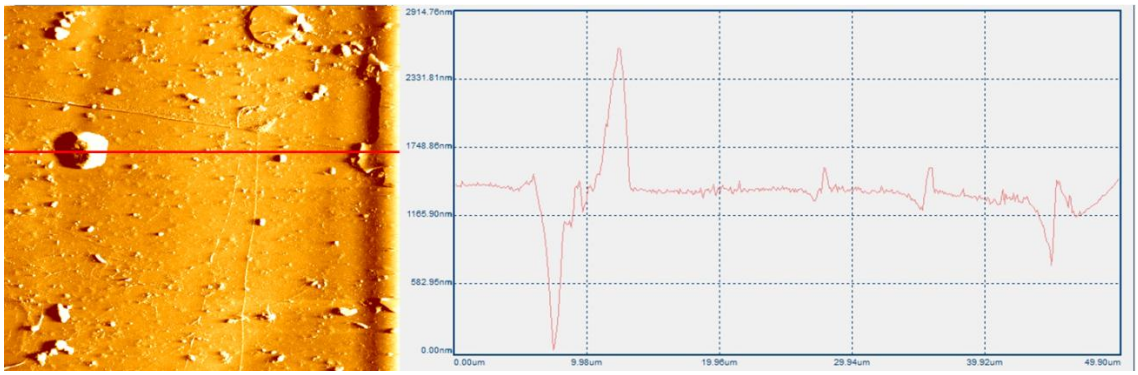

Fig. B.8 Junction 6: Scan (50um), RMS (126nm), Peak (2500nm)

APPENDIX C

UNCERTAINTY ANALYSIS

Measurement uncertainty for estimating the heat flux values was calculated by using the Kline and McClintock method. This method is based on tracing the propagation of uncertainties for each experimental parameter. Thus identifying uncertainty for each experimental parameter is important and is the focus of this appendix. Measurement uncertainty was calculated for both heat transfer coefficients and heat flux values (global and local) for the experiments conducted at AFRL. This appendix has two sections. The first section provides a description of the equations used for estimating the measurement uncertainty for local heat flux values. The second section provides a description of the equations used for estimating the measurement uncertainty for global heat flux values.

Measurement Uncertainty (Local Heat Flux Values)

The equation used to calculate the local heat transfer coefficient is derived from the semi-infinite body assumption with the value of location of *x* set to zero. This equation is:

$$\frac{T(0,t)-T_i}{T_\infty-T_i}=1-\left[\exp\left(\frac{h^2\alpha t}{k^2}\right)\right]\left[\operatorname{erfc}\left(\frac{h\sqrt{\alpha t}}{k}\right)\right] \qquad \text{(C.1)}$$

In order to determine the uncertainty of h, the uncertainty for variables $T(t)$, T_∞, T_i, α, t, and k must be obtained. A summary of the measurement uncertainties for these variables is listed in Table C.1.

Table C.1 Uncertainty values for different parameters

Variable	Value (Units)	Uncertainty Value	Description
α	$8.854 * 10^{-5}\left(\frac{m^2}{s}\right)$	$8.854 * 10^{-7}\left(\frac{m^2}{s}\right)$	1% of value
t (time)	$10 - 11\ ms$	$\left(\frac{d\tau}{dt}\right)$	See discussion below
k	$148\ \left(\frac{W}{m\,K}\right)$	$1.48\ \left(\frac{W}{m\,K}\right)$	1% of value
$T_{initial}$	Varies	$\frac{T_{max} - T_{min}}{T_{min}}$	Values for before droplet impingement, representing error
T_{room}	25°C	0.5°C	Assumed value
T(t)	Varies	$\frac{T_{max} - T_{min}}{T_{min}}$	Values for before droplet impingement, representing error

To calculate uncertainty for time (t) the term

$$\frac{d\tau}{dt} \tag{C.2}$$

is introduced, where t is time and τ is the time constant:

$$\tau = \frac{L_c^2}{\alpha} \tag{C.3}$$

where characteristic length, L_c, is defined as

$$L_c = \frac{V}{A_s} \tag{C.4}$$

where V is volume and A_s is surface area of the TFT junction. This volume and area were calculated as $4.9 * 10^{-16}\ m^3$ and $2 * 10^{-9}\ m^2$, respectively, from the layout diagram in

SolidWorks. Using these values the characteristic length is estimated as $2.45 * 10^{-7} m$. With this value calculated it is important to consider the lumped capacitance method to determine uncertainty for estimating time. To be accurate, this method states that the Biot number must be less than 0.1 to ensure the resistance to conduction within the solid TFT is much less than the resistance to convection across the fluid boundary layer [38]. The Biot number is found as

$$\mathrm{Bi} = \frac{hL_c}{k} \tag{C.5}$$

With max local heat transfer rates from the data found to be around on the order of $10^6 \ \frac{W}{m^2 k}$, the thermal conductivity of nickel (major composition of k-type thermocouples) to be 90.7 $\frac{W}{mk}$, and using previously found characteristic length, the Biot condition of <0.1 is always satisfied and it can be assumed that the temperature gradient inside the TFT junction is sufficiently small and the TFT temperature remains uniform as it is cooled by an impinging water droplet. With this data known, one can use τ, Equation C.3, to find the time it takes for the TFT junction to fully heat or cool for each time step. With this number known and dividing by the time step (10 or 11 ms) using Equation C.2, one can find the uncertainty for time.

The equation used to calculate local heat transfer uncertainty is

$$\frac{w_h}{h} = \left[\left[\frac{w_\alpha}{\alpha}\right]^2 + \left[\frac{w_t}{t}\right]^2 + \left[\frac{w_k}{k}\right]^2 + \left[\frac{w_{Tinitial}}{T_{initial}}\right]^2 + \left[\frac{w_{Troom}}{T_{room}}\right]^2 + \left[\frac{w_{T(t)}}{T(t)}\right]^2 \right]^{1/2} \tag{C.6}$$

and is calculated using the values listed in Table C.1. With uncertainty for the heat transfer coefficient known, uncertainty of the convection equation can be calculated as

$$\frac{w_q}{q} = \left[\left[\frac{w_h}{h}\right]^2 + \left[\frac{w_{T(t)}}{T(t)}\right]^2 + \left[\frac{w_{Troom}}{T_{room}}\right]^2\right]^{1/2} \quad \text{(C.7)}$$

It is observed that measurement uncertainty for local heat flux varies from ~5% to 10%. The values of measurement uncertainty are most sensitive to the measurement of T(t) and $T_{initial}$, since these measurements are accounted for twice in the uncertainty analyses.

Measurement Uncertainty (Global Heat Flux Values)

Measurement uncertainty of global heat flux values was calculated using a similar procedure. However, different equations were used to calculate the two phase heat flux. Hence, measurement uncertainty propagation in each equation must be determined and calculated values should be used in the appropriate equations. The uncertainty for the natural convection heat transfer (and the Nusselt number) is assumed to be 7%; based on the literature reports by Lloyd and Moran [81]. The uncertainty for the natural convection heat transfer coefficient is determined as:

$$\frac{w_{hnc}}{h_{nc}} = \left[\left[\frac{w_k}{k}\right]^2 + \left[\frac{w_{Nu}}{Nu}\right]^2 + \left[\frac{w_L}{L}\right]^2\right]^{1/2} \quad \text{(C.8)}$$

$$\frac{w_{qnc}}{q_{nc}} = \left[\left[\frac{w_{hnc}}{h_{nc}}\right]^2 + \left[\frac{w_{Tinitial}}{T_{initial}}\right]^2 + \left[\frac{w_{Troom}}{T_{room}}\right]^2\right]^{1/2} \quad \text{(C.9)}$$

$$\frac{w_{Rc}}{T_c} = \left[\left[\frac{w_{Theater}}{T_{heater}}\right]^2 + \left[\frac{w_{Tinitial}}{T_{initial}}\right]^2 + \left[\frac{w_{qnc}}{q_{nc}}\right]^2\right]^{1/2} \quad \text{(C.10)}$$

$$\frac{w_{q2phase}}{q_{2phase}} = \left[\left[\frac{w_{Theater}}{T_{heater}}\right]^2 + \left[\frac{w_{T(t)}}{T_t}\right]^2 + \left[\frac{w_{Rc}}{R_c}\right]^2\right]^{1/2} \quad \text{(C.11)}$$

Uncertainty values for each term are listed in Table C.2.

Table C.2 Uncertainty values for different parameters

Variable	Value (Units)	Uncertainty Value	Description
L	0.00625 (m)	$6.25 * 10^{-5}$ (m)	1% of value
Nu	Varies	7%	See source (40)
k	$148\ \left(\frac{W}{m\,K}\right)$	$1.48\ \left(\frac{W}{m\,K}\right)$	1% of value
$T_{initial}$	Varies	$\frac{T_{max} - T_{min}}{T_{min}}$	Values for before droplet impingement, representing error
T_{room}	25°C	0.5°C	Assumed value
T_{heater}	Varies	0.5°C	Assumed value

The measurement uncertainty for the global heat flux is estimated to range from 8~20%. The values of measurement uncertainty are most sensitive to the measurement of T(t) and $T_{initial}$, since these measurements are accounted for several times in the uncertainty analyses.

APPENDIX D

ADDITIONAL DROPLET DATA AND NON-DIMENSIONAL DATA

In this appendix, detailed information about contact angle measurements is presented for both uncoated and coated wafers. These measurements were performed using the images from the droplet impingement studies at the Air Force Research Lab as well for the uncoated wafers used at Texas A&M. In addition, both dimensional parameters and non-dimensional variables are calculated.

Table D.1 Dimensional data for coated unexposed experiments (AFRL)

Drop	Contact Angle (°)		Volume		Impact Velocity	Surface Area	
	Left	Right	Mass (mg)	Volume (mm^3)	Velocity (mm/s)	Radius (mm)	S.A. (mm^2)
105C							
Drop 1	66	68	3.8	3.8	16	1.4	6.4
Drop 2	66	71	4.2	4.3	25	1.4	6.2
115C							
Drop 1	64	73	4.1	4.1	55	1.5	6.9
Drop 2	53	53	4.4	4.4	50	1.7	9.1
Drop 3	51	55	4.3	4.3	46	1.5	6.9
121C							
Drop 1	69	71	4.2	4.2	48	1.4	6.4
Drop 5	67	69	4.1	4.1	38	1.5	7.3
131C							
Drop 1	82	82	3.8	3.9	138	1.4	6.1
Drop 3	69	80	4.0	4.0	131	1.4	6.2
Average	**65**	**69**	**4.1**	**4.1**	**61**	**1.5**	**6.8**
Std. Dev.	**9**	**10**	**0.2**	**0.2**	**44**	**0.1**	**0.9**

Table D.2 Non-dimensional and evaporation data for coated unexposed experiments (AFRL)

Drop	Dimensionless Parameters				Evaporation Rates	
	Weber #	Bond #	Reynolds #	Jacob #	Evaporation Time (s)	Evaporation Rate (mg/s)
105C						
Drop 1	0.0	1.11	55	0.005	17.8	0.2
Drop 2	0.0	1.08	82	0.004	15.5	0.3
115C						
Drop 1	0.1	1.20	189	0.011	*Cannot Be Determined*	
Drop 2	0.1	1.58	200	0.011	11.2	0.4
Drop 3	0.1	1.20	159	0.010	9.2	0.5
121C						
Drop 1	0.1	1.12	161	0.021	6.5	0.7
Drop 5	0.1	1.26	135	0.022	6.3	0.7
131C						
Drop 1	0.7	1.06	449	0.042	3.1	1.3
Drop 3	0.7	1.08	432	0.038	3.8	1.1
Average	**0.2**	**1.19**	**207**	**0.018**		
Std. Dev.	**0.3**	**0.16**	**140**	**0.014**		

Table D.3 Dimensional data for coated exposed experiments (AFRL)

Drop	Contact Angle (°)		Volume		Impact Velocity	Surface Area	
	Left	Right	Mass (mg)	Volume (mm^3)	Velocity	Radius (mm)	S.A. (mm^2)
105C							
Drop 1	58	57	4.3	4.3	53	1.6	8.0
Drop 4	55	58	4.3	4.3	*Cannot Be Determined*	1.6	8.1
Drop 5	63	65	4.1	4.1	30	1.6	8.4
115C							
Drop 1	68	60	4.1	4.1	56	1.5	7.1
Drop 3	62	61	4.5	4.5	56	1.6	7.7
Drop 5	57	57	4.1	4.1	93	1.6	8.2
121C							
Drop 5	53	59	4.3	4.3	38	1.6	7.7
Drop 7	56	60	4.0	4.1	55	1.6	7.7
131C							
Drop 1	63	68	3.9	3.9	47	1.4	6.3
Drop 5	62	72	4.3	4.3	46	1.5	6.7
Average	**60**	**62**	**4.2**	**4.2**	**53**	**1.6**	**7.6**
Std. Dev.	**4**	**5**	**0.2**	**0.2**	**18**	**0.1**	**0.7**

Table D.4 Non-dimensional and evaporation data for coated exposed experiments (AFRL)

Drop	Dimensionless Parameters				Evaporation Rates	
	Weber #	Bond #	Reynolds #	Jacob #	Evaporation Time (s)	Evaporation Rate (mg/s)
105C						
Drop 1	0.1	1.38	199	0.004	13.6	0.3
Drop 4	*Cannot Be Determined*	1.40	*Cannot Be Determined*	0.005	13.2	0.3
Drop 5	0.0	1.46	115	0.004	15.7	0.3
115C						
Drop 1	0.1	1.24	199	0.013	10.5	0.4
Drop 3	0.1	1.34	206	0.012	10.8	0.4
Drop 5	0.4	1.43	352	0.012	9.0	0.5
121C						
Drop 5	0.1	1.35	139	0.021	6.2	0.7
Drop 7	0.1	1.33	201	0.021	5.4	0.7
131C						
Drop 1	0.1	1.09	156	0.040	3.3	1.2
Drop 5	0.1	1.17	157	0.037	3.9	1.1
Average	**0.1**	**1.32**	**192**	**0.017**		
Std. Dev.	**0.1**	**0.12**	**68**	**0.013**		

Table D.5 Dimensional data for uncoated unexposed experiments (AFRL)

Drop	Contact Angle (°)		Volume		Impact Velocity	Surface Area	
	Left	Right	Mass (mg)	Volume (mm^3)	Velocity	Radius (mm)	S.A. (mm^2)
105C							
Drop 1	76	79	3.8	3.8	21	1.5	6.8
Drop 2	79	85	4.4	4.4	41	1.5	6.8
115C							
Drop 1	78	83	3.9	3.9	25	1.5	6.6
Drop 3	78	79	3.8	3.8	23	1.7	9.4
Drop 4	78	80	3.7	3.7	30	1.6	8.3
Drop 5	75	75	4.4	4.4	25	1.5	7.3
121C							
Drop 1	83	79	4.0	4.1	30	1.4	6.6
Average	**78**	**80**	**4.0**	**4.0**	**28**	**1.5**	**7.4**
Std. Dev.	**3**	**3**	**0.3**	**0.3**	**7**	**0.1**	**1.1**

Table D.6 Non-dimensional and evaporation data for uncoated unexposed experiments (AFRL)

Drop	Dimensionless Parameters				Evaporation Rates	
	Weber #	Bond #	Reynolds #	Jacob #	Evaporation Time (s)	Evaporation Rate (mg/s)
105C						
Drop 1	0.0	1.18	71	0.005	17.2	0.2
Drop 2	0.1	1.19	142	0.001	19.6	0.2
115C						
Drop 1	0.0	1.16	86	0.020	9.5	0.4
Drop 3	0.0	1.64	93	0.020	8.9	0.4
Drop 4	0.0	1.44	113	0.021	8.6	0.4
Drop 5	0.0	1.27	90	0.022	9.0	0.5
121C						
Drop 1	0.0	1.14	101	0.034	5.9	0.7
Average	**0.0**	**1.29**	**99**	**0.018**		
Std. Dev.	**0.0**	**0.19**	**23**	**0.011**		

Table D.7 Dimensional and non-dimensional data 0% exposure experiments (Texas A&M)

0% Exposure

Drop	Evap Time (s)	Contact Angle (°) Left	Right	Radius (mm)	Volume (mm^3)	Mass (mg)	Bond #	Jacob #
105C								
Drop 1	30	63	70	0.9	2.4	2.4	0.48	0.005
Drop 2	30	67	66	1.0	2.4	2.4	0.46	0.005
Drop 3	29	67	71	0.9	2.4	2.4	0.48	0.005
110C								
Drop 1	19	66	77	1.0	3.0	3.0	0.52	0.003
Drop 2	19	65	78	1.0	2.9	2.9	0.52	0.003
Drop 3	19	69	79	1.0	2.6	2.6	0.52	0.003
115C								
Drop 1	15	68	X	0.9	2.6	2.6	0.49	0.014
Drop 2	15	69		1.0	2.5	2.5	0.46	0.014
Drop 3	18	63		1.0	2.7	2.7	0.49	0.014
120C								
Drop 1	11	70	X	1.4	4.7	4.7	0.77	0.022
Drop 2	11	69		1.0	6.0	6.0	0.98	0.022
Drop 3	12	67		1.0	3.3	3.2	0.60	0.022
Average		**67**	**73**	**1.0**	**3.1**	**3.1**	**0.56**	**0.011**
Std. Dev.		**2**	**5**	**0.0**	**1.1**	**1.1**	**0.16**	**0.008**

Table D.8 Dimensional and non-dimensional data 50% exposure experiments (Texas A&M)

50% Exposure

Drop	Evap Time	Contact Angle (°) Left	Right	Radius (mm)	Volume (mm^3)	Mass (mg)	Bond #	Jacob #
105C								
Drop 1	28	65	71	0.9	2.4	2.4	0.48	0.004
Drop 2	29	65	68	0.9	2.6	2.6	0.49	0.004
Drop 3	28	65	67	0.9	2.5	2.5	0.48	0.004
110C								
Drop 1	19	68	79	1.0	3.3	3.3	0.58	0.005
Drop 2	19	67	79	1.0	2.8	2.8	0.53	0.005
Drop 3	23	65	77	1.0	2.7	2.7	0.53	0.005
115C								
Drop 1	19	66	X	1.0	2.6	2.6	0.47	0.009
Drop 2	18	67		1.0	3.4	3.4	0.53	0.009
Drop 3	18	69		1.0	3.4	3.4	0.55	0.009
120C								
Drop 1	9	68	X	1.0	5.6	5.6	1.02	0.022
Drop 2	10	68		1.0	2.8	2.8	0.53	0.022
Drop 3	9	72		1.0	2.7	2.7	0.49	0.022
Average		**67**	**74**	**73.6**	**3.1**	**3.1**	**3.07**	**3.065**
Std. Dev.		**2**	**6**	**5.5**	**0.9**	**0.9**	**0.87**	**0.866**

Table D.9 Dimensional and non-dimensional data 100% exposure experiments (Texas A&M)

100% Exposure

Drop	Evap Time	Contact Angle (°)		Radius (mm)	Volume (mm^3)	Mass (mg)	Bond #	Jacob #
		Left	Right					
105C								
Drop 1	28	66	65	0.9	2.4	2.4	0.48	0.004
Drop 2	29	67	74	0.9	2.4	2.4	0.48	0.004
Drop 3	29	67	70	0.9	2.4	2.3	0.47	0.004
110C								
Drop 1	23	62	78	1.0	3.0	3.0	0.57	0.006
Drop 2	22	65	77	1.0	3.0	3.0	0.56	0.006
Drop 3	22	64	78	1.0	2.6	2.6	0.52	0.006
115C								
Drop 1	17	63	X	1.0	3.4	3.3	0.53	0.012
Drop 2	17	68		1.0	3.2	3.2	0.51	0.012
Drop 3	19	63		1.0	2.9	2.9	0.52	0.012
120C								
Drop 1	9	68	X	1.0	3.1	3.1	0.60	0.024
Drop 2	9	68		1.0	3.0	3.0	0.59	0.024
Drop 3	9	68		1.0	2.9	2.9	0.54	0.024
Average		**66**	**73**		**2.9**	**2.8**	**3.07**	**3.065**
Std. Dev.		**2**	**5**		**0.3**	**0.3**	**0.87**	**0.866**

VITA

Scott William Hansen received his Bachelor of Arts degree in finance from the University of South Dakota in December 2007. While attending school at USD, he was accepted into NASA Johnson Space Center's (JSC) Cooperative Education Program. During his time at JSC he became interested in engineering and decided to pursue an engineering degree. Upon graduating from USD, he enrolled at Texas A&M University and began completing undergraduate courses in mathematics and engineering while continuing to co-op at JSC. Upon completing over seventy hours of undergrad engineering, physics, and math coursework, he was accepted into the Graduate Mechanical Engineering Program at Texas A&M University. He entered graduate studies in January 2011 and interned at the Air Force Research Lab in Dayton, Ohio in Summer 2011 where research on droplet impingement was completed. He received his Master of Science degree in mechanical engineering in May 2012 and began working full-time at Johnson Space Center's Advanced Thermal Group in June 2012.

Mr. Hansen may be reached through the following information.

Address: Texas A&M University
Department of Mechanical Engineering
3123 TAMU
College Station, TX 77843

Email Address: swhansen@neo.tamu.edu